2014

Nonlinear integrated photonics on silicon and gallium arsenide substrates

Jichi Ma
University of Central Florida

NONLINEAR INTEGRATED PHOTONICS ON SILICON AND GALLIUM ARSENIDE SUBSTRATES

by

JICHI MA
B.S. Tsinghua University 2006
M.Sc. Tsinghua University 2008

A dissertation submitted in partial fulfillment of the requirements
for the degree of Doctor of Philosophy
in the College of Optics and Photonics
at the University of Central Florida
Orlando, Florida

Summer Term
2014

Major Professor: Sasan Fathpour

ABSTRACT

Silicon photonics is nowadays a mature technology and is on the verge of becoming a blossoming industry. Silicon photonics has also been pursued as a platform for integrated nonlinear optics based on Raman and Kerr effects. In recent years, more futuristic directions have been pursued by various groups. For instance, the realm of silicon photonics has been expanded beyond the well-established near-infrared wavelengths and into the mid-infrared (3 – 5 µm). In this wavelength range, the omnipresent hurdle of nonlinear silicon photonics in the telecommunication band, i.e., nonlinear losses due to two-photon absorption, is inherently nonexistent. With the lack of efficient light-emission capability and second-order optical nonlinearity in silicon, heterogeneous integration with other material systems has been another direction pursued. Finally, several approaches have been proposed and demonstrated to address the energy efficiency of silicon photonic devices in the near-infrared wavelength range.

In this dissertation, theoretical and experimental works are conducted to extend applications of integrated photonics into mid-infrared wavelengths based on silicon, demonstrate heterogeneous integration of tantalum pentoxide and lithium niobate photonics on silicon substrates, and study two-photon photovoltaic effect in gallium arsenide and plasmonic-enhanced structures.

Specifically, performance and noise properties of nonlinear silicon photonic devices, such as Raman lasers and optical parametric amplifiers, based on novel and reliable waveguide

technologies are studied. Both near-infrared and mid-infrared nonlinear silicon devices have been studied for comparison. Novel tantalum-pentoxide- and lithium-niobate-on-silicon platforms are developed for compact microring resonators and Mach-Zehnder modulators. Third- and second-harmonic generations are theoretical studied based on these two platforms, respectively.

Also, the two-photon photovoltaic effect is studied in gallium arsenide waveguides for the first time. The effect, which was first demonstrated in silicon, is the nonlinear equivalent of the photovoltaic effect of solar cells and offers a viable solution for achieving energy-efficient photonic devices. The measured power efficiency achieved in gallium arsenide is higher than that in silicon and even higher efficiency is theoretically predicted with optimized designs. Finally, plasmonic-enhanced photovoltaic power converters, based on the two-photon photovoltaic effect in silicon using subwavelength apertures in metallic films, are proposed and theoretically studied.

To my parents, Sui Ma and Huaihong Zhu;

and my wife, Si Chang

ACKNOWLEDGMENT

I would acknowledge my Ph.D. advisor, Dr. Sasan Fathpour, for his trust in me, which manifested in his offer for a graduate research assistant position along with financial support throughout my studies. He is always willing to discuss with me on my research in the field of integrated photonics. I have learned not only knowledge, but more importantly, the way to analyze and solve problems from him. Furthermore, he happens to be more than a Ph.D. advisor. His guidance and mentorship, which was not limited to studies and research, helped me to raise my awareness and creativity level.

Next, I would like to thank my committee members, Dr. David Hagan, Dr. Guifang Li and Dr. Robert Peale, for their valuable time, interest and suggestions on my research.

Many thanks go to my colleagues in the research group, Dr. Payam Rabiei, Dr. Saeed Khan, Jeff Chiles, and Ashutosh Rao for their friendship, help and discussions.

At last and most importantly, my special thanks go to my wife, Si Chang, who brings joy to my life.

TABLE OF CONTENTS

LIST OF FIGURES

LIST OF TABLES

LIST OF ACRONYMS/ABBREVIATIONS

3PA	Three-photon absorption
CMOS	Complementary Metal-Oxide-Semiconductor
CW	Continuous wave
DBR	Distributed Bragg reflector
EO	Electro-optic
FCA	Free-carrier absorption
FOM	Figure of merit
FP	Fabry-Perot
FWM	Four-wave mixing
GSG	Ground-signal-ground
ICP	Inductively-coupled-plasma
IRCM	Infrared countermeasures
LED	Light-emitting diode
LHS	Left-hand side
LIDAR	Light detection and ranging
LOCOS	Local oxidation of silicon
MMI	Multimode interferometers
MWIR	Mid-wave infrared
MZ	Mach-Zehnder

NF	Noise figure
NIR	Near-infrared
OPA	Optical parametric amplifier
OPO	Optical parametric oscillator
OSA	Optical spectrum analyzer
PECVD	Plasma-enhanced chemical vapor deposition
PPC	Photovoltaic power converter
QCL	Quantum cascade laser
RF	Radio frequency
RHS	Right-hand side
RIE	Reactive ion etching
RIN	Relative intensity noise
SEM	Scanning-electron microscopy
SHG	Second-harmonic generation
SNR	Signal-to-noise ratio
SOI	Silicon-on-insulator
SON	Silicon-on-nitride
SOS	Silicon-on-sapphire
SPM	Self-phase modulation
SRL	Silicon Raman laser
SRS	Stimulated Raman scattering
TEC	Thermoelectric cooler

THG	Third-harmonic generation
TPA	Two-photon absorption
TPPV	Two-photon photovoltaic
VCSOA	Vertical-cavity semiconductor optical amplifier
VCSEL	Vertical-cavity surface-emitting laser
VCSRA	Vertical cavity silicon Raman amplifier

CHAPTER 1: INTRODUCTION

Silicon is an ideal candidate for building photonic devices due to its low linear loss in the 1.2 to 6.5 µm wavelength range. Silicon photonics, also known as group IV photonics, is the study and application of photonic systems which use silicon as the main optical medium [1]. It has attracted significant attention in recent years with the aim of realizing low-cost, high-speed optoelectronic components for data and telecommunication applications, such as high-speed optical interconnects [2], optical routers and signal processors [3], and long-range telecommunications [4]. It has been shown that silicon waveguides are capable of constructing most of the components of a photonic data transmission system on a single chip. Additionally, complex electronic-photonic integrated circuits can be created by integrating these components together with complementary metal-oxide-semiconductor (CMOS) electronics [5].

The field of silicon photonics has been the topic of active research for several years in the near-infrared (near-IR or NIR) wavelength range, i.e., from 1.1 to around 2 µm. The advantages of integrated silicon photonic devices for near infrared data communications applications are well-known, and a large amount of optical components are commercially available at the important 1300 and 1550 nm ranges. A review can be found elsewhere [1]. However, although these wavelengths are convenient for telecommunications, obviously they are not suitable for all applications. Mid-wave infrared (MWIR, also known as mid-IR), defined vaguely as the wavelength range spanning 3 to 5 or sometimes 2 to 6 µm, represents another array of applications, where silicon photonics play an important role. Historically, the need for sources operating in this range has been primarily driven by military applications such as wind Light

Detection and Ranging (LIDAR), remote chemical and biological sensing and infrared countermeasures (IRCM). Over the past decade, such sources have also found use in thermal imaging [6], chemical bond spectroscopy which spans from the visible to 20 µm [7], gas sensing [8] including CO_2 (4.6 µm), NO_x (6.5 µm), CO (4.2 µm) and SO_x (7.3 µm), environmental monitoring and astronomy.

Silicon photonics, however, has an inherent problem at near-infrared wavelengths: significant optical loss under high-power pumping. Although silicon is transparent and has low propagation losses, at high intensities it begins to absorb light due to two-photon absorption (TPA). TPA creates free carriers that, in turn, can absorb more significantly through free-carrier absorption (FCA) [9]. As an indirect band-gap semiconductor, silicon has a low intrinsic recombination rate of free carriers. Consequently, the free-carrier population quickly grows up, resulting in huge optical loss. However, this problem is no longer serious when the wavelength of the incident light exceeds ~2.2 µm (the threshold for TPA to occur). It has been experimentally shown that TPA and the absorption of free carriers can be decreased to negligible levels by going to longer photon wavelengths [10]. As a result, silicon is an excellent nonlinear optical crystal in the MWIR range. It is attracting great interest because it offers the possibility of integrating a variety of passive and active components on a single chip, as well as exploiting an inherent transparency and strong nonlinear optical effects in the MWIR region. Silicon has several additional attractive properties, such as a large thermal conductivity and high-optical-damage threshold.

In the past, the mid-infrared (mid-IR) wavelength range was a problematic region for photonics due to lack of coherent sources and integrated optical waveguides. Recently, although

there are still some missing pieces such as high-bandwidth modulators, tunable filters and optical elements of complex fiber/waveguide-coupled photonic systems, the landscape has begun to change a lot. Inexpensive single-mode quantum cascade lasers (QCLs), exploiting electronic wavefunction engineering at an unprecedented level of sophistication, are now available commercially all the way down to below 4 µm [11]. Single-mode fibers are now available at wavelengths up to 6 µm [12], so are mid-IR photodetectors that operates at near room-temperature with a bandwidth of above 1 GHz (Boston Electronics Corporation). These components make it possible to build efficient mid-infrared devices and give hope to on-chip applications. A new kind of integrated photonics is being born. Future research will focus on integrated room-temperature active and passive devices such as waveguides, amplifiers, resonators, switches, modulators and optical parametric devices. All of these will help to realize on-chip optoelectronic systems. A major part of this dissertation is devoted to several aspects of mid-IR silicon photonic waveguide technology and nonlinear optical effects in them.

The performance of nonlinear devices operating based on third-order nonlinearity ($\chi^{(3)}$) cannot in principle compete with devices based on second-order nonlinearity ($\chi^{(2)}$) for most applications. Silicon is a centrosymmetric crystal and hence $\chi^{(2)}$ does not exist in the material. A hybrid platform, which enjoys the advantages of silicon photonics (CMOS compatibility and low-loss and tightly confined waveguides), and uses a second-order nonlinear material in the waveguide core region instead of silicon is desired. Lithium niobate ($LiNbO_3$) in one of the best candidates due to its high $\chi^{(2)}$ value. Indeed, standard $LiNbO_3$ waveguides are regarded as the best choice for electro-optical modulators in the photonic industry with impressively high modulation bandwidths up to 100 GHz [13]. $LiNbO_3$ modulators definitely offer higher

performance in terms of modulation bandwidth, modulation depth and insertion loss over silicon optical modulators [1]. The challenge for this hybrid approach lies in the fabrication of reliable LiNbO$_3$-on-silicon wafers and low-loss submicron ridge or channel waveguides on the wafers. These problems are addressed here and the demonstrated platform can also an ideal candidate for integrated $\chi^{(2)}$ nonlinear optics, such as second-harmonic generation.

Two-photon photovoltaic (TPPV) effect is an energy harvesting technique based on TPA. It is a nonlinear equivalent of the conventional single-photon photovoltaic effect in solar cells. It was first demonstrated in silicon as a carrier sweep-out technique that not only eliminates the nonlinear losses without electrical power dissipation but also generates electrical power at the same time [14]. The TPPV effect has potential applications in photovoltaic power converters (PPCs) and self-powered remote sensors in fiber-optic network [15]. The TPPV effect is not restricted to silicon. It is also applicable to III-V semiconductors. It is expected to be even stronger in gallium arsenide (GaAs), as studied here for the first time, and indium phosphide (InP) [16]. The power efficiency of the PPCs based on the TPPV effect can also be enhanced by the plasmonic effect of subwavelength apertures, as studied in this work.
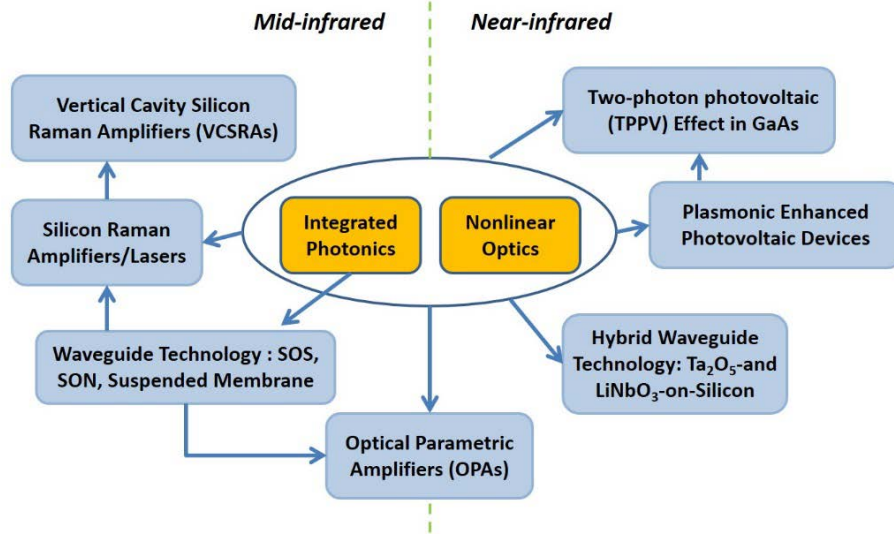
Figure 1-1: Organization of the dissertation.

The organization of this dissertation is depicted in Fig. 1-1. Theoretical models are developed and experimental works are conducted to study and test the performance of nonlinear integrated photonic devices on silicon and GaAs substrates. In Chapter 2, mid-IR nonlinear silicon photonic devices based on Raman (silicon Raman amplifiers/lasers) and Kerr effects (optical parametric amplifiers (OPAs) and continuum generation sources) are theoretically studied. Chapter 3 numerically investigated the noise figure (NF) spectra of near-IR amorphous silicon (a-Si) and mid-IR crystalline silicon (c-Si) OPAs. In Chapter 4, two novel waveguide technologies, Ta_2O_5-on-Si and $LiNbO_3$-on-Si, based on newly demonstrated fabrication techniques, are introduced and their potential applications in nonlinear integrated photonics such as harmonic generation are proposed and theoretically investigated. Chapter 5 focuses on the TPPV effect in GaAs, which is expected to be more efficient than in silicon and thus can be utilized in self-powered optoelectronic chips and PPCs. Chapter 6 presents the theoretical study of plasmonic-enhanced silicon photovoltaic devices including solar cells with nanoparticles and

5

two-photon PPCs using nanoaperture structures. The final chapter shows the ideas on future research direction for nonlinear integrated photonic devices on silicon and III-V semiconductor substrates.

CHAPTER 2: MID-INFRARED NONLINEAR SILICON PHOTONICS

2.1   Overview

The second-order optical susceptibility is absent in silicon because the material is in the form of a centrosymmetric crystal. Alternatively, third-order nonlinearity in silicon has been exploited and aggressively studied in the last decade. More recently, silicon photonics has been pursued in the mid-IR regime with a host of civilian and military applications. Optical Raman amplification at 3.4 µm [17,18], four-wave mixing (FWM) and parametric amplification at ~2.2 µm [19 , 20], silicon-on-sapphire (SOS) waveguides at 4.5 µm [21], silicon-on-insulator waveguides at 3.39 µm [22] and SOS gratings couplers at 2.75 µm [23] are some of the recent developments in the emerging field of mid-IR silicon photonics.

The nonlinear absorption processes in near-IR silicon photonic devices include TPA (in which two photons can simultaneously get absorbed and excite an electron out of the valance band and into the conduction band), free-carrier absorption (FCA) induced by TPA, as well as higher order nonlinear process such as three-photon absorption, which can occur at very high intensities. These processes have been found to create additional loss mechanisms for optical waves interacting with each other in silicon. Therefore, the efficiency of the nonlinear processes is significantly reduced.

TPA and the generation of free carriers in silicon for near-IR pumps are shown in Fig. 2-1. The population of free carriers builds up rapidly because of their long lifetime in silicon as an indirect band-gap material, causing photons to be lost through FCA. The rate of two-photon

generation is much larger for higher energy pump photons due to the number of available electron states in both the valence band and the conduction band. V. Raghunathan *et al*. studied the transmission through a silicon sample at two pump wavelengths, 2.09 µm and 2.936 µm [10]. The maximum transmission was around 53% because the silicon sample is double-sided polished and the reflection loss per facet is around 29%. The enhanced nonlinear losses at 2.09 µm due to TPA and FCA and the absence of these losses at 2.936 µm are clearly illustrated in Ref. [10].
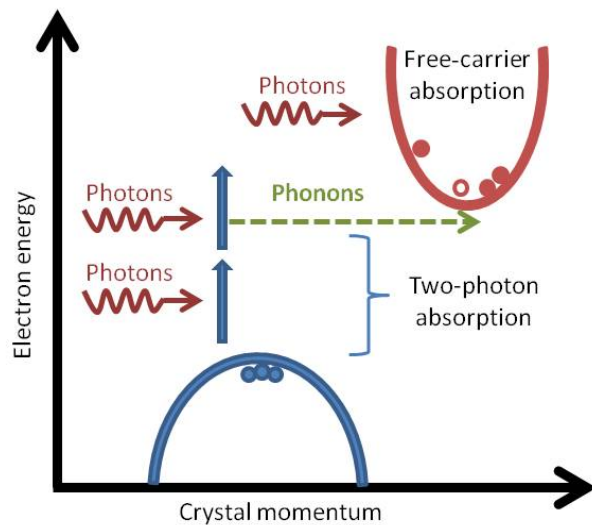
Figure 2-1: TPA and the associated FCA for near-IR pumps [24].

Absorption by TPA-induced free carriers is a broadband process that competes with the Raman or FWM gain. TPA has been shown to be negligible from the point of view of pump depletion. This is reasonable because the TPA coefficient in silicon, β, is relatively small (about 0.5 cm/GW) compared with the Raman gain coefficient at 1550-nm wavelength. The magnitude of the TPA-induced FCA depends on free carrier concentration and the effective recombination lifetime for free carriers. In order to make the nonlinear processes more efficient, a lot of effort

has been put on minimizing the carrier concentration in the near-IR regime. Active carrier sweep-out using *p-i-n* junction diodes and short pulse pumping have been proposed as means to mitigate this problem [1].

Three-photon absorption (3PA) might be more problematic at the mid-IR than the near-IR because of the square-wavelength (λ^2) dependence of the free-carrier scattering cross-section. However, the three-photon absorption coefficient, γ, is quite small. Measured in the range from 2300 nm to 3300 nm with a 200 fs pulsed laser, γ has a peak value of 0.035 cm^3/GW^2 [25]. If the pump wavelength is above 3300 nm, or the pump intensity is just a few hundred MW/cm^2, which is enough for stimulated Raman scattering and FWM to take place, three-photon absorption is virtually negligible.

2.2   Waveguide Technologies for Mid-IR Silicon Photonics

A reliable low-loss optical waveguide technology is of great importance for any integrated photonics platform. The silicon-on-insulator (SOI) platform is generally not suitable for the mid-IR because the bottom cladding material, silicon dioxide (SiO$_2$), is lossy over the 2.5-2.9 µm and above 3.6 µm wavelengths. My colleagues and I have been developing novel waveguide platforms and unique fabrication techniques to expand the realm of silicon photonics into the Mid-IR wavelengths. Figure 2-2 illustrates the three platforms we have demonstrated so far: silicon-on-sapphire (SOS), silicon-on-nitride (SON) [26] and all-silicon optical platform (ASOP) [27].

Sapphire has high transmittance over the broad 1 to 5 µm range [28]. Therefore, silicon-on-sapphire (SOS) wafers can be used for both mid- and near-IR photonics. SOS waveguides were first proposed by Soref *et al*. [28] and then demonstrated by Hochberg *et al*. [21]. However, fabricating submicron waveguides using electron-beam (e-beam) lithography results in poor sidewall roughness and high propagation loss. We have been developing a unique SOS waveguide fabrication technology-local oxidation of silicon (LOCOS) of microelectronic fabrication [29]. This method not only smoothens the sidewall roughness, but also shrinks the lateral dimension of the waveguide (see the scanning-electron microscopy image for SOS waveguides in Fig. 2-2(b)). Therefore, the technique can beat the resolution limit of conventional micron-size mask aligners and achieve submicron waveguides.
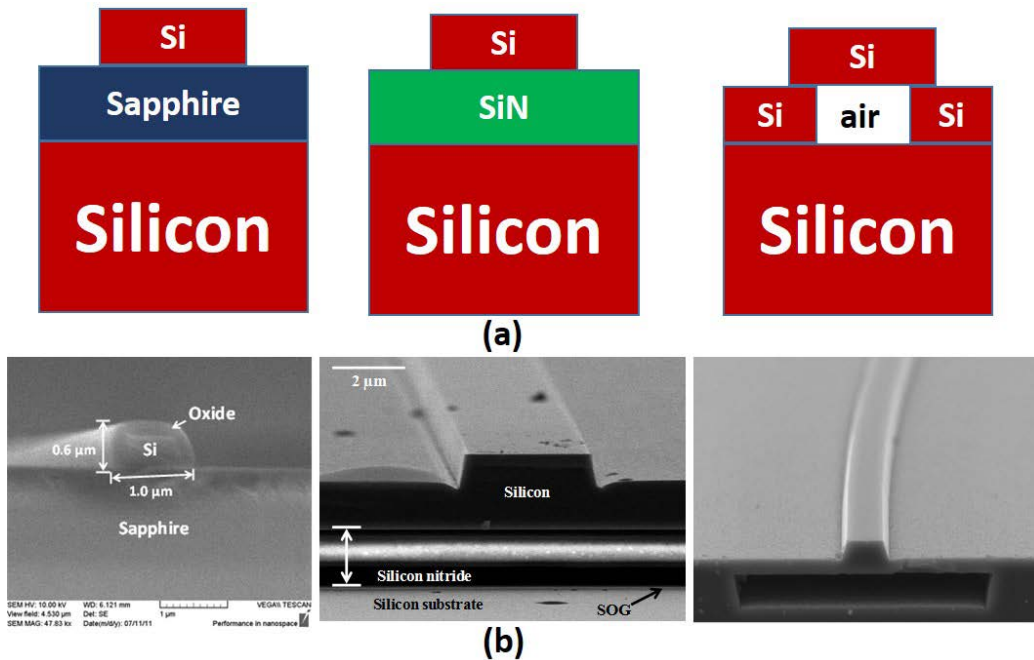
Figure 2-2: (a) Three waveguide technologies of silicon photonics at mid-IR based on novel fabrication techniques: SOS, SON, and all-silicon waveguiding platform. (b) SEM images of the fabricated waveguides for the three platforms [26,27].

The linear propagation loss α of the SOS waveguides at wavelength of 1550 nm was first characterized using the Fabry-Perot (FP) method (Fig. 2-3(a)). Interference fringes can be observed in the transmission spectrum of the waveguide as FP cavity is formed by the two facets of the waveguide. α was then extracted from the modulation depth of the FP fringes:

$$\alpha = \frac{1}{L}\log\left(R\frac{1+\sqrt{P_{min}/P_{max}}}{1-\sqrt{P_{min}/P_{max}}} \right) \tag{2.1}$$

where P_{min} and P_{max} are the minimum and maximum power in the FP fringes, L is the length of the waveguide, and $R=(1-n_{eff})^2/(1+n_{eff})^2$ is the reflectivity of the waveguide facet, where n_{eff} is the effective index of the waveguide calculated in COMSOL^{TM}.

Another convenient and accurate way to measure the linear propagation loss of the waveguide is the cut-back method. The power transmission of L-shape waveguides with different lengths was measured with a photodetector and α was extracted from the least-square linear fit of the data obtained (Fig. 2-3(b)). The radius of curvature of the L-shaped waveguides is 1 mm, which is large enough to ignore any bending loss. The measured loss in the SOS waveguides is 12.1 dB/cm using the FP method and 13.4 dB/cm using the cut-back method at wavelength of 1550 nm. The high propagation loss can be explained by the aluminum generation from chemical interaction between silicon and sapphire at high temperatures, as well as dislocation caused by the large difference in the thermal expansion coefficients and lattice constants of the two materials.
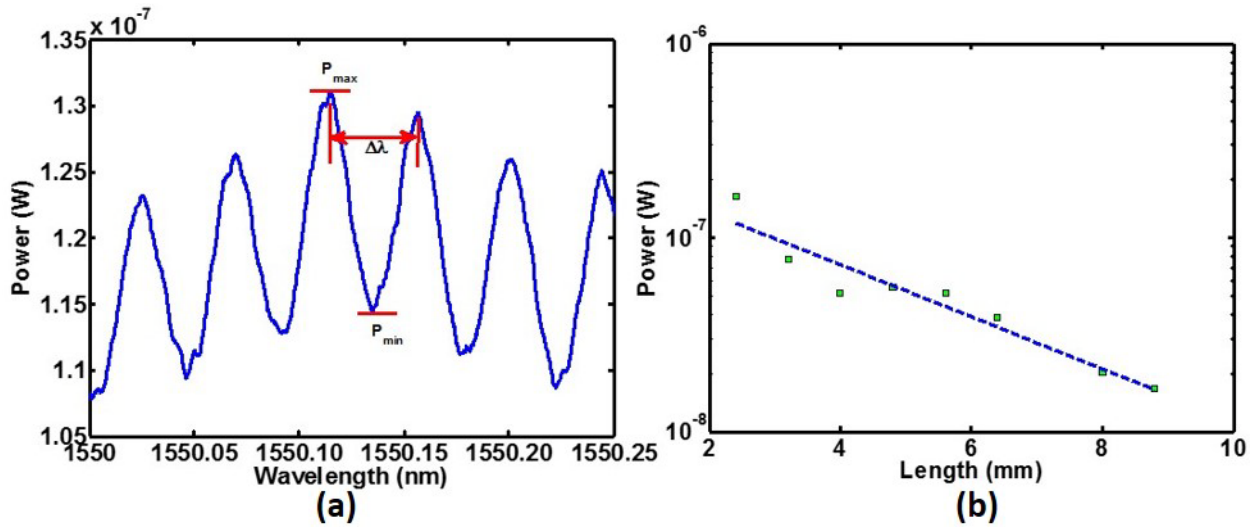
Figure 2-3: Linear propagation loss characterization of the SOS waveguides using (a) the FP method and (b) the cut-back method.

One challenge in processing SOS wafers is achieving high-quality waveguide facets because polishing sapphire is extremely difficult. Although the problem can be alleviated by partial dicing of sapphire substrates at the very first processing step and subsequent cleaving along the dicing marks, the quality of the polished facets of SOS waveguides is still worse than those of SOI waveguides. Moreover, the transmission window of SOS technology is limited by the transmittance of sapphire for wavelengths above 5 µm. In order to make polishing easier and obtain the largest possible transmission window, i.e., the low-loss transmission window of silicon (1.2-6.5 µm), two alternatives to SOS technology, SON and ASOP have been developed. The SON platform was achieved by bonding a silicon die to a SOI die coated with a silicon nitride layer using a spin-on-glass layer and subsequent removal of the SOI substrate [26], because SON wafers are not commercially available in the market. The ASOP platform was realized by direct bonding of an inverted SOI die to a bulk silicon die with trenches on it [27].

12

The details of the fabrication processes of these two novel waveguide technologies are stated in Ref. [26] and [27], respectively.

The measurement set-up for charactering the SON and ASOP waveguides at mid-IR wavelengths is shown in Fig. 2-4. The devices were tested using a Newport 3.39-µm HeNe laser with a continuous-wave (CW) output power of 2 mW. The laser was coupled through a ZnSe objective lens (5 mm focal length) into a mid-IR single-mode ZBLAN (a family of glasses with a chemical composition of ZrF_4-BaF_2-LaF_3-AlF_3-NaF) optical fiber from IRPhotonics, and then into the waveguides. The output of the chip was coupled into a lead selenide (PbSe) amplified detector (model# PDA20H from Thorlabs) through a mid-IR multimode metal halide fiber. The FP fringes were obtained by sweeping the temperature of the chip using a thermoelectric cooler (TEC) controller, as mid-IR tunable lasers are not yet available. The temperature was scanned at a speed of 0.1°C/sec. The signal-to-noise ratio (SNR) was further enhanced by mechanically chopping the laser at 700 Hz and using a lock-in amplifier to detect the modulated signal. Figure 2-5 presents the FP interference fringes recorded from the fabricated waveguides. The calculated loss (using Eq. (2.1)) of SON waveguides and ASOP (suspended membrane) waveguides are 5.2 dB/cm [26] and 2.8 dB/cm [27], respectively.
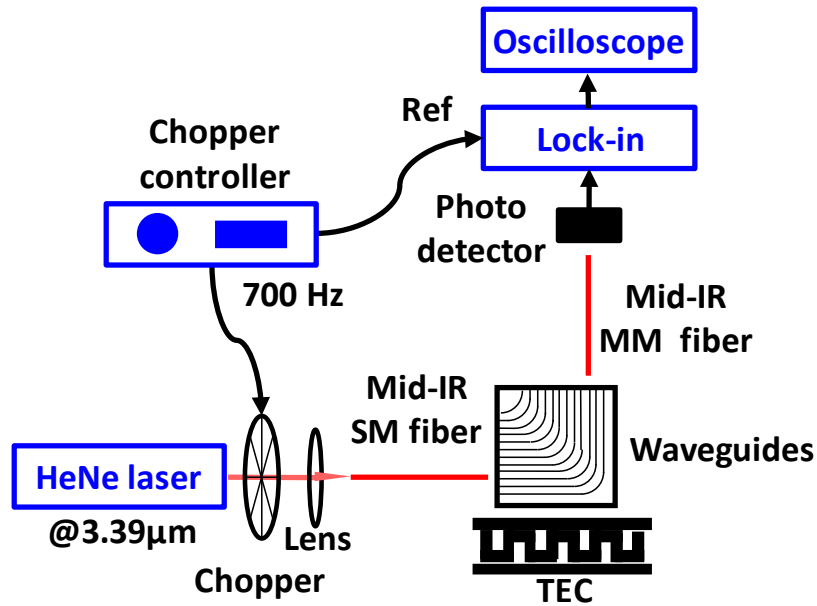
Figure 2-4: Schematic of the experimental mid-IR setup used to characterize the silicon-on-nitride and ASOP (suspended membrane) waveguides [26].
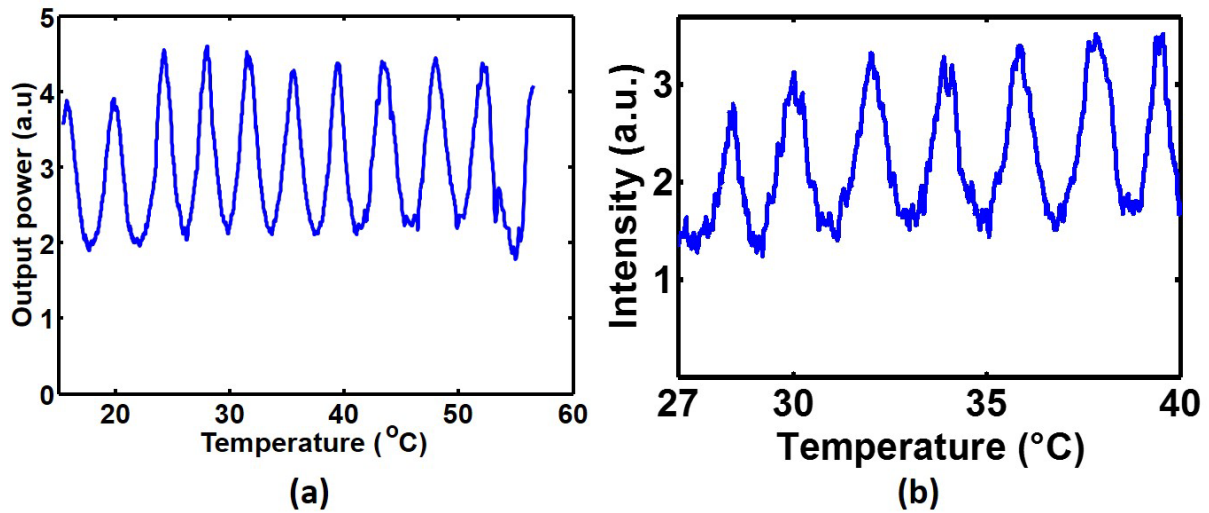
Figure 2-5: FP interference fringes at wavelength of 3.39 μm obtained by tuning the temperature of the chips for (a) SON waveguides [26] and (b) all-silicon suspended membrane waveguides [27].

2.3 Mid-IR Silicon Raman Laser

2.3.1 Background of Silicon Raman Lasers/Amplifiers

Historically, achieving optical gain and/or lasing in silicon has been one of the most challenging targets in silicon photonics because bulk silicon has an indirect electronic band structure and therefore has a very low light emission efficiency, i.e., low band-to-band radiative electron-hole recombination rate.

Alternatively, Raman scattering and stimulated emission has been pursued. The Raman effect is the inelastic scattering of a photon. When light is scattered from an atom, molecule or crystal, a small fraction of the scattered light is scattered by an excitation, with the scattered photons having a frequency different from, and usually lower than, the frequency of the incident photons. The stimulated Raman scattering (SRS) process actually is a combination of a Raman process with stimulated emission. It can be described as the interaction of the incoming pump with the vibrations in the medium to efficiently stimulate the creation of Stokes photons. The Raman shift, i.e., the frequency difference between the pump and Stokes waves of single-crystal silicon is 15.6 THz.

Observation of Raman emission in silicon was first reported in 2002 [30]. Both forward and backward spontaneous Raman scattering from SOI waveguides were measured at 1.54 µm with a 1.43 µm pump. In 2004, stimulated Raman scattering was used to demonstrate light amplification and lasing in silicon [31]. However, because of the nonlinear optical loss associated with TPA-induced free-carrier absorption (FCA), lasing was limited to pulsed bias operation. A continuous-wave silicon Raman laser (SRL) based on low-loss SOI rib waveguide,

pumped at 1550 nm wavelength, was demonstrated in 2005 [32]. TPA-induced FCA in silicon was significantly reduced by introducing a reverse-biased *p-i-n* diode straddling the SOI waveguide. The laser cavity was formed by coating the facets of the silicon waveguide with multilayer dielectric films, whose reflectivities were designed using the FP resonances. Other research on near-IR silicon Raman lasers/amplifiers include using silicon ring resonator instead of conventional single-pass-pumped silicon Raman amplifier to resonantly enhance the externally applied pump power [33], and injecting the pump power into a surrounding cladding instead of directly into the silicon core, which significantly increased the maximum achievable total gain of silicon Raman amplifiers [34]. Also, fourth quadrant biasing of the straddling diodes have been proposed and demonstrated to achieve energy harvesting in silicon Raman amplifiers [14].

Mid-infrared silicon Raman amplifier was first demonstrated in 2007 [17]. Because of the high loss of SiO_2 at mid-infrared wavelengths, a 2.5-cm-long bulk silicon ingot was used as the active medium and pumped with 5 ns pulses at 2.88 µm. The two facets of the silicon samples were coated with broadband anti-reflection coatings to prevent incurring Fresnel reflection losses. Two dichroic beam-splitters and a spectrometer were used as filters to separate the strong residual pump from the weak amplified Stokes signal. The time-resolved Stokes signal was detected using a cooled indium arsenide (InAs) detector. A gain of 12 dB was reported for a signal at 3.4 µm wavelength.

The behavior of Raman amplified Stokes signal and coherent anti-Stokes Raman scattered signal in presence of a noisy pump was studied [18]. It was experimentally determined that the Raman amplification process of the weak input stokes beam by a noisy pump source

16

follows *L*-shaped distribution. The distribution of pulse energy of 3000 pump pulses was found to follow a mean centric distribution, such as a Gaussian or a Rician distribution. Simultaneously, the Raman gain experienced by the Stokes beam was measured. The observed distribution clearly follows an *L*-shaped extreme value statistical behavior, highlighted by the high probability of the large outliers in the extended tail of the distribution. This is attributed to the inherently noisy pump source used in the experiments (Q-swtiched Nd-YAG laser pumped Optical Parametric Oscillator).

Under the assumption of undepleted pump, the evolution of the Raman Stokes intensity I_s along the propagation direction z is described as:

$$\frac{dI_s}{dz} = g_R I_p I_s \tag{2.2}$$

where I_p is the pump intensity, and g_R is the Raman gain coefficient, determined from the value of the third order Raman susceptibility $\chi^{(3)}$ [17]:

$$g_R = \frac{6\pi\mu_0}{\lambda_s n_s n_p} \chi^{(3)} \tag{2.3}$$

Equation (2.3) tells us that the Raman gain coefficient is proportion to $1/\lambda_s$. The gain coefficient measured in the near infrared (1550 nm) is in the range of 10~20 cm/GW [35]. So at the Stokes wavelength of 3.4 µm, the Raman gain coefficient is expected to be 4.5~9 cm/GW. It has been found in Raman amplification experiments in bulk crystals that the Raman gain scales down faster than the inverse wavelength scaling as predicted by theory [36].

17

2.3.2 Analytical Modeling of Mid-IR Silicon Raman Lasers

SRLs were first demonstrated in the near-IR regime [31,32]. The works were followed by several simulations on Raman lasers and amplifiers [37,38,39,40,41]. The longest wavelength experimentally reported in the near-IR is a cascaded laser operating at 1.848 µm [42]. Cascaded Raman lasers up to 3 µm and pumped at 1.55 µm have been studied based on fully numerical methods [39]. Here, an analytical model for mid-IR SRLs is developed for the first time. The model can be used to avoid time-consuming fully numerical simulations in the design and analysis of the devices. The model is validated by comparing it with numerical solutions of coupled-wave equations, and is used to predict the performance of the lasers.

With the absence of TPA and FCA at above 2.2 µm, the coupled-wave equations for Raman lasing lend themselves to analytical solutions, as developed here. This is in contrast to near-IR wavelengths where achieving accurate analytical solutions is difficult, if not impossible, and hence fully numerical simulation are usually employed [37,38,39,40,41]. The model is applicable to various silicon waveguide configurations as well as bulk silicon, coated or uncoated with dielectric or integrated mirrors, provided that the predicted pump intensities are achievable in practice. Figure 2-6(a) shows the schematic of the SRL analyzed in this work in which the input pump is injected from the left-hand side (LHS) and the output Stokes is from the right-hand side (RHS). As discussed later, a device in which the output is from the LHS was also studied but exhibited very similar performance. In either case, the device consists of a silicon waveguide of length L, whose facets are coated with multilayer dielectric films. A continuous wave (CW) pump laser (p) at wavelength λ_p is coupled into the LHS (l) of the cavity and the output Stokes

(*s*) wavelength λ_s is exited from the RHS (*r*) via stimulated Raman scattering. The reflectivities of the left and right mirrors at λ_p and λ_s are R_{pl}, R_{pr}, R_{sl} and R_{sr}, respectively.

A typical micron-size ridge waveguide with the geometry described in the caption of Fig. 2-6 was analyzed. Figure 2-6(b) shows the TE optical modes propagating in the SOS waveguide at both the pump and the Stokes wavelengths. The effective core area of the waveguide is ~3 μm^2. The overlap of the two modes, Γ, is calculated to be close to unity (99.75%). The overlap integral, Γ, is included in the following model for completeness. However, its value is assumed to be 1 for the present micron-size ridge waveguides. It is noted that Γ could be considerably smaller than unity in submicron waveguides.
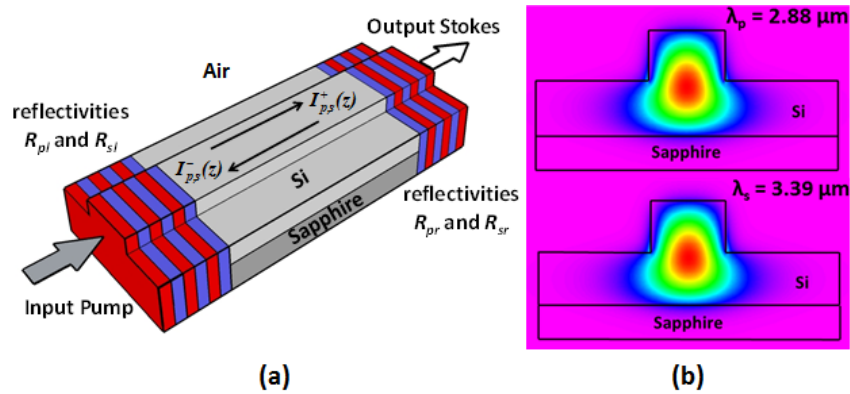
Figure 2-6: (a) Schematic of the studied mid-IR silicon Raman laser; (b) Optical mode profile (TE) at pump (top) and the Stokes (bottom) wavelengths in the SOS waveguide with air top-cladding having rib width of 2 µm, rib height of 2 µm and slab height of 1 µm. The calculations are obtained from a commercial numerical mode solver (BeamPROP by RSoft) [43].

As mentioned, TPA and FCA are negligible at mid-IR wavelengths. By also neglecting spontaneous Raman scattering at and above threshold, the evolution of the forward (+) and

backward (–) propagating pump and Stokes intensities are governed by the following coupled-wave equations [37]

$$\pm \frac{dI_p^\pm}{I_p^\pm dz} = -\alpha_p - \Gamma g_R \cdot \frac{\lambda_s}{\lambda_p}(I_s^+ + I_s^-), \tag{2.4a}$$

$$\pm \frac{dI_s^\pm}{I_s^\pm dz} = -\alpha_s + \Gamma g_R \cdot (I_p^+ + I_p^-) \tag{2.4b}$$

where g_R is the Raman gain coefficient, α_p and α_s are the linear propagation losses at λ_p and λ_s, respectively. The corresponding boundary conditions are

$$
\begin{aligned}
I_p^+(0) &= (1 - R_{pl})I_{in} + R_{pl}I_p^-(0), \\
I_p^-(L) &= R_{pr}I_p^+(L), \\
I_s^+(0) &= R_{sl}I_s^-(0), \\
I_s^-(L) &= R_{sr}I_s^+(L),
\end{aligned}
\tag{2.5}
$$

where I_{in} is the input pump intensity.

Equations (2.4) and (2.5) might be considered to be similar to the coupled-wave equations and boundary conditions of near-IR Raman fiber lasers (RFLs). Although several analytical and numerical models for RFLs have been published [44-49], each has its own shortcoming for the present case, as follows. F. Leplingard *et al*. simplified the numerical algorithm for solving the equations by transforming the two-point boundary value problem into an initial value problem, but the solution was still fully numerical [44]; The analytical solution developed by J. Zhou *et al*. assumed single pass pump, i.e., anti-reflection coated mirrors [45]; Other analytical models developed for RFLs assume zero left-mirror reflectivity at the pump wavelength (a simplifying valid assumption because of the low index of silica) [46,47,48,49]; Z. Qin *et al*. made the further simplifying assumption of zero residual pump power reflected back to

the input end [46]; S. A. Babin *et al.* not only assumed zero left-mirror reflectivity but also assumed that the output power increases linearly with the input [47]. However, none of these models are applicable to silicon Raman lasers because a considerable amount of pump power reflects back and forth between the right- and left-hand side mirrors into the cavity. Indeed, a variety of dielectric coated mirrors, with different reflectivities at pump and Stokes wavelengths are commonly considered in silicon Raman lasers. Therefore, in this work, nonzero left- and right- mirror reflectivities at both pump and Stokes wavelengths are included in the modeling of Raman lasers, for the first time, to account for silicon and other high-index material cases (the simplest example may be uncoated air-silicon interface with reflectivity of ~30% at both pump and Stokes). This will require developing a more complicated mathematical treatment of the problem, as presented here.

Comments should be made regarding the other nonlinear processes that may influence the performance of SRLs. Stimulated Brillouin Scattering (SBS) presents a serious problem in RFLs. However, SBS can be ignored in SRLs as the Brillouin scattering coefficient for silicon is two orders of magnitude smaller than the Raman gain coefficient [50]. 3PA and associated free-carrier effects are also negligible because the corresponding coefficient for silicon is very small [25]. Degenerate FWM between the pump and the generated Stokes waves can be discarded as the phase matching condition cannot be satisfied due to the large difference of the interacting wavelengths. Therefore, only SRS is considered in Eq. (2.4). This assumption is consistent with previous works on SRLs [37,39,40].

The above differential equations with the boundary conditions can be solved numerically by collocation. However, an initial guess is usually required for numerical methods. In our case,

this guess is difficult to find because zero Stokes intensity is always a possible solution even when the pump intensity is above lasing threshold. Therefore, an analytical solution to this boundary-value problem is developed. The presented solution can be utilized not only as an initial guess for numerical solvers but also as a fully-analytical model.

First, the geometric mean intensity $\bar{I}_{p,s}^{1/2} = (I_{p,s}^{+} I_{p,s}^{-})^{1/2}$ and the gain factor $G_{p,s}(z) = 1/2 \ln I_{p,s}^{+}(z)/I_{p,s}^{-}(z)$ are defined [44,45,46,47,48,49]. $\bar{I}_{p}$ and $\bar{I}_{s}$ are constant, i.e., they are independent of z. As a result, Eqs. (2.4) and (2.5) can then be rewritten in terms of $\bar{I}_{p,s}$ and $G_{p,s}(z)$. A linear dependence of $G_{p,s}(z)$ on z is also assumed, i.e.,

$$G_{p}(z) = G_{p}(0) + z[G_{p}(L) - G_{p}(0)]/L. \tag{2.6}$$

This linear assumption implies that the pump depletes exponentially in both forward and backward directions. The validity of this linear dependency assumption was confirmed by comparison with fully numerical solutions (Fig. 2.5).

Based on the above, the threshold intensity of the silicon Raman laser is obtained as

$$I_{th} = \frac{\alpha \delta_{s}(1 - R_{pl}e^{-2\delta_{p}})(e^{\delta_{p}} - R_{pl}e^{-\delta_{p}})}{g_{R}(1 - R_{pl})(1 - e^{-\alpha L})(1 + R_{pr}e^{-\alpha L})}, \tag{2.7}$$

where

$$\delta_{p} = \alpha L + 1/2 \ln(1/R_{pr}), \tag{2.8a}$$

$$\delta_{s} = \alpha L + 1/2 \ln(1/R_{sl}R_{sr}) \tag{2.8b}$$

are loss factors of the pump and Stokes waves due to linear propagation loss and mirror transmission losses. By defining

$$L_{p,s}(z) = L\frac{\sinh[G_{p,s}(z)] - \sinh[G_{p,s}(0)]}{G_{p,s}(L) - G_{p,s}(0)}, \tag{2.9}$$

above threshold, $\bar{I}_p$ can be solved from

$$\bar{I}_p^{1/2} = \delta_1 /[2g_R L_p(L)]. \tag{2.10}$$

Consequently, the geometric mean intensity and gain factor of the Stokes wave are obtained from

$$\bar{I}_s^{1/2} = \lambda_p[G_p(0) - \delta_0]/[2g_R \lambda_s L_s(L)], \tag{2.11}$$

$$G_s(z) = G_s(0) - \alpha z + 2g_R \bar{I}_p^{1/2} L_p(z). \tag{2.12}$$

$G_{p,s}(z)$ and $G_{p,s}(L)$ are easily obtained from Eq. (2.5). Finally, the intensity distributions for the pump and Stokes wave are

$$I_{p,s}^{\pm}(z) = \bar{I}_{p,s}^{1/2} \exp[\pm G_{p,s}(z)], \tag{2.13}$$

and the output of the laser at the Stokes wavelength on the RHS of the waveguide in Fig. 2-4(a) is finally

$$I_{out} = (1 - R_{sr})I_s^{+}(L). \tag{2.14}$$

An equation similar to Eq. (2.14) can be easily obtained if the laser output beam is at the LHS, i.e., the case where the laser output and input beams are counterpropagating.

The above general model was applied to specific examples. In all the following numerical and analytical solutions, a pump wavelength of 2.88 µm is used [17,18]. The corresponding Stokes wavelength is 3.39 µm according to silicon's optical phonon energy. The experimentally estimated Raman gain coefficient g_R of 9 cm/GW at these wavelengths was employed [17].

A non-coated 2-cm long-cavity was first analytically modeled by assuming that reflectivities at both pump and Stokes wavelengths were 30%. Fully numerical simulation to coupled-wave equations was also carried out for this special case by using the results from the analytical method as guesses for the initial solution. Figure 2-7(a) presents the comparison between the analytical and numerical solutions. The intensity distributions of the pump and Stokes waves in the laser cavity for an input intensity of $I_{in} = 200$ MW/cm^2 are plotted using both methods. Such pump intensities can be attained in practice by solid-state mid-IR lasers (e.g., optical parametric oscillators) [17,18]. Also shown in the inset of Fig. 2-7(a) is the input-output (light-light) characteristic of the laser. It is clearly evident that the results have excellent agreement. The validity of the model was rigorously tested under other boundary condition examples not presented here. Meanwhile, the analytical model is proved to be much faster than the traditional numerical way of solving this set of equations. For example, the time consumed for plotting the inset of Fig. 2-7(a) is 200 times faster than numerical simulations. Therefore, our analytical model can be confidently used as a convenient and efficient tool in design and optimization of mid-IR SRLs. The results of Fig. 2-7(a) also suggest that at mid-IR wavelengths, where TPA and FCA are negligible, it is possible to pump a non-coated CW SRL above threshold with a reasonable pump intensity of around 100 MW/cm^2. It is reminded that CW near-IR SRLs are not achievable at any pump intensity without using appropriate mirror coatings on top of employing the carrier sweep-out technique to reduce the carrier lifetime [32].
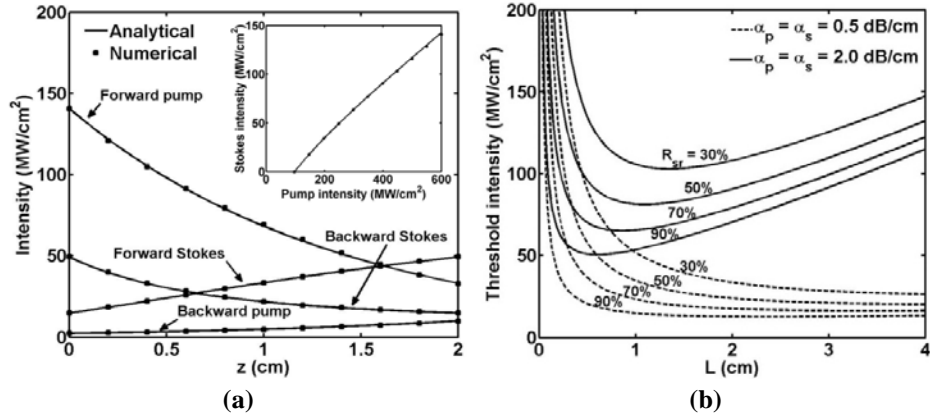
Figure 2-7: (a) Intensity distributions of pump and Stokes waves with I_{in} = 200 MW/cm^2. $R_{pl} = R_{pr} = R_{sl} = R_{sr} = 30\%$, $\alpha_p = \alpha_s = 0.5$ dB/cm and $L = 2$ cm were assumed. The inset shows the input-output characteristics of the Raman laser; (b) Threshold intensity versus cavity length for various output facet reflectivities and propagation losses and for $R_{pl} = 10\%$, $R_{pr} = R_{sl} = 90\%$ [43].

Using the described analytical model, it is easy to analyze mid-IR SRLs and optimize their design parameters. Indeed, achieving all the following results would have been extremely challenging and time-consuming based on fully numerical models. Figure 2.7(b) shows the threshold intensity as a function of L for different right facet reflectivities and two different linear propagation losses of 0.5 and 2.0 dB/cm. Unlike near-IR SRLs that have no lasing threshold outside a limited range of lengths [40], mid-IR silicon waveguide cavities can lase for any given length if enough pump power is available. Also, it is evident that for fixed reflectivities, there is an optimum length, where the lasing threshold reaches a minimum. This is more remarkable at the higher studied propagation loss (2.0 dB/cm), as an optimum length of $< \sim$ 1 cm can be recognized.

Figure 2.8 shows the influence of the cavity parameters, length and facet reflectivities, on the energy conversion efficiency of the lasers, defined as I_{out}/I_{in}. Generating each 3D plot in Fig. 2-8 was achieved in about 10 minutes with a typical desktop PC (with a 3 GHz Intel(R) Core(TM)2 Duo CPU), while it can take days to make similar plots based on fully numerical methods. However, our analytical model offers an efficient way to optimize the design of mid-IR SRLs. In this case, L and R_{sr} could be optimized under certain pump intensities. For linear propagation loss of $\alpha_p = \alpha_s = 0.5$ dB/cm, maximum conversion efficiencies of 55.8% and 45.1% are obtained at input intensities of $I_{in} = 200$ and 100 MW/cm^2, respectively (Fig. 2-8(a) and (c)). Such high conversion efficiency have been previously estimated based on fully numerical simulations and indicate that silicon Raman lasers in the mid-IR can attain performances comparable to near-IR fiber Raman lasers [39]. The lasers' efficiency, however, drop quickly for devices with the higher loss, i.e., $\alpha_p = \alpha_s = 2.0$ dB/cm. The maximum conversion efficiency obtained are 30.5% and 13.5% at input intensities of $I_{in} = 200$ and 100 MW/cm^2, respectively (Fig. 2-8(b) and (d)). The optimum lengths are below 0.4 cm in these two cases. Further increasing the length will result in higher lasing threshold and lower slope efficiency at the same time. Nonetheless, these predictions indicate a key advantage of mid-IR lasers, as compact laser cavities can be demonstrated. In comparison, up to 5 cm lengths are required at near-IR wavelengths [32]. It is noted that even more compact devices can be envisioned using ring resonator Raman lasers, as reported in the near-IR [50]. However, the study of such lasers is beyond the scope of this work.

The maximum conversion efficiencies achievable for four propagation loss values are plotted versus pump intensity in Fig. 2-9. For devices with the lowest loss, i.e., $\alpha_p = \alpha_s = 0.1$

dB/cm, the maximum possible conversion efficiency is ~73%. This could be considered as a practical limit for the efficiency of a mid-IR SRL assuming extremely low-loss silicon waveguides. Pumping the laser with intensities above 200 MW/cm^2 is unnecessary in this case as it could hardly improve the conversion efficiency. For devices with higher loss, i.e., $\alpha_p = \alpha_s = 1.0$ or 2.0 dB/cm, the conversion efficiency has not yet reached saturation at an intensity of 500 MW/cm^2. The minimum achievable lasing thresholds for the four propagation loss values are recognizable by the intersections of the curves with the *x*-axis.
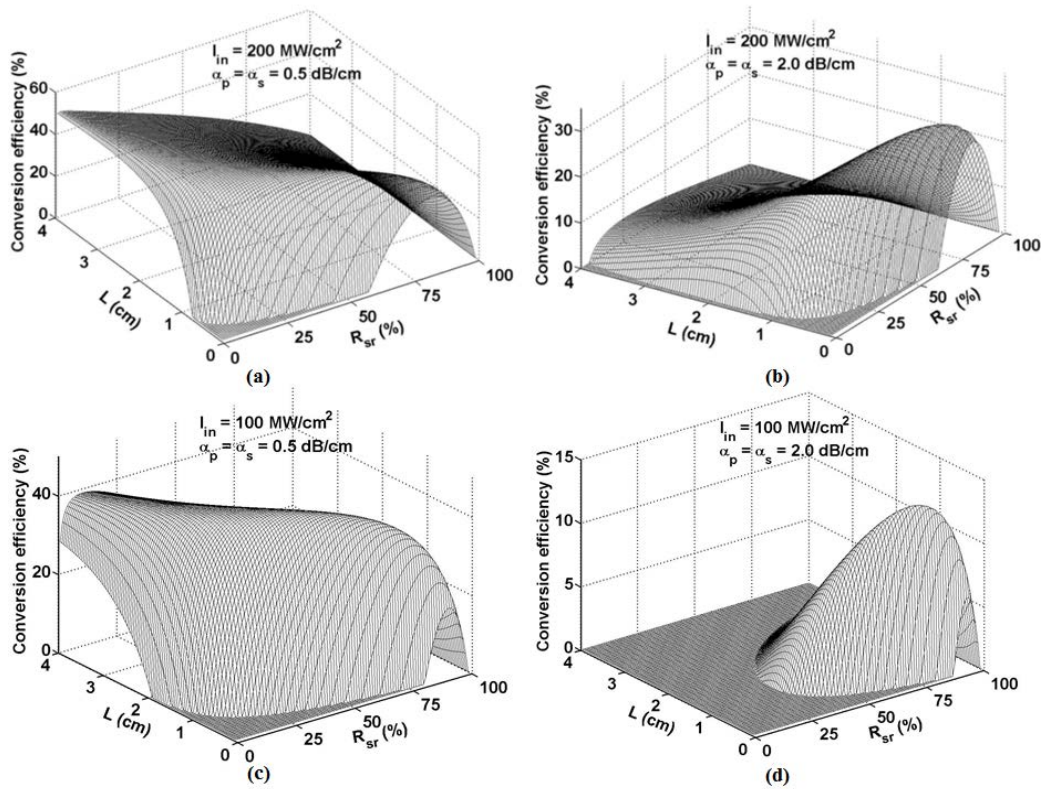
Figure 2-8: Conversion efficiency versus cavity length *L* and output facet reflectivity *R_sr* for two propagation loss values and two pump intensities [43].
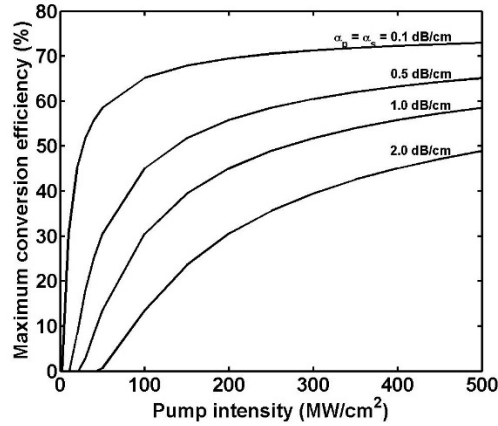
Figure 2-9: Maximum conversion efficiency versus pump intensity for four different propagation loss values [43].

It is noted that unlike Raman amplifiers whose gain depends on whether a co- or counter-propagating scheme is employed [40], our studies on mid-IR SRLs suggest that there is little dependency of the devices' conversion efficiency on the propagation directions of the pump and the output Stokes wave. This difference between Raman amplifiers and lasers can be attributed to the fact that the asymmetric impact of the nonuniform pump distribution along the waveguide is more pronounced in amplifiers–whose Stokes signal is typically passed a single time through the waveguide-as opposed to lasers whose Stokes output wave experiences several roundtrips in the cavity.

2.3.3   Pump-to-Stokes RIN Transfer of Mid-IR Silicon Raman Lasers

The Rician distribution of pump amplitude fluctuations has been shown to have a significant impact on the pulse-to-pulse gain statistics of mid-IR Raman amplifiers [18]. Similarly, the relative intensity noise (RIN) transferred from the instability of the pump source to the output Stokes can have a significant impact on the performance of mid-IR SRLs. The RIN

transfer has been theoretically and experimentally studied in Raman fiber lasers [51], and has been numerically simulated in near-IR silicon Raman amplifiers and lasers [52,53,54]. In this paper, the impact of RIN transfer on the performance of mid-IR SRLs is investigated for the first time.

Unlike the above model for the light-light characteristics, the governing equations for RIN transfer in SRLs do not lend themselves to analytical solutions. To estimate the effect of RIN transfer from the pump to the Stokes output, the noise component at angular frequency Ω in the pump noise spectrum is considered. The intensity fluctuations of the pump and the Stokes wave, normalized to the average intensities, are represented by $m_p^\pm(z)$ and $m_s^\pm(z)$, respectively:

$$I_p^\pm(z,t) = \bar{I}_p^\pm(z)[1 + m_p^\pm(z)\exp(i\Omega t)], \qquad (2.15a)$$

$$I_s^\pm(z,t) = \bar{I}_s^\pm(z)[1 + m_s^\pm(z)\exp(i\Omega t)], \qquad (2.15b)$$

where $\bar{I}_p^\pm(z)$ and $\bar{I}_s^\pm(z)$ are time-independent average intensities. $m_p^\pm(z)$, $m_s^\pm(z)$ are complex values satisfying $\left|m_p^\pm(z)\right|, \left|m_s^\pm(z)\right| << 1$. The input pump is assumed to be modulated by a sinusoidal function at angular frequency Ω, i.e., $I_{in} = \bar{I}_{in}[1 + m_{in}\exp(i\Omega t)]$, where m_{in} is a small real number. The different values of pump and Stokes group velocities, v_p and v_s, should be accounted for similar to Raman amplifiers [52,53]. This leads to reduced RIN transfer:

$$\pm\frac{\partial I_p^\pm}{\partial z} + \frac{1}{v_p}\frac{\partial I_p^\pm}{\partial t} = -\alpha_p I_p^\pm - g_R \cdot \frac{\lambda_s}{\lambda_p}(I_s^+ + I_s^-)I_p^\pm, \qquad (2.16a)$$

$$\pm\frac{\partial I_s^\pm}{\partial z} + \frac{1}{v_s}\frac{\partial I_s^\pm}{\partial t} = -\alpha_s I_s^\pm + g_R \cdot (I_p^+ + I_p^-)I_s^\pm. \qquad (2.16b)$$

Substituting Eq. (2.15) into Eqs. (2.16) and (2.5) and neglecting higher order fluctuation terms, a total of eight coupled differential equations and eight boundary conditions can be obtained. This is a somewhat more complicated problem compared to the only four [52] or six (to account for carrier density noise [53]) equations and boundary conditions that ought to be solved for silicon Raman amplifiers. The equations for steady state operation and corresponding boundary conditions can be obtained by replacing $I_{p,s}^{\pm}$ in Eqs. (2.4) and (2.5) with $\bar{I}_{p,s}^{\pm}$ and solved using the analytical model mentioned above. The other four coupled equations and four boundary conditions that describe the small fluctuations on the pump and Stokes waves along transmission length z are derived as:

$$\frac{dm_p^{\pm}}{dz} = \mp \frac{i\Omega}{v_p} m_p^{\pm} \mp g_R \frac{\lambda_s}{\lambda_p} (\bar{I}_s^+ m_s^+ + \bar{I}_s^- m_s^-),$$ (2.17a)

$$\frac{dm_s^{\pm}}{dz} = \mp \frac{i\Omega}{v_p} m_s^{\pm} \pm g_R (\bar{I}_p^+ m_p^+ + \bar{I}_p^- m_p^-),$$ (2.17b)

$$\begin{aligned}
&\bar{I}_p^+(0)m_p^+(0) = (1 - R_{pl})\bar{I}_{in}m_{in} + R_{pl}\bar{I}_p^-(0)m_p^-(0), \\
&m_p^-(L) = m_p^+(L), \\
&m_s^+(0) = m_s^-(0), \\
&m_s^-(L) = m_s^+(L).
\end{aligned}$$ (2.18)

Equations (2.17) and (2.18), together with the steady-state equations, can be numerically solved using the collocation method, from which the RIN transferred from the pump to the Stokes is calculated as

$$T_{RIN}(\Omega) = \frac{\left| m_s^+(L,\Omega) \right|^2}{m_{in}^2}.$$ (2.19)

30

The RIN transfer in a SRL with a linear waveguide loss of 0.5 dB/cm and for an optimized pump intensity of 100 MW/cm^2, i.e., $L = 1.20$ cm, $R_{sr} = 38\%$ (assuming $R_{pl} = 10\%$ and $R_{pr} = R_{sl} = 90\%$), was numerically evaluated. Noise frequencies ranging from zero to tens of gigahertz were included. The group velocity at the pump wavelength in Eqs. (2.16(a)) and (2.17(a)) was calculated as $v_p = c/n_{eff}$, where c is the speed of light in vacuum and n_{eff} is the effective index of the silicon waveguide at pump wavelength. The group velocity at the Stokes wavelength was obtained from $v_s = 1/[(\lambda_s - \lambda_p)D + 1/v_p]$, where $D = -120$ ps/(nm.km) is the local group-velocity dispersion in silicon calculated by the Sellmeier equation. This material dispersion dominates the waveguide dispersion in the studied large cross-section waveguides. This was validated by RSoft calculations and is consistent with previous works [52,53,54]. Finally, $m_{in} = 0.01$ is assumed in our simulation but even higher values for this quantity changes the following calculations insignificantly.

Figure 2-10(a) presents the pump-to-Stokes RIN transfer spectrum for pump intensities of 50, 75, 100 and 200 MW/cm^2. It is evident that the RIN transfer remains constant at low frequencies, then starts to oscillate at the free-spectral range (FSR) of the laser cavity, i.e., $\Delta v = c/(2n_{eff}L) = 3.6$ GHz. The observed strong oscillations at higher frequencies suggest that laser sources with RIN spectra no wider than a few GHz are required for pumping mid-IR lasers with cavity lengths of ~ 1 cm. The low-frequency transferred RIN, as well as the magnitude of the high-frequency oscillations, drop as the pump power increases. This is consistent with theoretical and experimental RIN transfer spectrum of Raman fiber lasers [51]. The low-frequency RIN transfer for the SRL could be above 12 dB when pumped at 50 MW/cm^2, and drops to below 1 dB at a pump intensity of 200 MW/cm^2.

31

Results very close to Fig. 2-10(a) were obtained for the case in which the laser output and the input pump are counterpropagating. This differs from Raman amplifiers that show a higher RIN bandwidth for the copropagation scheme as compared with the counterpropagation scheme [52].
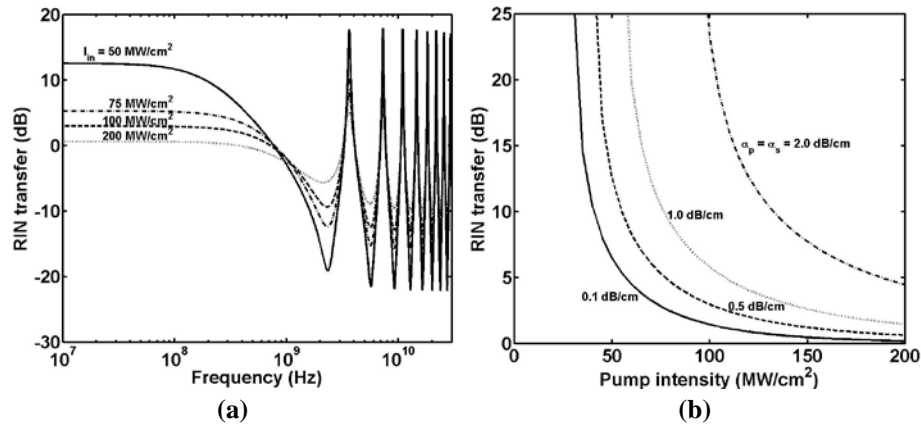
Figure 2-10: (a) RIN transfer spectra for mid-IR SRLs pumped at 50, 75, 100 and 200 MW/cm^2 and (b) the devices' low frequency RIN transfer versus pump intensity for four propagation loss values. Modal parameter: $L = 1.20$ cm, $R_{sr} = 38\%$, $\alpha = 0.5$ dB/cm (optimized design for $I_{in} = 100$ MW/cm^2), $D = -120$ ps/(nm·km) [43].

Figure 2-10(b) summarizes the low-frequency RIN transfer versus pump intensity under different propagation loss values. The RIN transfer observed goes to infinity right below the lasing threshold and decreases with increasing pump intensity. Also evident is the noticeable increase in the low-frequency RIN transfer with increasing propagation loss. Unlike near-IR SRLs, in which the RIN transfer is strongly affected by FCA [53], the RIN transfer in mid-IR lasers is mainly determined by the linear propagation loss and the pump intensity. Therefore, pumping at well-above lasing threshold and reducing the linear loss of silicon waveguides are two crucial requirements for decreasing the RIN transfer in mid-IR SRLs.

32

2.3.4 Experimental Results on Mid-IR Silicon Raman Lasers

No experimental work on mid-IR SRLs has yet been reported to the best of our knowledge. It is, nonetheless, mentioned that demonstration of 3.4 µm mid-IR SRLs has been attempted by us. We first observed spontaneous Raman emission in an uncoated 1-inch thick bulk silicon using the laser systems of CREOL's Nonlinear Optics Group. The set-up is shown in Fig. 2-11. The pump laser (2.88 µm) was an optical parametric oscillator (OPO) operating under pulsed condition with a pulse width of 11~14 ps and repetition rate of 10 Hz. The visible source was used for optical alignment purposes only. The polarization of the beam from OPO was set to the vertical direction using the Babinet-Soleil compensator so that the transmittance of the monochromator reached its maximum. A single CaF_2 plano-convex lens was used to focus the pump into the silicon sample. At the output end another CaF_2 plano-convex lens was used as the imaging lens. A monochromator was used to filter the residual pump, leaving only the Raman emission at the Stokes wavelength. The Stokes wave was detected using a cooled gold doped germanium detector and observed with an oscilloscope.
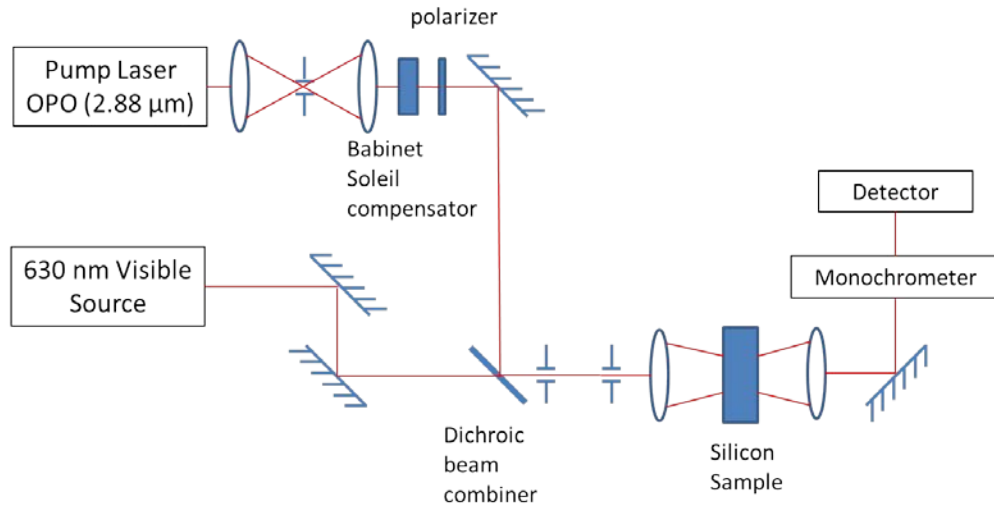
Figure 2-11: Set-up used for mid-IR Raman lasing in bulk silicon.

No Raman lasing was observed because the sample was not coated, and more importantly, the cavity photon lifetime of the FP cavity τ_p is around 70 ps ($1/\tau_p$ = -$1/2(v_g/L)\log(R_1R_2)$) for lossless cavity, where v_g is the group velocity, L is the length of the cavity, and R_1, R_2 are reflectivities of the facets), much longer than the pulse width of the OPO. However, an increase in the output power after the filters was observed when the silicon sample is placed in the path, which indicated that spontaneous Raman scattering was taking place inside silicon. The increase in the output power is roughly estimated as the generated Stokes signal. The result is shown in Fig. 2-12 (only forward scattering). The slope efficiency of the spontaneous Raman emission is estimated to be 6×10^{-5}. The fluctuations in the output power might be explained by extreme value statistics in silicon.
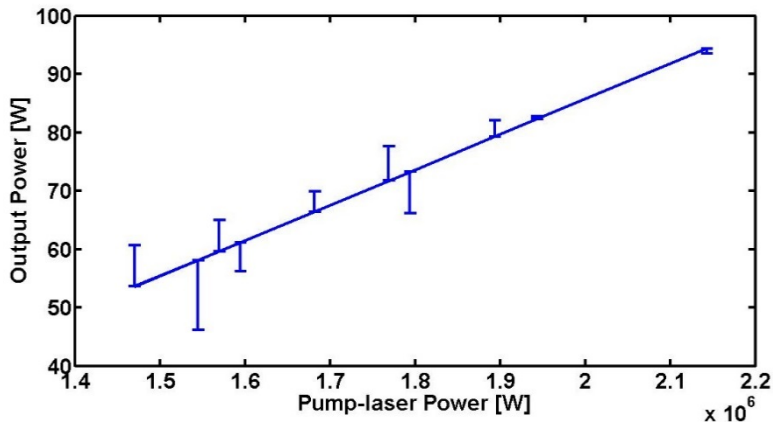
Figure 2-12: Spontaneous Raman emission as a function of pump power.

Later we had the 1-inch thick bulk silicon coated with appropriately designed dielectric mirrors and tried the same experiment at UCLA, using VIBRANT IR Model 2731 optical parametric oscillator by OPOTEK, Inc. as the pump source, which has a pulse width of ~ 5 ns, much longer than the cavity photon lifetime as well as the Raman response time of silicon (~3 ps [55]). Although spontaneous Raman emission was certainly observed and the bulk device was perhaps at or slightly above threshold (Fig. 2-13), the low average power and the poor beam quality of the employed pump source prevented definite and undisputable confirmation of lasing. It is our belief that optical waveguiding would alleviate some of these issues provided that low-loss mid-IR silicon waveguides and efficient coupling schemes are simultaneously employed.
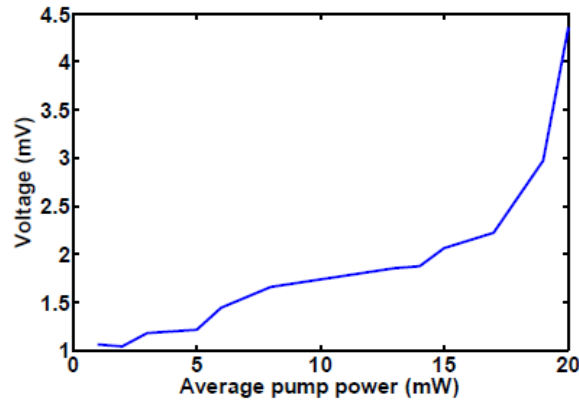
Figure 2-13: Measured signal at 3.4 µm from a 1-inch-thick bulk silicon sample coated with dielectric mirrors designed for Raman lasing at this wavelength and pumped with a nanosecond OPO at a wavelength of 2.88 µm.

2.4   Mid-IR Nonlinear Silicon Photonics Using the Kerr Effect

Third-order nonlinear susceptibility ($\chi^{(3)}$) based on Kerr effect is especially important in silicon as it exhibits a wide variety of phenomena such as four-wave mixing (FWM) and self-phase modulation (SPM) [1, 56]. Among others, two of the useful nonlinear functionalities that have been pursued in the near-IR in SOI waveguides are wavelength conversion and parametric amplification (based on FWM) and continuum generation (based on SPM). Demonstrating these two functionalities on SOS waveguides in the mid-IR range is proposed here.

At near-IR, a figure of merit (FOM), defined as $n_2(\lambda)/\beta_{TPA}\lambda$ (n_2 is the nonlinear coefficient and β_{TPA} is the TPA coefficient), is often used to compare the strength of the Kerr effect and the nonlinear absorption. However, FOM may be irrelevant at > 2.2 µm, since $\beta_{TPA} \approx 0$. Instead, the conventional nonlinear parameter, $\gamma = 2\pi n_2(\lambda)/A_{eff}\lambda$ [57] will play a dominant role (A_{eff} is the effective waveguide area). Not only the Kerr effect is somewhat weaker in the mid-IR

36

[58,59], but also the larger λ (compared to near-IR) reduces γ. Nonetheless, due to lower nonlinear losses (TPA and FCA), FWM on SOI waveguides perform better at ~ 2.2 μm when compared to ~ 1.5 μm [19,20]. n_2 at > 2.35 μm is not yet measured to the best of our knowledge. Theoretical calculations were published that predict n_2 values of 3.67 to 3.26×10^{-5} cm^2/GW for λ varying from 3.39 to 4.26 μm [60].

2.4.1   Mid-IR Continuum Generation Sources

Continuum generation is formed when several nonlinear processes act together upon a pump beam in order to cause spectral broadening of the original pump beam, whereas the spatial coherence usually remains high. The spectral broadening is usually accomplished by propagating optical pulses through a strongly nonlinear device.

A lot of studies on continuum generation in guided-wave structures, such as single-mode fibers [61] or photonic-crystal fibers [62] have been reported. These studies suggest that continuum generation can be achieved at low optical power and short propagation distances, if the guiding medium has tunable dispersion properties and high nonlinear response. Although efficient continuum generation is shown in previous studies on PCF, its use in on-chip integration applications is limited by the large propagation length required for inducing large spectral broadening.

An alternative means to overcome this limitation is silicon waveguides, which have several unique properties that can be employed to achieve on-chip supercontinuum generation [63]. Because silicon waveguides have small transverse dimensions, their dispersion properties are governed mainly by the waveguide dispersion. As a result, tunable dispersion properties can

be achieved by carefully designing the transverse waveguide dimensions. In addition, because of high optical confinement in silicon waveguides due to the high index contrast between silicon and the surrounding media (such as SiO_2), large optical intensities are achieved inside the guiding layer. Furthermore, silicon has higher material nonlinearity. These advantages make the effective nonlinear coefficient in silicon waveguides several orders higher than that in a low-confinement optical fiber.

The group-velocity dispersion (GVD) has a great impact on nonlinear pulse propagation. The efficiency of continuum generation is greatly enhanced if the input pulse is launched in the anomalous dispersion regime, near the zero-group velocity dispersion (ZGVD) point. Silicon has significant normal dispersion over its transparent spectral region beyond 1.2 µm. However, the dispersion introduced by mode confinement provided by waveguide geometry can be used to compensate for the material dispersion. The wavelength dependence of β_2 is illustrated clearly in Ref. [64]. By changing the size and aspect ratio of a rectangular SOI waveguide, the ZGVD point can be designed to lie anywhere from 1.2 µm to beyond 3 µm. It is also shown that quasi-TE modes are more sensitive to the waveguide width, while quasi-TM modes are more sensitive to the waveguide height. A good explanation to this phenomenon is the GVD for a mode is determined by the boundaries where the electric field is discontinuous.

There are several studies on continuum generation at near-IR wavelengths in SOI waveguides [1,56]. It has been shown that TPA is the main predicament for achieving high brocading factors [65]. It is hence expected that higher broadening can be most likely observed in the mid-IR. For $\lambda_0 = 3.85$ μm, a channel SOS waveguide with a width of 0.9 µm and height a 0.5 µm was designed using a commercial beam propagation method solver (BeamPROP). The

38

spectral broadening of a 80 fs transform-limited input pulses in this SOS waveguide and with an optimized length of 0.5 cm was calculated by numerically solving the nonlinear Schrödinger equation using an in-house Matlab code. A 3-dB broadening factor of up to 6 is predicted (Fig. 2-14) for a pump intensity of ≤ 200 GW/cm^2, which is below the threshold damage of silicon for sub-picosecond pulse widths [66]. The predicted broadening factors are indeed higher than those in SOI waveguides in the near-IR [65].
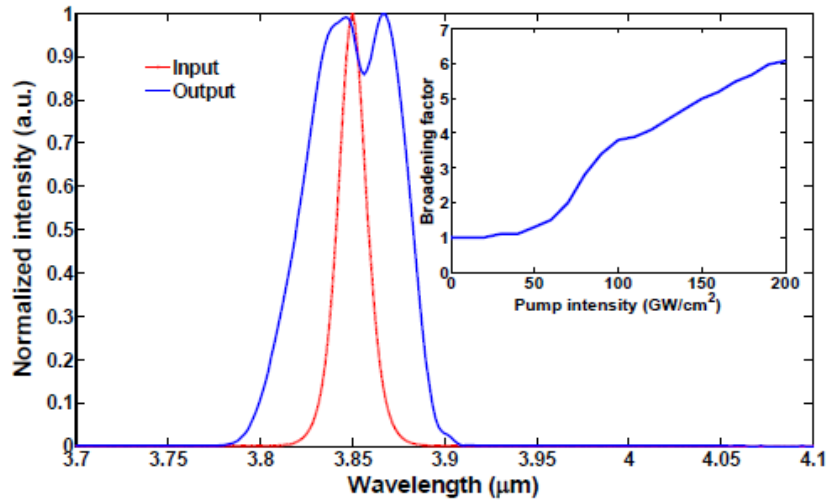
Fig. 2-14: Input/output spectra of continuum generation in an SOS waveguide at pump intensity of 96 GW/cm^2. The inset plots the broadening factor versus pump intensity.

2.4.2 Mid-IR Optical Parametric Amplifiers

FWM-based parametric amplification has a large gain bandwidth (usually tens of nanometers or even more), which is a significant advantage over stimulated Raman amplification. However, unlike the Raman-based devices that are only sensitive to the pump intensity, parametric amplifiers require phase matching to achieve wideband operation, i.e., the

39

device must operate in the anomalous dispersion regime that can be achieved by dispersion engineering via proper waveguide design. Successful parametric gain and wavelength conversion have been demonstrated around the communication wavelength of 1.55 µm and in the 2-2.5 µm range [19,20]. According to the dispersion calculations based on numerical simulations of waveguide effective indices using BeamPROP by RSoft, broad band (3.0-3.8 µm) anomalous dispersion can be achieved in 1.5-µm-wide and 0.5-µm-high SOS waveguide. In Section 3.3, the gain and noise figure (NF) of a mid-IR silicon OPA pumped at 3.4 µm are simulated numerically.

2.5   Vertical-Cavity Silicon Raman Amplifier

2.5.1   Background

Our proposed idea of vertical-cavity silicon Raman amplifier (VCSRA) arises from vertical cavity semiconductor optical amplifiers (VCSOAs), which are in principle vertical-cavity surface-emitting lasers (VCSELs) operated below lasing threshold. As a background, it has to be mentioned that VCSELs have been studied extensively for use in fiber-optic networks and optical interconnects due to its compatibility with low-cost wafer scale fabrication and testing methods [67]. A review of VCSELs is beyond the scope of this work and can be found elsewhere.

VCSOAs are FP amplifiers that share the same fabrication advantages as VCSELs. As an alternative to fiber amplifiers, VCSOAs are interesting devices for a wide range of applications in optical communication systems [67]. VCSOAs have been demonstrated at all important

telecommunication wavelengths including 980 nm, 1300 nm and 1550 nm [68]. The vertical-cavity design gives VCSOAs several advantages over in-plane devices such as higher coupling efficiency to optical fibers, polarization independent gain, small form factor, and possibility of fabricating 2-D arrays on wafer.

The proposed VCSRA is similar in design to a VCSOA. It is composed of a gain region sandwiched between two distributed Bragg reflectors (DBRs) which allow the gain to build up, as shown in Fig. 2-15. Different from VCSOAs, in VCSRAs, Raman scattering is used as the gain mechanism for signal amplification instead of stimulated emission. This means unlike VCSOAs that are usually electrically pumped, VCSRAs are optically pumped. The entire structure is undoped, which simplifies processing and minimizes optical losses. VCSRAs have two modes of operation: co-directionally propagating (reflection mode) and counter-directionally propagating (transmission mode), as illustrated in Fig. 2-15.
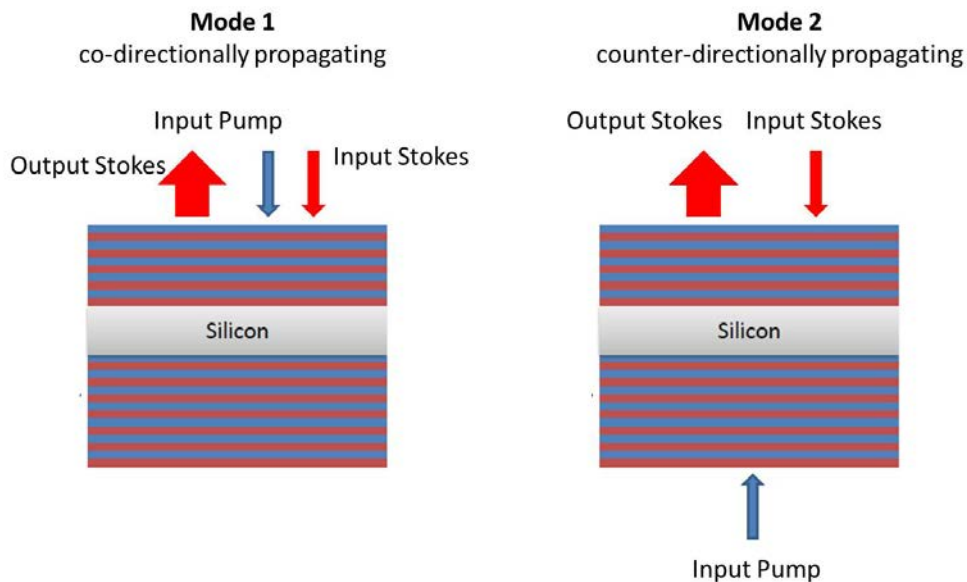
Figure 2-15: Schematic of VCSOAs showing co-directionally propagating mode (left) and counter-directionally propagating mode operation (right).

41

VCSRAs can operate at both near- and mid-infrared. Demonstration of mid-IR Raman amplification in a piece of uncoated bulk silicon was mentioned in Section 2.1. Proper design of the DBRs will help boosting the total signal gain.

2.5.2   Design of Mirror Reflectivities

Design of mirror reflectivities is crucial in the design of VCSRAs. If the reflectivities are too low, there will not be enough feedback to reach sufficient gain. However, if the mirror reflectivities are too high, the device starts to lase. Therefore, the reflectivities should be just low enough so that lasing threshold is not reached when the amplifier is optically pumped.

Similar to mid-IR silicon Raman lasers, the coupled-mode equations that govern the evolution of forward (+) and backward (-) propagating intensities at pump (p) and signal (s) wavelengths in the FP cavity of a VCSRA are as follows:

$$
\begin{aligned}
dI_S^\pm / dz &= \pm g_R (I_P^+ + I_p^-) I_s^\pm \mp \alpha I_s^\pm \\
dI_P^\pm / dz &= \mp g_R \lambda_S / \lambda_P (I_S^+ + I_S^-) I_P^\pm \mp \alpha I_P^\pm
\end{aligned}
\tag{4.1}
$$

Given the top (T) and bottom (B) mirror reflectivities, the boundary conditions for Mode 1 are:

$$
\begin{aligned}
I_P^-(L) &= (1 - R_{TP}) I_{Pin} + R_{TP} I_P^+(L) \\
I_P^+(0) &= R_{BP} I_P^-(0) \\
I_S^+(0) &= R_{BS} I_S^-(0) \\
I_S^-(L) &= (1 - R_{TS}) I_{Sin} + R_{TS} I_S^+(L)
\end{aligned}
\tag{4.2}
$$

while the boundary conditions for Mode 2 are:

$$
\begin{aligned}
I_P^+(0) &= (1 - R_{BP}) I_{Pin} + R_{BP} I_P^-(0) \\
I_P^-(L) &= R_{TP} I_P^+(L) \\
I_S^+(0) &= R_{BS} I_S^-(0) \\
I_S^-(L) &= (1 - R_{TS}) I_{Sin} + R_{TS} I_S^+(L)
\end{aligned}
\tag{4.3}
$$

L is the length of the cavity. In order to achieve standing waves in the cavity at both pump and signal (Stokes) wavelengths, L has to be a multiple of both λ_S (3.39 µm) and λ_P (2.88 µm). Here we assume $L = 949$ µm $= 960\lambda_S = 1130\lambda_P$. We identified CaF$_2$ (refractive index $n_1 = 1.42$) and ZnSe (refractive index $n_2 = 2.44$) for top and bottom DBRs. Due to the large index contrast between CaF$_2$ and ZnSe, DBR design for Mode 2 is more difficult. This is because the counter-directionally propagating mode requires high reflectivity (>0.9) at λ_S (or λ_P) and much lower reflectivity at λ_P (or λ_S) for the top (or bottom) mirror, which is impossible to achieve when the bandwidth of the DBR is too large, as the frequency shift between the two waves is only 15.6 THz. Using materials with lower index contrast for DBR design is a possible solution. Here we circumvent the problem by choosing the co-directionally propagating mode (Mode 1).

We set R_{BS}=0.9, R_{BP}=0.9, R_{TP}=0.2, and R_{TS} as a variable. In Fig. 2-16 the signal gain is plotted versus R_{TS} at pump intensity of 400 kW/cm^2. R_{TS} should be kept below 50% in order to avoid operating too close to the lasing threshold. Table 2-1 summaries the DBR design for the top and bottom mirrors. The signal gain obtained is 4.5 dB.
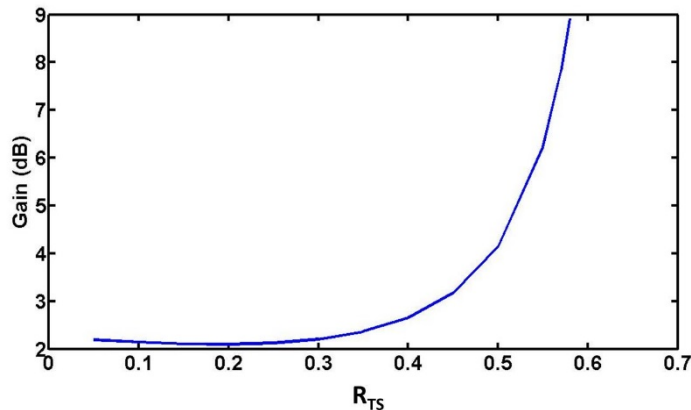
Figure 2-16: Signal gain versus RTS for pump intensity of 400 kW/cm^2 and for $R_{BS}=$ 0.9, $R_{BP} = 0.9$, $R_{TP} = 0.2$.

Table 2-1: DBR design for the top and bottom mirrors of a mid-IR VCSRA.

Mirror	Top	Bottom
Materials	ZnSe/CaF$_2$	CaF$_2$/ZnSe
Number of pairs	1.5	7
Layer thickness	$d_{CaF2} = 0.597\,\mu m$; $d_{ZnSe} = 0.347\,\mu m$	$d_{CaF2} = 0.597\,\mu m$; $d_{ZnSe} = 0.347\,\mu m$
Reflectivities	$R_{TS} = 0.454$; $R_{TP} = 0.476$	$R_{BP} = 0.917$; $R_{BS} = 0.993$

CHAPTER 3: NOISE FIGURE IN SILICON OPTICAL PARAMETRIC AMPLIFIERS

3.1   Background

There has been significant progress in the development of silicon-photonic-based optical parametric amplifiers and wavelength converters based on the Kerr effect [69]. However, similar to SRLs discussed in previous chapter, significant nonlinear loss mechanism of TPA-induced FCA caused by the high optical intensities required for nonlinear interactions, have limited the performance and efficiency of these nonlinear devices [10]. Several methods, similar to those applied to SRLs, have been proposed to mitigate this drawback. First, active carrier sweep-out using *p-i-n* junction diodes and short-pulse pumping can partially reduce FCA [21]; second, silicon photonics has been pursued in the mid-IR regime using optical pumps at wavelengths above the TPA threshold wavelength of 2.2 µm [10] (Recent developments in the emerging field of mid-IR silicon photonics were discussed in detail in Chapter 2); Third, amorphous silicon (a-Si) has shown promise for large parametric amplification and efficient wavelength conversion due to its large nonlinear figure of merit (FOM = $n_2/\beta_{TPA}\lambda$, where β_{TPA} is the TPA coefficient and n_2 is the nonlinear refractive index) at telecom wavelengths [70]. Nonlinear coefficient as large as 2000 $(W.m)^{-1}$ [71] and FOM of ~5, which is more than 7 times higher than that of the SOI waveguides [72] are reported. Material degradation due to pump exposure can limit the performance, although it has been claimed that optical stability has been greatly improved recently and no degradation of the nonlinear parameters has been observed at peak pump

intensity as high as 2 GW/cm^2 [72]. FWM gain of 26.5 dB [73] and conversion efficiency of 12 dB [74] have been demonstrated experimentally in hydrogenated a-Si nanowires.

One of the main concerns in the design of nonlinear photonic devices is the noise figure (NF), which impairs the device performance. Several studies on the noise characteristics of silicon Raman amplifiers [75, 76], SRLs [77, 78], and near-IR c-Si OPAs [79] have been reported. The signal-to-noise ratio (SNR) of mid-IR c-Si parametric wavelength converters has been studied in Ref. [80]. However, the noise originating from the pump lasers was excluded from the calculations and the waveguide was assumed to be lossless. This chapter aims at full characterization of the signal NF spectrum in both near-IR a-Si and mid-IR c-Si OPAs. Main noise sources, i.e., photon fluctuations due to gain and loss in the medium and pump transferred noise (PTN), are accounted for and numerically simulated.

Specifically, the following aspects of a-Si and mid-IR c-Si OPAs are studied here for the first time. First, a-Si has a broad band Raman spectrum centered at 480 cm^{-1} (~ 14.4 THz) [81]. The effect of the complex Raman nonlinearity on the process of FWM cannot be ignored in the analysis of gain and NF of a-Si OPAs. Second, unlike near-IR c-Si OPAs, in which the pump laser's RIN is not as effective as the ASE of the EDFA, mid-IR c-Si OPAs are usually pumped with optical parametric oscillators (OPOs) or high power pulsed lasers (e.g., Er:YAG lasers) instead of EDFA. Therefore, pump ASE noise does not exist but the RIN of the pump laser will be transferred to the signal and the final NF of the amplifier will be increased. Thus, the PTN must be analyzed using a different numerical model.

3.2   Noise Figure of Near-IR a-Si OPAs

Unlike c-Si whose Raman spectrum peaks at a frequency shift of 15.6 THz and has a full-width at half-maximum (FWHM) of only 105 GHz [41], a-Si is less orderly in its atomic arrangement and hence has a broad Raman band centered at 14.4 THz [81]. When high pump power and large gain bandwidth are considered, the effect of Raman nonlinearity on the parametric amplification process becomes non-negligible. Both the gain and NF spectra will be modified due to the complex Raman susceptibility. Raman-induced quantum-limited NF and asymmetric pump noise transfer in fiber OPAs have been analytically studied [82]. However, in a-Si OPAs, where nonlinear losses (TPA and FCA) are present, achieving accurate analytical solutions becomes difficult, if not impossible. In this paper, the impact of Raman nonlinear susceptibility on the performance of near-IR a-Si OPAs is investigated for the first time.

In previous studies of c-Si OPAs, the conventional nonlinear parameter $\gamma_0 = 2\pi n_2/A_{eff}\lambda_p$ is always assumed to be constant over the telecommunication band (where λ_p is the pump wavelength and A_{eff} is the effective waveguide area). Here, a frequency dependent nonlinear parameter is defined:

$$\gamma(\Omega) = 2\pi n_2(\Omega)/\lambda A_{eff} \qquad (3.1)$$

where $n_2(\Omega) = 3\chi^{(3)}(\Omega)/(4\varepsilon_0 n_0^2 c)$ is the frequency dependent nonlinear refractive index (ε_0 is the permittivity of free space and c is the speed of light). The third-order susceptibility $\chi^{(3)}(\Omega)$ is composed of the nonresonant (or electronic) susceptibility $\chi_{NR}^{(3)}$, which is a delta function in the time domain and a constant in the frequency domain, and the resonant (or Raman) susceptibility

$\chi_R^{(3)}(\Omega)$, which is a time-delayed response and varies over the bandwidth of interest [82].

The real part of the Kerr nonlinearity in a-Si:H waveguides can be found in published measurements [71]. It should be noted that the γ reported in this reference is the sum of the nonresonant nonlinearity and the resonant nonlinearity at zero frequency shift. The broad band Raman gain profile $g_R(\Omega)$ of a-Si is previously characterized too [81]. Its maximum value is estimated to be ~4.735 cm/GW from Fig. 1 of Ref. [81], given the Raman gain coefficient of c-Si at wavelength of 1550 nm (20 cm/GW). The imaginary part of $\gamma(\Omega)$ equals to $g_R(\Omega)/2$ if the pump and the signal waves are co-propagating and co-polarized [82]. The real part of $\gamma(\Omega)$ is then calculated using Kramers-Kronig transformation for the parallel Raman susceptibility [83]:

$$\text{Re}[\chi_R^{(3)}(\Omega)] = \frac{1}{\pi} P \int_{-\infty}^{\infty} d\Omega' \frac{\text{Im}[\chi_R^{(3)}(\Omega')]}{\Omega' - \Omega} \tag{3.2}$$

where P denotes the principle part of the integral and is estimated to be 1.0203 in the case of a-Si. Figure 3-1 shows the real and imaginary part of $\gamma(\Omega)$ of the waveguide studied later, including the Raman contribution.

Assuming the pump intensity is much higher than the signal intensity, the coupled-mode equations that describe the evolution of the pump, signal and idler amplitudes along the waveguide including the effect of the Raman susceptibility are as follows [84]:

$$dA_p / dz = -1/2\left(\alpha + \alpha_p^{FCA}(z)\right)A_p$$
$$+ i\left(\gamma_0 + i\beta_{TPA}/(2A_{eff})\right)|A_p|^2 A_p \tag{3.3a}$$

$$dA_s / dz = -1/2\left(\alpha + \alpha_s^{FCA}(z)\right)A_s$$
$$+ i\left(\gamma_0 + \gamma(-\Omega) + i\beta_{TPA}/A_{eff}\right)|A_p|^2 A_s \tag{3.3b}$$
$$+ i\gamma(-\Omega)A_p^2 A_i^* \exp(-i\Delta kz)$$

$$dA_i / dz = -1/2\left(\alpha + \alpha_i^{FCA}(z)\right)A_i$$
$$+ i\left(\gamma_0 + \gamma(\Omega) + i\beta_{TPA}/A_{eff}\right)\left|A_p\right|^2 A_i \qquad (3.3c)$$
$$+ i\gamma(\Omega)A_p^2 A_s^* \exp(-i\Delta kz)$$

Here, α is the linear propagation loss of the waveguide, β_{TPA} is the TPA coefficient, A_j (j

= p,s,i) is the electrical field amplitude of the three waves in unit of $W^{1/2}$,

$\alpha_j^{FCA}(z) = 1.45 \times 10^{-17}(\lambda_j/1.55)^2 \tau_{eff}\beta_{TPA}\left|A_p\right|^4/(2E_p A_{eff}^2)$, where τ_{eff} is the effective carrier lifetime,

E_p is the photon energy at pump wavelength. $\Omega = \omega_i - \omega_p = \omega_p - \omega_s$ is the frequency deviation

from the pump wavelength. $\Delta k = k_s + k_i - 2k_p = \beta_2\Omega^2$ is the phase mismatch between the three

waves, where k_j is the propagation constant at frequency ω_j and β_2 is the group velocity

dispersion coefficient.
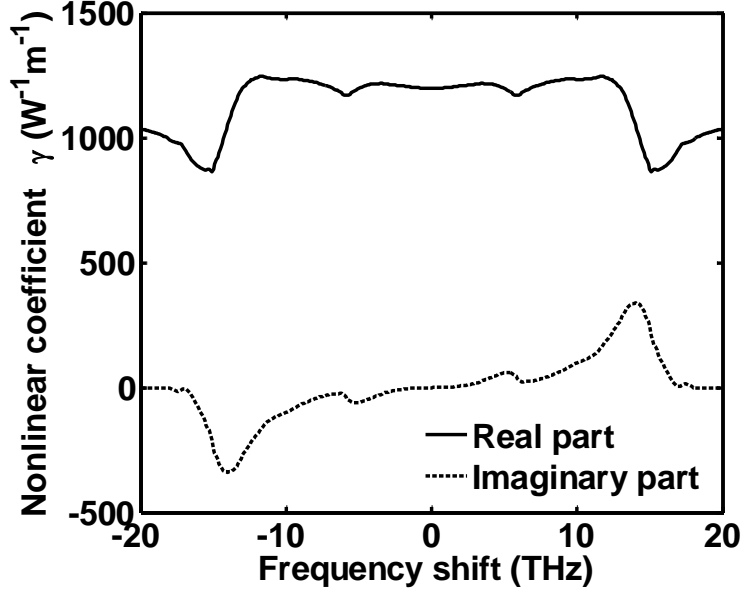
Figure 3-1: Real and imaginary part of the nonlinear coefficient $\gamma(\Omega)$ including the Raman contribution. The effective area of the waveguide is assumed to be 0.07 μm^2 [85].

49

To estimate the total NF of silicon OPAs, the noise induced by photon fluctuations in the material and the noise induced by the noise of the pump sources are calculated separately. In the presence of nonlinear TPA and FCA losses, the above coupled-mode equations do not have analytical solutions as in optical fibers. Therefore, the model in Ref. [82] cannot be applied to a-Si OPAs. Here, the noise model in [75] and [79] for linear optical amplifiers is used.

Ideally, when loss or gain is present in a waveguide, Langevin noise sources must be added to the propagation equations (e.g., Eqs. 3.3) in order to maintain the equilibrium value of the field amplitude along the waveguide length. This semi-classical approach has been pursued in Raman fiber lasers, where there exists no nonlinear loss and analytical solutions are possible [86]. However, in the present case, the resulting equations do not lend themselves to analytical solutions, since nonlinear losses are present and hence the noise terms do not have explicit z-dependent expressions. Instead, a fully quantum-mechanical noise model is used here. In this approach Eqs. 3.3 are solved under steady state condition without including the noise term and then the approach described in the following is used to include the noise terms in the propagation equation of the quantum-mechanic annihilation operator [75,79].

In a single-mode silicon OPA, the signal wave propagating along the waveguide experiences both parametric gain $g(z)$ and losses determined by $\gamma'(z)$:

$$\frac{d\hat{a}_s}{dz} = \left[\frac{g(z)}{2} - \frac{\gamma'(z)}{2} \right] \hat{a}_s \tag{3.4}$$

where $\hat{a}_s$ is the photon annihilation operator of the signal field. The operator is normalized according to the commutation relation $[\hat{a}_s, \hat{a}_s^+] = 1$ where $\hat{a}_s^+$ is the photon creation operator of the signal field. The gain and loss parameters $g(z)$ and $\gamma'(z)$ can be numerically solved from the

50

coupled mode equations (3.3a)-(3.3c).

The Langevin noise sources for gain and loss are derived on the principle of commutator conservation, i.e., $d[\hat{a}_s, \hat{a}_s^+]/dz = 0$, and are given by the operators $\sqrt{g(z)}\hat{N}_g^+$ and $\sqrt{\gamma'(z)}\hat{N}_l$, respectively [75]. The commutators of the noise source operators are delta functions. Eq. (3.4) is now rewritten taking into account the noise sources:

$$\frac{d\hat{a}_s}{dz} = \left[\frac{g(z)}{2} - \frac{\gamma'(z)}{2}\right]\hat{a}_s + \sqrt{g(z)}\hat{N}_g^+ + \sqrt{\gamma'(z)}\hat{N}_l \tag{3.5}$$

The analytical solution of Eq. (3.5) is given by:

$$\hat{a}_s(z) = \exp\left(\left(\frac{1}{2}\right)\int_0^z [g(z) - \gamma'(z)]dz\right)\hat{a}_s(0)$$
$$+ \int_0^z dz \exp\left(\left(\frac{1}{2}\right)\int_z^{z'} [g(z') - \gamma'(z')]dz'\right) \times \left(\sqrt{g(z)}\hat{N}_g^+(z) + \sqrt{\gamma'(z)}\hat{N}_l(z)\right) \tag{3.6}$$

The analysis of noise in a-Si OPAs is more complicated than that of c-Si OPAs due to the frequency dependent nonlinear coefficient. Eq. (3.3a)-(3.3c) are first solved numerically. The numerical solutions, i.e., the distribution of the three waves along the a-Si waveguide (z direction) are then used to calculate the gain and loss parameters $g(z)$ and $\gamma'(z)$. The mean output photon number N_o is evaluated from the first term on the right side of Eq. (3.6):

$$N_o = \exp\left(\left(\frac{1}{2}\right)\int_0^z [g(z) - \gamma'(z)]dz\right) \tag{3.7}$$

and the photon number fluctuations induced by gain and loss in the FWM process are given by:

$$N_g = \int_0^L g(z)\exp\left(\int_z^L [g(z') - \gamma'(z')]dz'\right)dz \tag{3.8a}$$

$$N_i = \int_0^L \gamma'(z)\exp\left(\int_z^L [g(z') - \gamma'(z')]dz'\right)dz \tag{3.8b}$$

Assuming the input photon number at the signal wavelength is large enough, the NF induced by photon fluctuations can be calculated as [75,79]:

$$NF_{pf} = (N_o + N_g + N_l)/N_o. \tag{3.9}$$

At near-IR, an EDFA is usually used as the pump source. The ASE noise of the EDFA is transferred to the signal during the parametric amplification process. The RIN of the pump laser (before getting amplified by the EDFA) can also impact the performance of the a-Si OPA. However, the availability of low noise lasers at telecom wavelength with RIN below -160 dB/Hz makes the contribution of pump-to-signal RIN transfer negligible. The case for mid-IR OPAs is completely different, as will be discussed in the Section 3.3. To calculate the signal variation due to the power variation of the input pump ΔP_{pin}, the output signal $P_{sout} = |A_s(z=L)|^2$ is assumed to be linearly dependent on the mean input pump power $P_{pin} = |A_p(z=0)|^2$, if ΔP_{pin} is small. Consequently, the quadratic fluctuation terms can be neglected:

$$P_{sout}(P_{pin}) = G(P_{pin}) \cdot P_s(z=0) + B \cdot \Delta P_{pin} \tag{3.10}$$

where $G(P_{pin})$ is the signal gain as a function of input pump power, and B is the slope of P_{sout} at P_{pin}. The analytical expression of B can be found in Ref. [87] for lossless waveguides. However, B must be calculated numerically in a-Si waveguides due to the presence of linear and nonlinear losses. If the quantum noise of the pump source as well as the ASE-ASE beating terms are neglected and only the pump-ASE beating noise is considered, the linear NF increase (after detection) contributed by the noisy pump is given by [87]:

$$\Delta NF_{pump} = \frac{2B^2 P_{pin} n_{sp}(G_A - 1)}{G(P_{pin})^2 P_s(z=0)} \tag{3.11}$$

where n_{sp} is the population inversion factor of the EDFA and G_A is the gain of the EDFA. It is

noticed that B is proportional to P_s ($z = 0$), therefore ΔNF_{pump} is linearly dependent on the input signal power, while ΔNF_{pf} does not have signal dependence. The total NF of a-Si OPAs is finally obtained by

$$NF = NF_{pf} + \Delta NF_{pump} \qquad (3.12)$$

Table 3-1 summarizes the linear and nonlinear optical properties of near-IR c-Si, near-IR a-Si and mid-IR c-Si waveguides employed in this work. It is noted that, unlike c-Si, the nonlinear optical properties of a-Si:H such as β_{TPA} and $\gamma(\Omega)$ strongly depend on the fabrication process, i.e., its composition (hydrogen content) or atomic arrangement. γ_0 as high as 2000 $W^{-1}m^{-1}$ [72] and β_{TPA} as low as 0.08 cm/GW [88] have been reported for a-Si waveguides. However, unfortunately they cannot be achieved simultaneously. Nonlinear parameters $\gamma_0 = 1200$ $W^{-1}m^{-1}$ and $\beta_{TPA} = 0.25$ cm/GW [71] are used in the following simulations as they provide the highest nonlinear FOM (~ 5) reported to date. The studied waveguides are 500 nm wide and 220 nm high and have an effective area $A_{eff} = 0.07$ μm^2. The length of the devices is 2 cm. The group velocity dispersion (GVD) of the waveguides is set to be 200 ps.km^{-1}.nm^{-1}, which leads to a large gain bandwidth of > 200 μm (Fig. 3) and thus more apparent Raman-induced noise. Although the linear loss of a-Si waveguides are higher than c-Si waveguides, the propagation losses as low as 3.2 ± 0.2 dB/cm for the TE mode and 2.3 ± 0.1 dB/cm for the TM mode have been reported for submicron (200 nm $\times$ 500 nm) a-Si wire waveguides [89]. Free-carrier lifetimes in the picosecond range have been measured [90]. Here, the devices are assumed to be pumped with a peak intensity of 500 MW/cm^2 at wavelength of 1550 nm. In the simulation of PTN contribution to the NF, $n_{sp} = 1.5$ and $G_A = 50$ are used as typical near-IR lasers have 1-10 mW of output power before amplification. The input signal power is assumed to be 10 μW.

Table 3-1: Summary of optical properties of three different types of silicon waveguides.

	c-Si (near-IR)	a-Si (near-IR)	c-Si (mid-IR)
n_2 (m^2/W)	5.5×10^{-18}	2.1×10^{-17}	3.67×10^{-18}
α (dB/cm)	< 0.2	> 2	~ 1
β_{TPA} (cm/GW)	0.7	0.25	--
τ_{eff}	$\sim$ ns	$\sim$ ps	--
FOM	0.3-0.5	~ 5	--
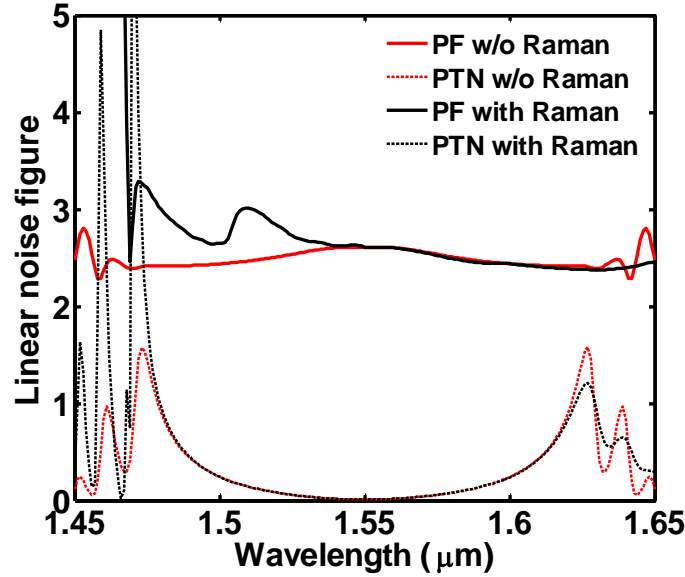
Figure 3-2: Linear NF spectra of near-IR a-Si OPA pumped at wavelength of 1550 nm with a peak intensity of 500 MW/cm^2. The noise sources contribute to the total NF, i.e., photon fluctuations and PTN are modeled separately. For the NF spectra calculation excluding the Raman effect (dashed lines), Im$\{\gamma(\Omega)\} = 0$. The linear loss of the waveguide is 2 dB/cm [85].

Figure 3-2 shows the linear NF spectrum of a-Si OPA pumped at 1550 nm. The NF spectrum without Raman effect, i.e., $\gamma(\Omega) = \gamma_0$ or Im$\{\gamma(\Omega)\} = 0$, is also plotted for comparison. As illustrated, the NF contribution from gain and loss fluctuations is greater than the PTN

contribution, so that it can be treated as the dominant noise source in a-Si OPAs, when the input signal power is small. It is shown that when the Raman effect is taken into account, the NF spectra for both gain and loss fluctuations and PTN become asymmetric due to the real and imaginary part of the Raman susceptibility. For signal wavelengths that are longer than the pump wavelength (Stokes side or negative frequency shift), the NF spectrum are slightly modified when Raman-induced noise is considered. For signal wavelengths shorter than the pump wavelength (anti-Stokes side or positive frequency shift), the NF is evidently increased compared to the NF without Raman, especially at the gain edge (Fig. 3). Similar results have been obtained in lossless fiber OPAs [82].   In this paper, for the first time, linear and nonlinear losses, as well as the complex third order susceptibility are all considered at the same time.
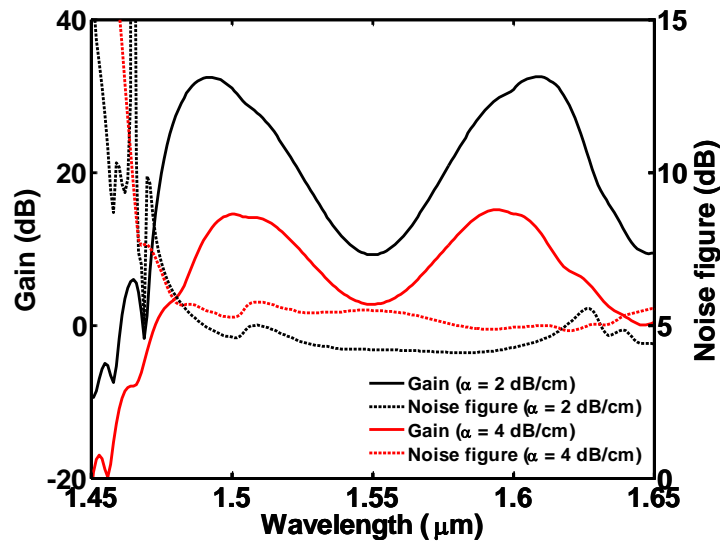
Figure 3-3: Gain and total NF spectra of near-IR a-Si OPAs with linear propagation losses of 2 dB/cm and 4 dB/cm. Raman susceptibility is included [85].

In Fig. 3-3, the gain and total NF spectra are plotted in logarithmic scale. For linear loss as low as 2 dB/cm, wideband optical gain (maximum 30 dB) is obtained with a NF of ~ 5 dB at

wavelengths from 1.48 µm to 1.65 µm. The asymmetry of the gain spectrum is obvious due to the Raman gain on the Stokes side and Raman loss on the anti-Stokes side. The NF increases sharply to above 20 dB at the gain edge on the anti-Stokes side. Although the gain at wavelengths ~ 1.47 µm is still high (10 dB or more), the overall performance of the OPA is poor because of the high NF. Therefore, operation of the a-Si OPA is limited by the NF for signal frequencies larger than the pump frequency. Linear loss of 4 dB/cm is also considered because low linear loss and high nonlinear FOM may not be achieved simultaneously. It is clear that for OPAs with higher propagation loss, the gain is lower and the NF is slightly higher over the gain bandwidth.

3.3   Noise Figure of Mid-IR c-Si OPAs

TPA and FCA vanish in the mid-IR regime in c-Si. Although 3PA and associated free-carrier effects are considerable for pump intensities of a few GW/cm^2 in the wavelength range of 2300 nm–3300 nm [25,91], in our case, the pump laser wavelength is assumed to be 3.4 µm. Since this pump photon energy is below one third of silicon's indirect band-gap, 3PA-induced nonlinear losses are negligible for small signal intensities. Also, although the Kerr effect is weaker in the mid-IR, and the larger λ further reduces the conventional nonlinear parameter γ, FWM on SOI waveguides perform better at ~2.2 µm when compared to ~ 1.5 µm due to lower nonlinear losses [19]. $n_2 = 1 \times 10^{-5}$ cm^2/GW was measured at 2.35 µm [55] and theoretical calculations were published that predict different n_2 values (3.67 to 3.26$\times 10^{-5}$ cm^2/GW for λ varying from 3.39 to 4.26 µm [60]). The latter are the values used in this work.

Noise sources in mid-IR c-Si OPAs are similar to those in a-Si OPAs. Modeling of photon fluctuations in mid-IR c-Si OPAs is much easier because β_{TPA}, $\alpha_j^{FCA}(z)$, and $\gamma(\pm\Omega)$ in Eqs. (3.3a)-(3.3c) can be simply set to be zero. The nonlinear coefficient γ is assumed to be real and constant over the frequency range of interest because the Raman gain spectrum of c-Si has a sharp peak at a frequency shift of 15.6 THz and the common bandwidth of c-Si OPAs is only a few THz. However, the PTN of mid-IR c-Si OPAs should be modeled differently because mid-IR optical amplifiers are not commercially available. Mid-IR high power sources such as pulsed lasers and OPOs have low beam quality and high intensity fluctuations. Therefore, the RIN transferred from pump to signal should be analyzed instead of the ASE noise of the pump.

The noise component at angular frequency ω in the pump noise spectrum is considered. A sinusoidal noise term is introduced on the pump, signal and idler amplitudes:

$$A_j(z,t) = \overline{A}_j(z) + \Delta A_j(z,t) = \overline{A}_j(z)[1 + \delta_j(z)\exp(i\omega t)] \tag{3.13}$$

where $\overline{A}_j(z)$ ($j = p,s,i$) are time-independent average intensities, $\delta_j(z)$ are time-independent complex values that satisfy $|\delta_j(z)| \ll 1$. The different values of pump, signal and idler group velocities, v_p, v_s and v_i should be accounted for, especially for high modulation frequencies (> 1 GHz). The coupled-mode equations including group velocities and neglecting nonlinear losses as well as Raman contribution are as follows:

$$\partial A_p / \partial z + 1/v_p \cdot \partial A_p / \partial t = -(1/2)\alpha A_p + i\gamma |A_p|^2 A_p \tag{3.14a}$$

$$\begin{aligned} \partial A_s / \partial z + 1/v_s \cdot \partial A_s / \partial t = {} & -(1/2)\alpha A_s + 2i\gamma |A_p|^2 A_s \\ & + i\gamma A_i^* A_p^2 \exp(-i\Delta k z) \end{aligned} \tag{3.14b}$$

57

$$\partial A_i / \partial z + 1/v_i \cdot \partial A_i / \partial t = -(1/2)\alpha A_i + 2i\gamma \left| A_p \right|^2 A_i$$
$$+ i\gamma A_s^* A_p^2 \exp(-i\Delta kz) \tag{3.14c}$$

Substituting Eq. (3.13) into Eq. (3.14) and neglecting higher order fluctuation terms, the

propagation equations for the pump, signal and idler amplitude modulations are obtained:

$$\partial \Delta A_p / \partial z = -i\omega \Delta A_p / v_p - (1/2)\alpha \Delta A_p$$
$$+ i\gamma (2\left| \overline{A}_p \right|^2 \Delta A_p + \overline{A}_p^2 \Delta A_p^*) \tag{3.15a}$$

$$\partial \Delta A_s / \partial z = -i\omega \Delta A_s / v_s - (1/2)\alpha \Delta A_s$$
$$+ 2i\gamma (\left| \overline{A}_p \right|^2 \Delta A_s + \overline{A}_p \overline{A}_s \Delta A_p^* + \overline{A}_p^* \overline{A}_s \Delta A_p)$$
$$+ i\gamma (\overline{A}_p^2 \Delta A_i^* + 2\overline{A}_p \overline{A}_i^* \Delta A_p) \exp(-i\Delta kz) \tag{3.11b}$$

$$\partial \Delta A_i / \partial z = -i\omega \Delta A_i / v_i - (1/2)\alpha \Delta A_i$$
$$+ 2i\gamma (\left| \overline{A}_p \right|^2 \Delta A_i + \overline{A}_p \overline{A}_i \Delta A_p^* + \overline{A}_p^* \overline{A}_i \Delta A_p)$$
$$+ i\gamma (\overline{A}_p^2 \Delta A_s^* + 2\overline{A}_p \overline{A}_s^* \Delta A_p) \exp(-i\Delta kz) \tag{3.11c}$$

The RIN transfer is then calculated as the ratio of the signal RIN at the output of the OPA

and the pump RIN at the input of the OPA:

$$T_{RIN} = \left(\frac{\Delta P_s(L)}{\overline{P}_s(L)} \right)^2 \Big/ \left(\frac{\Delta P_p(0)}{\overline{P}_p(0)} \right)^2$$
$$= \frac{\left(\overline{A}_s^*(L)\Delta A_s(L) + \overline{A}_s(L)\Delta A_s^*(L) \right)^2 \left| \overline{A}_p(0) \right|^2}{\left(\overline{A}_p^*(0)\Delta A_p(0) + \overline{A}_p(0)\Delta A_p^*(0) \right)^2 \left| \overline{A}_s(L) \right|^2} \tag{3.12}$$

The linear NF increase due to pump-to-signal RIN transfer is given by [70]:

$$\Delta NF_{pump} = RIN_{pump} T_{RIN} \overline{P}_s(0) \lambda_s / 2hc \tag{3.13}$$

where h is the Planck's constant. Similar to near-IR a-Si OPAs, the PTN contribution to the total

NF is also linearly dependent on the input signal power.

In order to satisfy the phase matching condition required by OPAs, an SOS waveguide is

designed by dispersion engineering to achieve wideband anomalous dispersion ($D > 0$). The SOS

waveguide is 1.5 µm wide and 0.5 µm high and exhibits D of 250 - 450 ps.km^{-1}.nm^{-1} in the wavelength range of 2.9 - 3.9 µm. The pump wavelength is fixed at 3.4 µm. Due to the absence of nonlinear losses, increasing the pump power will always increase the gain of the OPA. The limiting factor, therefore, becomes the damaging threshold of silicon instead of the pump depletion due to FCA. Optical gain of ~30 dB is easily obtained at a peak pump intensity of 3 GW/cm^2 assuming the waveguide linear loss is 1 dB/cm and the length of the waveguide is 3 cm (Fig. 3-6(a)).
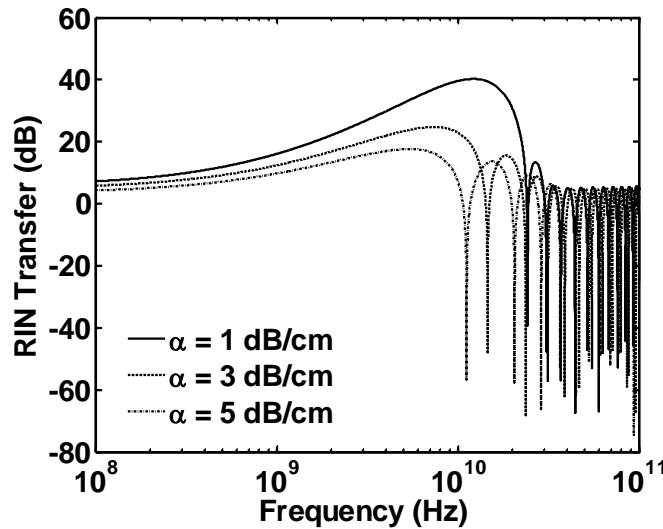
Figure 3-4: Pump-to-signal RIN transfer spectra for mid-IR c-Si OPAs with linear propagation losses of 1, 3 and 5 dB/cm. The OPA is pumped at a wavelength of 3.4 µm with a peak intensity of 3 GW/cm^2 [85].

Figure 3-4 presents the modulation frequency dependent pump-to-signal RIN transfer for waveguide losses of 1, 3 and 5 dB/cm at the wavelength of 3.338 µm, where the gain peaks (Fig. 3-6(a)). RIN transfer remains constant at low frequencies, and then starts to oscillate at > 10 GHz. The observed strong oscillations at higher frequencies suggest that laser sources with RIN

spectra no wider than 10 GHz are required for pumping mid-IR c-Si OPAs. The RIN values of the signal at lower frequencies could be about 5 ~ 10 dB higher than that of the pump for waveguide with linear loss of 5 dB/cm, and the situation is even worse for waveguides with lower propagation losses (larger parametric gain).

Figure 3-5(a) and (b) present the linear NF spectrum of mid-IR c-Si OPAs for propagation losses of 1 dB/cm and 3 dB/cm, respectively. Noise sources including gain and loss fluctuations and low-frequency pump-to-signal RIN transfer are both taken into account. No data on the RIN of mid-IR lasers is currently available. The pump RIN used in the following simulations is -140 dB/Hz, assuming mid-IR OPOs or pulsed lasers have similar noise performance as typical near-IR pump lasers, whose RIN is 20 dB worse than near-IR lasers used in optical communications [76]. It is evident that for mid-IR c-Si OPA with linear loss of 1 dB/cm (Fig. 3-5(a)), the noise induced by photon fluctuations is just slightly above the well-known 3 dB NF limit for an ideal OPA, while the noise transferred from the pump source is much higher, which leads to a total NF of well above 10 dB at the gain edge (Fig. 3-6(a)). In OPAs with linear loss of 3 dB/cm (Fig. 3-5(b)), the pump-to-signal RIN transfer dominates over the noise induced by gain and loss fluctuations.
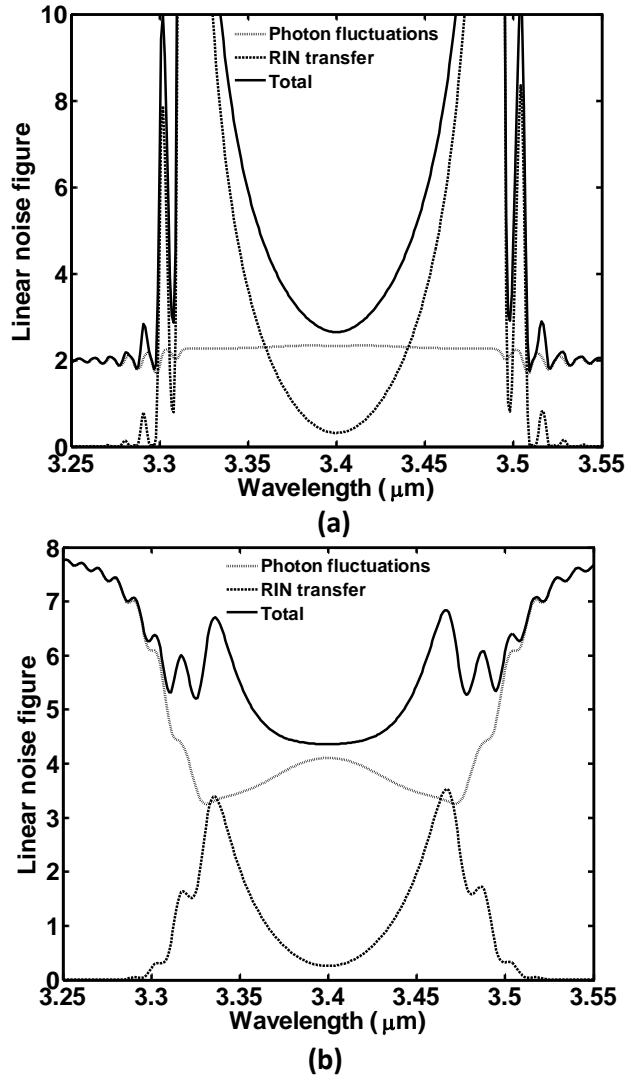
Figure 3-5: Linear NF spectra of mid-IR c-Si OPAs pumped at wavelength of 3.4 µm with a peak intensity of 3 GW/cm^2. The noise sources contribute to the total NF, i.e., photon fluctuations and RIN transfer are modeled separately: (a) α = 1 dB/cm and (b) α = 3 dB/cm [85].

In Fig. 3-6(a), the gain and NF spectra of the mid-IR c-Si OPAs are plotted in logarithmic scale. Unlike near-IR a-Si OPAs, in which higher amplification always leads to lower NF, in mid-IR c-Si OPAs, the gain and NF are both higher for lower propagation loss at large frequency shift (around the maximum gain). This is because the RIN transfer increases with increasing gain

61

as illustrated in Fig. 3-4. This limits the performance of low-loss mid-IR c-Si OPAs for large bandwidth operation. In Fig. 3.6(b), the maximum gain and NF of maximum gain are plotted versus peak pump intensity. It is shown that there is no gain saturation as in near-IR c-Si OPAs [79] because of the absence of TPA and FCA. For linear noise of 1 dB/cm, the NF of maximum gain keeps increasing when the pump intensity increases due to the high pump-to-signal RIN transfer which is the dominant noise source. For linear loss of 3 dB/cm, the noise figure of maximum gain is almost constant (< 10 dB), for pump intensities ranging from a few hundred MW/cm^2 to 5 GW/cm^2. This originates from the mutual influence of photon fluctuations (which decreases with increasing pump intensity) and pump-to-signal RIN transfer (which increases with increasing pump intensity).
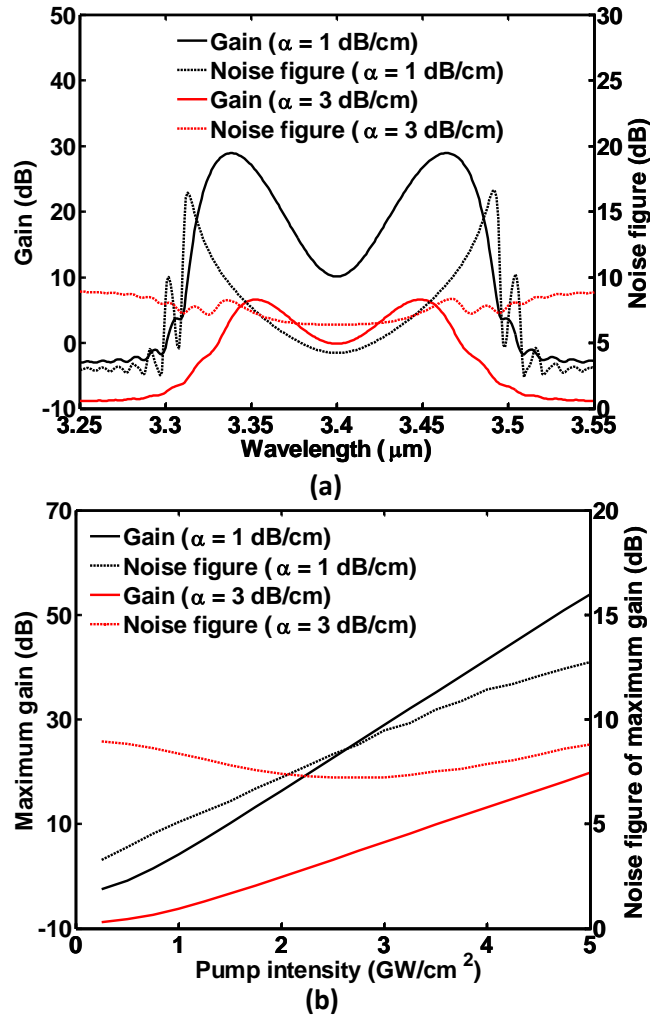
Figure 3-6: (a) Gain and total NF spectra of mid-IR c-Si OPAs with linear propagation losses of 1 dB/cm and 3 dB/cm; and (b) NF evolution at the maximum gain [85].

The gain and NF spectra of near-IR a-Si OPAs (Fig. 3-3) and mid-IR c-Si OPAs (Fig. 3-6(a)) are quite different from those of near-IR c-Si OPAs previously studied in Ref. [79]. Near-IR c-Si OPAs pumped with pulsed lasers have a maximum gain of ~ 10 dB, even when the carrier sweep-out technique is applied. Further increasing the pump power will result in lower gain and higher NF at the same time due to the intensity-dependent nonlinear losses. In contrast, in near-IR a-Si OPAs and mid-IR c-Si OPAs, > 30 dB gain can be easily achieved and no

63

saturation of the gain is observed with pump intensity up to a few GW/cm^2. Slight asymmetry appears in the gain spectrum of a-Si OPAs due to the Raman-effect-induced gain and loss. The NF spectrum of near-IR c-Si OPAs (Fig. 3 in [79]) is more or less symmetric with respect to the pump wavelength (slight asymmetry comes from the wavelength dependence of FCA). The NF is around 10 dB for small frequency detuning and drops to below 6 dB at the gain edge. However, in near-IR a-Si OPAs, the NF is only about 5 dB on the Stokes side due to the low nonlinear losses, but increases sharply at the gain edge on the anti-Stokes side. The NF spectrum of mid-IR c-Si OPA is strictly symmetric with respect to the pump wavelength. However, unlike near-IR c-Si OPAs in which the NF contribution from gain and loss fluctuations is the dominant noise source, the NF of mid-IR c-Si OPAs might be dominated by the pump-to-signal RIN transfer. Large gain and small NF cannot be achieved at the same time because the RIN transfer increases with increasing gain.

CHAPTER 4: HYBRID WAVEGUIDE TECHNOLOGY ON SILICON

4.1   Background

The primary target for silicon photonics has been low-cost optical telecommunication components and integrated circuits, e.g., optical transceiver for Ethernet and data center applications. Meanwhile, silicon photonics has been also pursued as a platform for integrated nonlinear optics. Silicon is a centrosymmetric crystal and hence the second-order optical susceptibility ($\chi^{(2)}$) is virtually nonexistent in the material. Alternatively, the third-order nonlinearity ($\chi^{(3)}$–based effects) has been exploited. However, the performance of nonlinear devices operating based on $\chi^{(3)}$ effects cannot in principle compete with devices based on $\chi^{(2)}$ effects for most applications.

In this chapter, in collaboration with my colleagues, a novel hybrid platform [92] is demonstrated that not only enjoys the mentioned advantages of silicon photonics (compatible with CMOS process of microelectronics, low-loss and tightly confined waveguides), but also uses a second-order nonlinear material in the waveguide core region instead of silicon. The choice of the material is $LiNbO_3$, which has one of the highest $\chi^{(2)}$ values among nonlinear optical materials. The single-crystalline $LiNbO_3$ also has large electrooptic (EO) coefficients (r_{33} = 31 pm/V and r_{13} = 8 pm/V), wide transparency wavelength window (0.4 to 5 µm), and large intrinsic bandwidth [93,94]. Indeed, standard $LiNbO_3$ waveguides are widely regarded as the best vehicle for electrooptic modulation in the photonic industry with impressively high modulation bandwidths (up to 100 GHz [13]). $LiNbO_3$ modulators definitely offer higher

65

performance (in terms of modulation bandwidth, modulation depth and insertion loss) compared to silicon optical modulators [1]. The challenge for this hybrid approach is how to make reliable LiNbO$_3$-on-Si wafers and low-loss submicron ridge/channel waveguides on them.

LiNbO$_3$ waveguides are traditionally formed by diffusion of titanium, the process of annealed proton exchange or implantation of dopants (e.g., oxygen ions) in bulk wafers [95]. Any of these processes can only slightly alter the refractive index of the material, i.e., the index contrast of the obtained stripe waveguides is rather small (0.1 to 0.2) and hence the guided modes are weakly confined. In EO modulators, this shortcoming leads to large device cross-sections (widths of several microns) and hence large half-voltage length-product, V_π.L, of 10 to 20 V.cm depending on modulation frequency and characteristic impedance [13,96]. Large cross-section waveguides also implies the need for high-power sources to achieve high optical density for the onset of optically-induced $\chi^{(2)}$ nonlinearity. Furthermore, weakly-confined waveguides means that their bending loss becomes significantly high for small radii.

Several years of efforts in developing dry or wet etching recipes for LiNbO$_3$ have not been successful in achieving submicron waveguides with smooth and vertical sidewalls. We envision an alternative approach that circumvents directly etching the hard dielectric material and instead forms the ridge on another index-matched material. Oxides of refractory metals, such as tantalum, niobium and titanium, have refractive indices close to that of LiNbO$_3$ (2.1 to 2.2) and are transparent over a very large range of optical wavelengths. Figure 4-1 summarizes the minimum achievable bending radius and waveguide core size of different waveguide technologies including our novel LiNbO$_3$-on-silicon platform. It is obvious that using this

technology, the waveguide dimensions and bending radius of LiNbO$_3$ devices can be reduced by one to two orders of magnitude compared with traditional LiNbO$_3$ waveguide technologies.
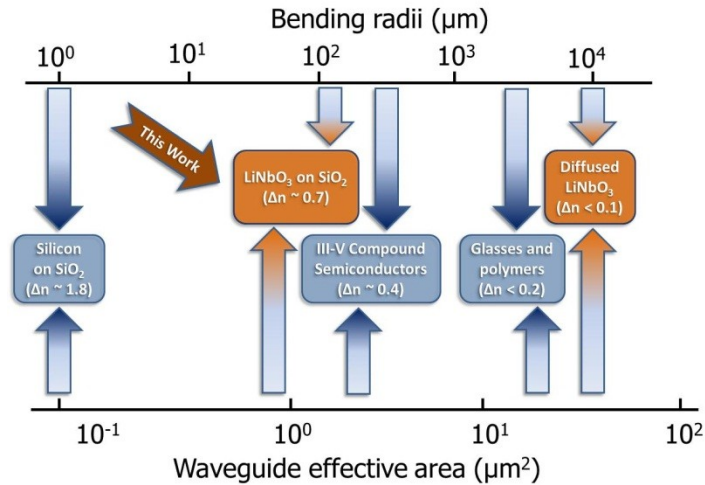
Figure 4-1: Typical ranges of effective areas and minimum radii for negligible ($<$ ~ 0.1 dB) bending loss at 90° bends are shown for different waveguides technologies. Δn denotes the rough refractive index contrast between core and cladding of the waveguides [92].

4.2 Ta$_2$O$_5$-on-Si Integrated Photonics

It has been mentioned in Section 4.1 that our novel LiNbO$_3$-on-silicon platform is based on etchless ridge formation technology using index-matched materials. In this work, the employed refractory metal is tantalum (Ta), whose oxide (Ta$_2$O$_5$) has a refractive index very close to that of LiNbO$_3$. Before demonstration of LiNbO$_3$ devices and in collaboration with my colleagues, Ta$_2$O$_5$-on-silicon waveguides and microring resonators were demonstrated first [97].

Previously, Ta$_2$O$_5$ waveguides have been demonstrated using standard lithography and RIE [98,99]. However, the propagation loss of the fabricated waveguides is high. Here my

colleagues and I developed a novel method based on selective oxidation of refractory metals (SORM) [97]. Instead of paying a lot of efforts in developing dry etching recipes for Ta_2O_5 to achieve submicron waveguides with smooth sidewalls, in our approach, the ridge waveguide is formed without the need of etching Ta_2O_5.

Figure 4-2 shows the fabrication process of Ta_2O_5 waveguides. First, the refractory metal (Ta) is deposited using a sputtering tool on a silicon substrate with a SiO_2 buffer layer (grown by thermal oxidation) on top. Next, 400-nm-thick SiO_2 is deposited on the tantalum surface by plasma-enhanced chemical vapor deposition (PECVD) as a mask layer. The SiO_2 layer is then patterned by electron-beam (e-beam) lithography to open a narrow submicron slot in the mask. The sample is then placed in a furnace with oxygen flow at high temperature (520°C) to selectively convert Ta into Ta_2O_5 in the exposed regions of the SiO_2 mask. A volume expansion of ~2 during oxidation must be considered during the mask design. In the subsequent steps, the SiO_2 layer is removed and the remaining Ta layer is etched away and a channel waveguide is formed. It is noted that since Ta can be etched highly selectively compared to Ta_2O_5, the tantalum etching step does not introduce any roughness in the waveguide layer. Finally, 1.5-µm-thick SiO_2 is deposited on top of the waveguides using PECVD as a cladding layer. Ridge waveguide and ridge and channel ring resonators were also fabricated. The gap with of the ring resonators is controlled by the oxidation time. The SEM images for the fabricated ridge and channel waveguides are shown in Fig. 4-3(a) and (b), respectively.
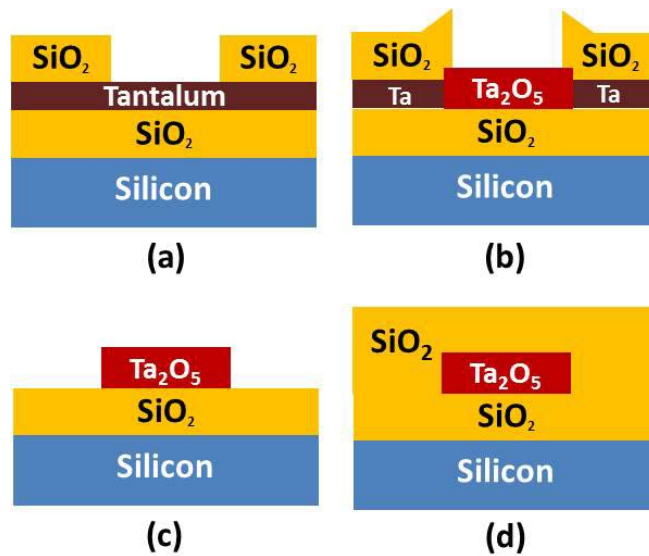
Figure 4-2: The processing steps of the proposed SORM waveguide fabrication technique [97].
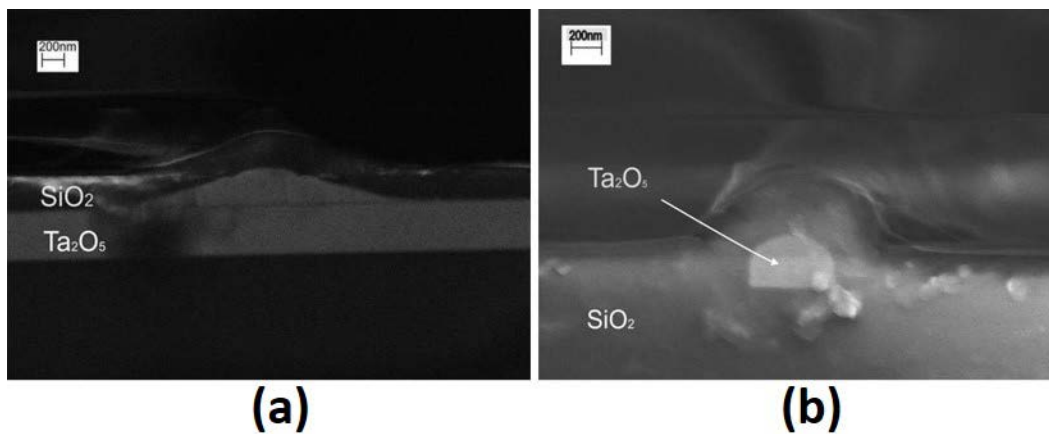
Figure 4-3: The SEM cross-section images of the fabricated devices: (a) ridge and (b) channel waveguides [97].

Ta_2O_5 micro-ring resonators were fabricated using the SORM technology in order to validate the new fabrication method. The microscope image of a fabricated micro-ring resonator with input and output bent bus waveguides is shown in Fig. 4-4(a). The transmission spectrum of the TE mode of the Ta_2O_5 ring resonator for different gap widths is shown in Fig. 4-4(b). The

propagation loss of the waveguide and the coupling strength were extracted by curve fitting to standard ring-resonator theories. The propagation loss is 9.5 dB/cm in a 300-µm diameter device. The loss is acceptable as an initial result considering that comparable values (8.5 dB/cm) are reported in the literature for much wider waveguides (18-µm wide). The unloaded quality factor of the resonator, Q, is estimated to be $\sim 4 \times 10^4$ and the unloaded finesse is 30.
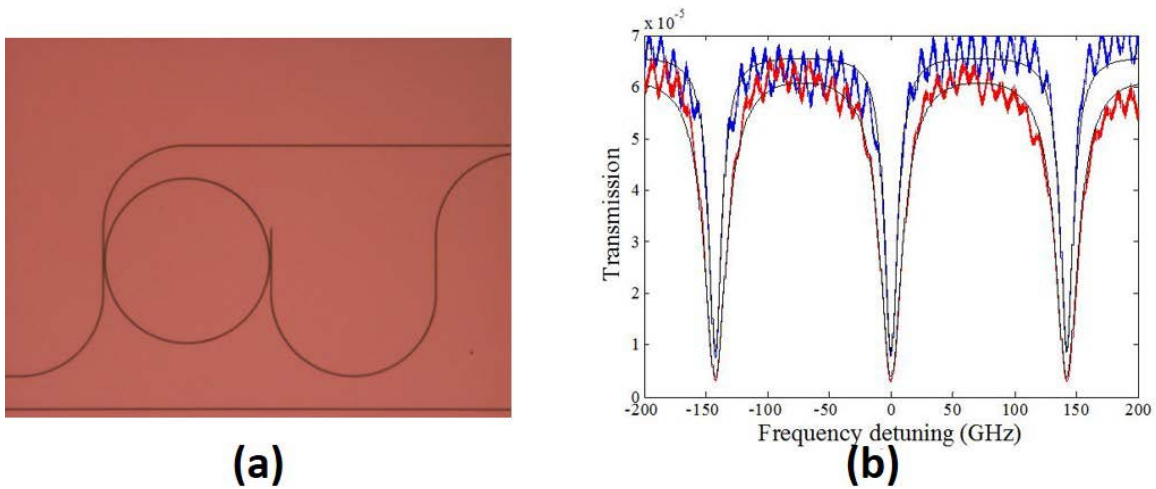
Figure 4-4: (a) Top-view high-magnification optical microscope image of a fabricated ring-resonator with input and output bent bus waveguides. (b) TE transmission spectrum of a device with 300-µm diameter and for various coupling strengths and the fitted spectrum around 1550 nm [97].

4.3   LiNbO$_3$-on-Si Waveguides and Micro Resonators

The fabrication method that allows achieving submicron LiNbO$_3$ is waveguides on silicon substrate compromises of two key proprietary technologies: (a) Thermal bonding of submicron thin films of LiNbO$_3$ on silicon; and (b) an etchless technique to achieve low-loss ridge waveguides, which has been described in detail in Section 4.2.

The demonstrated fabrication steps are presented in Fig. 4-5 [92]. The bonding process starts with ion implantation of a LiNbO$_3$ wafer to high doses of H$_e^+$ ions. A silicon wafer is coated by a ~2-µm-thick SiO$_2$ buffer layer. The two wafers are then polished and brought into contact at room temperature. After the room-temperature initial bonding, a heating process at 200°C is employed to improve the bonding. During the heating process, the implanted ions form a very high-pressure He gas in the implanted layer that forces the crystal to be sliced precisely at the peak position of the implanted species. Figure 3(e) shows an image of a 3'' thin film of bonded to a 4'' silicon wafer with no evidence of cracking or other bonding issues.

After wafer boning, the ridge waveguides are fabricated using the SORM method mentioned in Section 4.2. A 30-nm layer of SiO$_2$ is first deposited on LiNbO$_3$-on-Si wafers as a diffusion barrier to prevent out-diffusion of oxygen from LiNbO$_3$ in the Ta oxidation step. Then, Ta is deposited on LiNbO$_3$ thin films. A PECVD SiO$_2$ mask is then patterned on Ta by e-beam lithography for selective oxidation of Ta at 520°C. After oxidation, a composite rib-loaded waveguide is formed consisting of Ta$_2$O$_5$ ridge layer and LiNbO$_3$ slab layer. The mask layer is subsequently removed, the remaining non-oxidized tantalum layer is dry-etched in RIE using a chlorine-based recipe. The device is then covered with SiO$_2$ for passivation. In the end, for fabrication of EO modulators (Mach-Zehnder (MZ) interferometer-based or Ring-resonator-based), metal electrodes are added to the device using standard fabrication techniques. Figure 4-6(a) illustrates the cross section of the waveguide structure at one arm of the modulator with RF electric field in the LiNbO$_3$ active region. The corresponding SEM image of the fabricated waveguide is shown in Fig. 4-6(b).
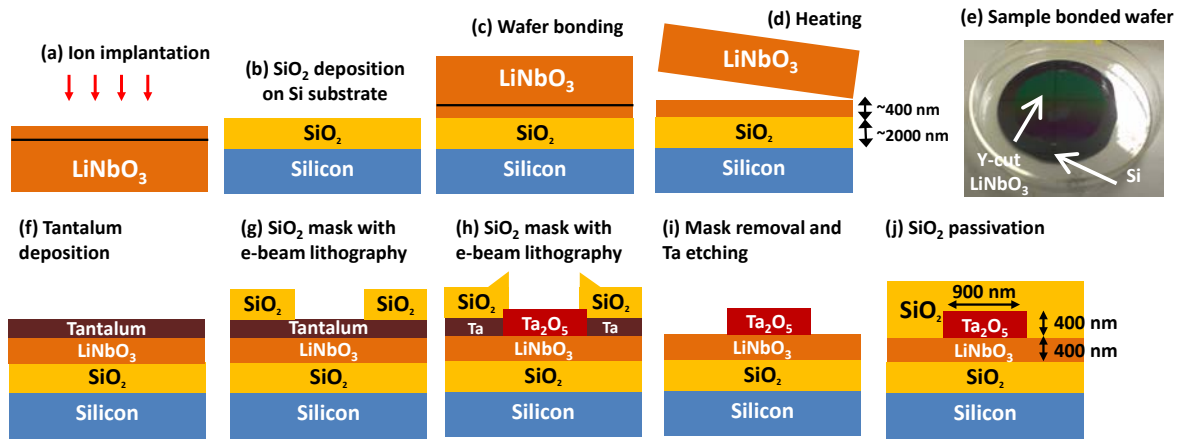
Figure 4-5: (a)-(d) Process steps for the fabrication of LiNbO₃-on-Si wafers; (e) Picture of successful bonding of a 3-inch Y-cut LiNbO₃ wafer bonded to a 4-inch silicon wafer; (f)-(j)The proposed process steps of selective oxidation of tantalum to form submicron LiNbO₃ ridge waveguide on silicon [92].
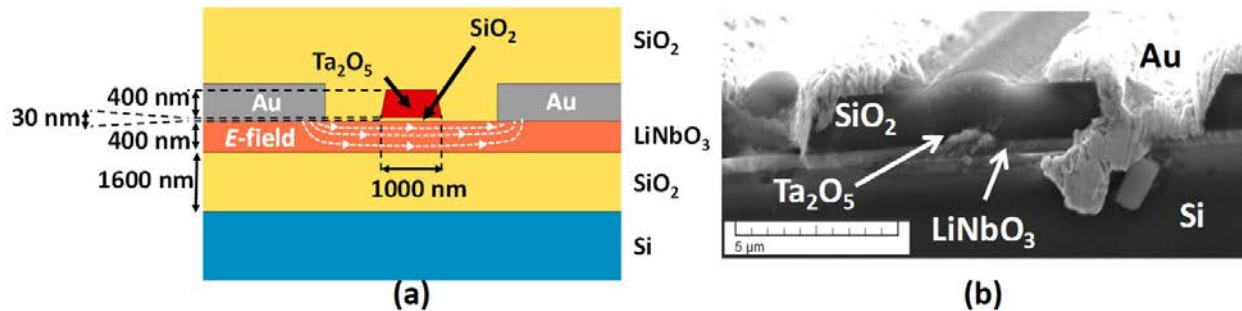
Figure 4-6: (a) Cross section of the waveguide structure at one arm of the modulator and simplistic RF electric field profile in the LiNbO₃ active region. (b) SEM image of cross section of a fabricated LiNbO₃-on-silicon waveguide [92].

An important advantage of the submicron, tightly-confined waveguides is that the electrodes can be placed much closer to the waveguides without significant absorption of light by the metallic electrodes. This reduces the voltage needed to obtain the same electric field for EO modulation. According to simulations, the gap between the electrodes can be as small as 4 µm

without overlap between the highly-confined optical mode and the electrodes. This is smaller by a factor of 5 compared to traditional LiNbO$_3$ EO modulators [92].

The measurement results of the fabricated devices are presented in Fig. 4-7. The loaded Q of the ring resonator is 4.5×10^4 (Fig. 4-7(a)), which is over an order of magnitude higher than previous results [100]. The linear propagation loss is around 5 dB/cm. The the MZ modulators were characterized by applying a sawtooth modulation voltage at 1 kHz on a device with 7 µm gap between the electrodes. The measured V_π is 6.8 V, which corresponds to a (half-wave voltage-length) of 4 V·cm for 6-mm-long electrodes, much lower than $V_\pi·L$ of diffusion-based modulators [101]. The extinction ratio of the modulator is approximately 20 dB.

(a)   (b)
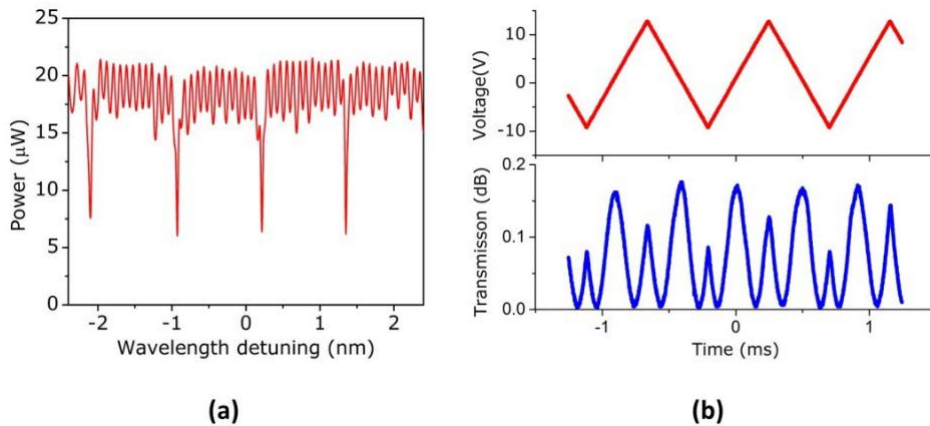
Figure 4-7: (a) Transmission spectrum of a microresonator with 300 µm diameter for the TE mode around 1550 nm wavelength. The resonance linewidth is 2.7 GHz; (b) Applied sawtooth electrical signal and the measured modulation response of a 6-mm-long Mach-Zehnder modulator [92].

The experimental results we got so far confirm that the LiNbO$_3$-on-Si platform is quite promising for a host of applications such as optical communications, optical sensing, nonlinear photonics and quantum optics.

73

4.4   Nonlinear Integrated Photonics in LiNbO$_3$ and Ta$_2$O$_5$-on-Si Waveguides

As discussed before, silicon photonics has been pursued as a platform for integrated nonlinear optics. However, the second-order susceptibility is nonexistent in silicon. Although the third-order nonlinearity of silicon has been aggressively studied in the last decade [41], nonlinear losses due to TPA and FCA at high optical intensities limit the performance of the $\chi^{(3)}$ devices. The two platforms described in Sections 4.2 and 4.3 are ideal candidates for integrated $\chi^{(2)}$ and $\chi^{(3)}$ nonlinear optics, provided that the propagation losses of the fabricated waveguides are reasonably low.

4.4.1   Third-Harmonic Generation in Ta$_2$O$_5$-on-Si

For certain application (e.g., green light generation from infrared sources via third-harmonic generation (THG), which cannot be realized in silicon waveguides because the generated visible light will be absorbed by silicon), $\chi^{(3)}$ materials are useful. Compared with other $\chi^{(3)}$ materials that have been studied by researchers, such as chalcogenide glasses and Hydex, Ta$_2$O$_5$ has a comparable nonlinear refractive index ($n_2 = 7.23 \times 10^{19}$), relatively higher refractive index (~2.2) and higher damage threshold. Therefore, the Ta$_2$O$_5$-on-Si waveguide technology is an attractive platform in this regard and worth pursuing. R. Y. Chen *et al*. have reported THG in lossy (8.5 dB/cm) and wide Ta$_2$O$_5$ waveguides using high-power femtosecond lasers [102]. The reduction of the waveguide dimensions in our submicron waveguides, as well as the low losses expected in the etchless fabrication technique, make it possible to demonstrate THG in Ta$_2$O$_5$ waveguides using CW sources like high-power EDFAs.

The phase-matching condition for THG is $n_{3\omega} = n_\omega$, i.e., the effective refractive indices for the pump and the third-harmonic signal should be identical. This can be achieved by dispersion engineering of the waveguide. The calculations shown in Fig. 4-8 are based on numerical simulations of waveguide effective indices using a commercial beam propagation method solver (COMSOL). The refractive indices of bulk Ta_2O_5 at the pump (1550 nm) and the third-harmonic signal (517 nm) are measured by an ellipsometer. The TE_{15} mode at 517 nm is used along with the fundamental TE_{11} mode at 1550 nm to achieve phase matching. The lower order modes of the waveguide at 517 nm (e.g., TE_{13} mode), which have larger overlap integral with TE_{11} mode at 1550 nm, are not feasible in this case because our Ta_2O_5 obtained by Ta oxidation is quite dispersive.
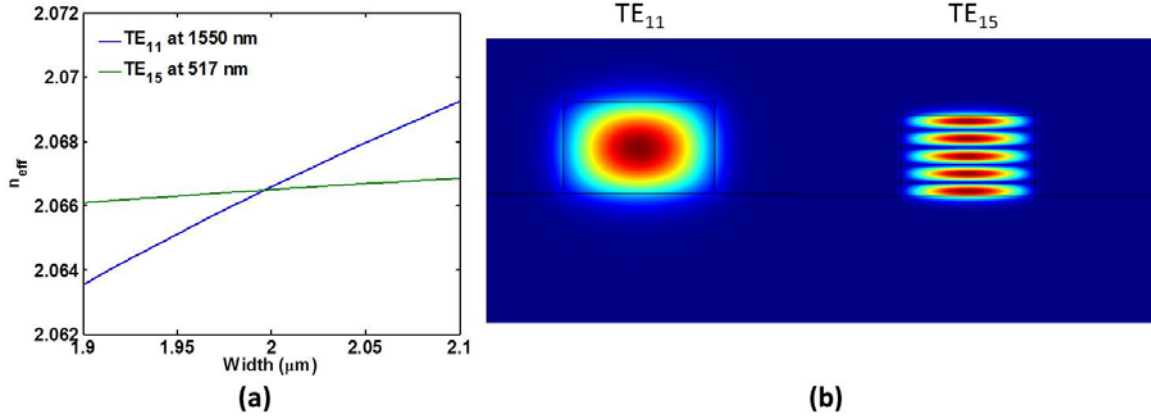
Figure 4-8: (a) Dispersion of Ta_2O_5 waveguides for THG; (b) The optical modes of fundamental TE_{11} (pump at 1550 nm) and higher-order TE_{15} (signal at 517 nm) of a designed waveguide that satisfies the phase-matching condition. The height of the channel waveguide is 1.2 µm.

4.4.2 Second-Harmonic Generation in LiNbO₃-on-Si

The performance of nonlinear devices operating based on $\chi^{(3)}$ effects cannot in principle compete with devices based on $\chi^{(2)}$ effects for most applications such as quantum optics. With the submicron LiNbO₃ waveguide technology presented in Section 4.3, dispersion engineering becomes possible through the geometrical design of the ridge waveguides. This is a big advantage compared with traditional LiNbO₃ integrated optics technology. The key to high conversion efficiency in second-harmonic generation (SHG) is fulfilling the phase matching condition, i.e., $n_{2\omega} = n_\omega$. The anisotropy of LiNbO₃ can be exploited to satisfy this condition. Two photons polarized along the ordinary axis (TM_{11} mode) can be phase-matched to a second-harmonic photon along extraordinary axis (TE_{11} mode). It is known as "Type I SHG". Similar to

76

the THG case, a waveguide with slab (LiNbO$_3$) height of 1560 nm, ridge (Ta$_2$O$_5$) width of 2.31 µm and ridge height of 600 nm is designed to satisfy the phase-matching condition (Fig. 4-9).
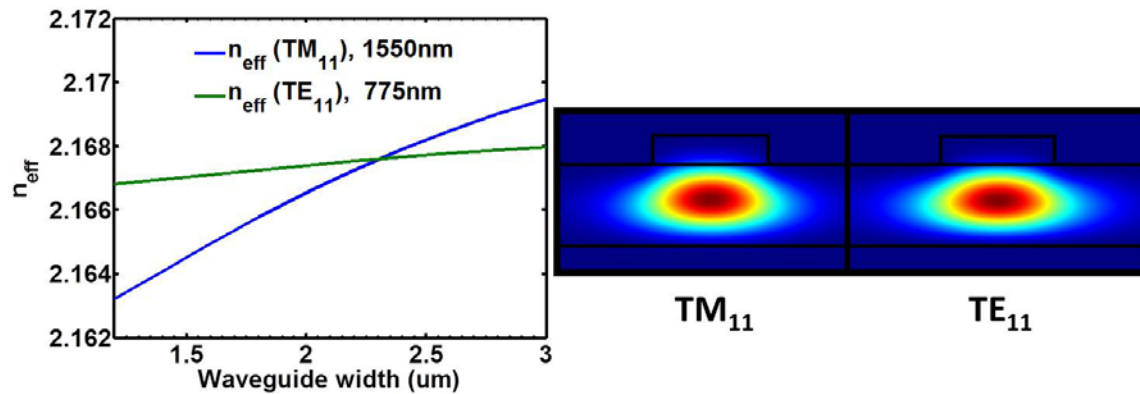
Figure 4-9: (a) Dispersion plot of LiNbO$_3$ waveguides for SHG; (b) The optical profiles of fundamental TM (pump at 1550 nm) and TE (signal at 775 nm) modes of a designed waveguide that satisfies the phase-matching condition corresponding to the crossover in (a): Ridge width: 2.31 µm, slab height 1560 nm, ridge height 600 nm.

CHAPTER 5: TWO-PHOTON PHOTOVOLTAIC EFFECT IN GALLIUM ARSENIDE

5.1   Background

Photovoltaics is the process of converting light into electricity using solar cells. Nowadays, it is a rapidly growing and increasingly important technology developed for resolving the global energy crisis. Two-photon photovoltaic (TPPV) effect is harvesting the energy of the photons lost to TPA. The effect is a nonlinear equivalent of the conventional (single-photon) photovoltaic effect widely used in solar cells.

The TPPV effect was first demonstrated in silicon [14]. Although the main purpose was to eliminate the nonlinear loss in silicon waveguides by decreasing the carrier lifetime, at the same time, electrical energy was harvested from the silicon photonics devices. In Ref. [14], the electron-hole collection efficiency of the process reached ~40% and is nearly independent of the coupled optical intensity from 5 to 150 MW/cm^2. It is also proved by simulations the maximum generated electrical power can go above 40 mW in a 1-cm-long device pumped with an optical intensity of 150 MW/cm^2. This reasonable power efficiency makes it possible to utilize the energy harvested through the TPPV effect to supply the electrical power on-chip. Energy harvesting (or negative electrical power dissipation) based on TPPV effect in silicon has been demonstrated in Raman amplifiers [103], parametric wavelength converters [69], and electro-optical modulators [104].

In principle, every two photons lost only to TPA generate one electron-hole pair in the semiconductor material and these photogenerated carriers are available for photovoltaic conversion into electrical power. Figure 6-1(a) shows the TPA process at the two particular wavelengths studied here, 976 nm and 1550 nm. Figure 6-1(b) shows a simplified schematic on how nonlinear absorption along the waveguide (due to TPA at high optical intensities) is different than linear absorption at low intensities. FCA is ignored in this simplified diagram.
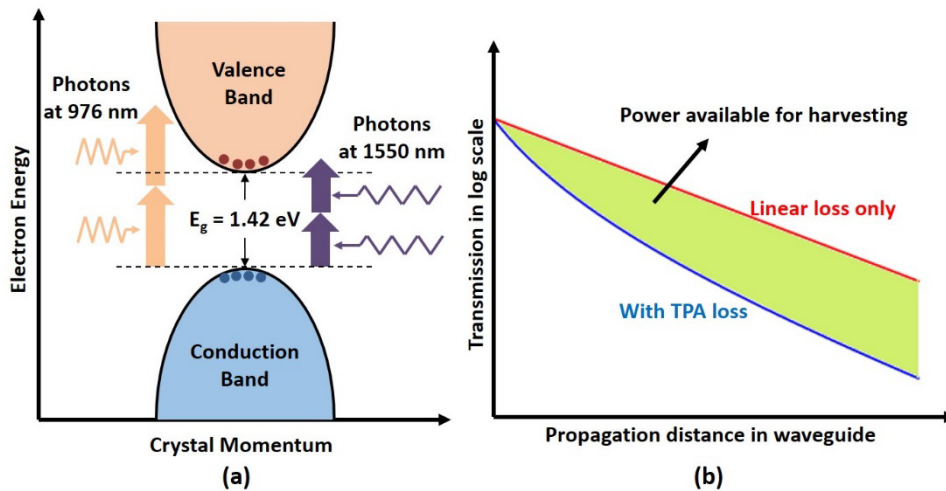
Figure 5-1: (a) Two-photon absorption (TPA) in GaAs at wavelengths of 976 and 1550 nm; (b) Waveguide loss with and without TPA. The carriers generated in GaAs by TPA are in principle available for photovoltaic conversion (free-carrier absorption has been ignored in this simplified diagram) [105].

One possible application of the TPPV is self-powered optoelectronic chips. Figure 6-1 shows the schematic of an electronic-photonic integrated circuit that is fully powered by an off-chip laser source [16]. It should be mentioned that only a small fraction of the signal is absorbed by TPA while most of the light is passed through the waveguide. This means the optical transmission of the photonic devices can still be measured and characterized while at the same

time the photodetectors or the sensing circuitry can be driven by the electrical power harvested through the TPPV effect. Another possible application of the TPPV effect is remote power delivery. Sometimes sensors used for temperature or pressure measurement are installed in critical environments (e.g., in coal mines) where potential danger or hazard exist if the sensors are powered electrically (e.g., using copper cable). Photovoltaic power converters (PPCs) based on the TPPV effect could be possibly applied in such cases.
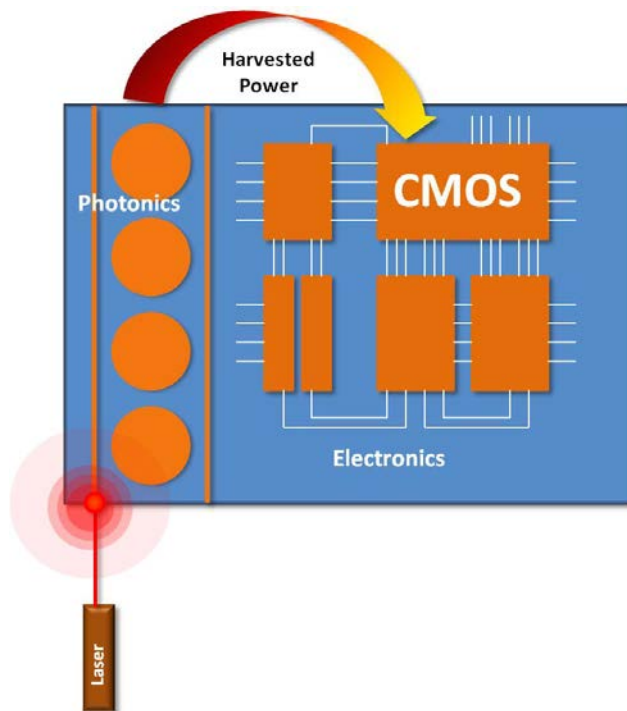
Figure 5-2: An electronic-photonic integrated circuit fully powered by an off-chip laser source using the TPPV effect.

The TPPV effect is not restricted to Si. It is also applicable to III-V semiconductors. TPA was observed experimentally in GaAs and the TPA coefficient β reported at 1.3 µm in GaAs is 70 cm/GW, much higher than in Si (3.3 cm/GW) [106]. Thus, the TPPV effect is expected to be

stronger in GaAs. It has been reported that at wavelength of 1.3 µm, the maximum power efficiency for GaAs is as high as 9%, achieved at optical intensities of below 5 MW/cm^2 [16].

5.2   Model

Figure 5-3 illustrates how TPPV can be realized in a single-mode GaAs/AlGaAs waveguide using a p-i-n junction diode. The employed device resembles a standard edge-emitting laser but without any active (quantum well) region. A theoretical model is developed to describe the TPPV effect in the GaAs/AlGaAs waveguide with vertical p-i-n heterojunction diodes shown in Fig. 6-3. Although a one-dimensional (1D) model is enough for simulation of the conventional solar cells, a 2D approach is applied here considering the optical intensity distribution of the guided mode. The junction cross section is in the x-y plane and light is propagating along the z-direction. Taking into account the loss due to nonlinear absorption (TPA and FCA), the optical intensity $I(z)$ propagating along the waveguide is governed by:

$$dI(z)/dz = -\alpha I(z) - \beta I^2(z) - \alpha_{FCA} I(z) \tag{5.1}$$

where α is the linear propagation loss and β is the TPA coefficient. α_{FCA} is the FCA coefficient calculated by $\alpha_{FCA} = 6.0 \times 10^{-18} \Delta N \cdot (\lambda/2)^2$ (cm^{-1}), where ΔN is the free carrier concentration in cm^{-3} and λ is the wavelength in µm [107]. ΔN depends on optical intensity $I(z)$ and bias voltage V and is calculated numerically.
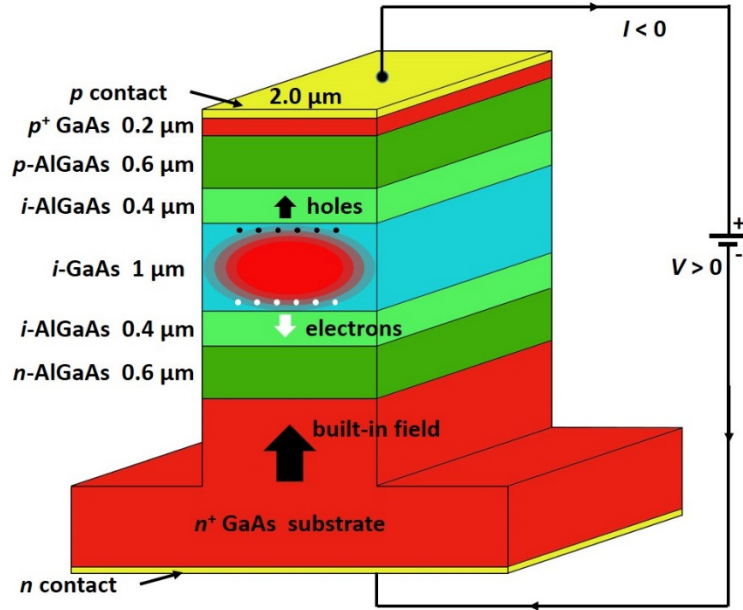
Figure 5-3: Schematic of the designed GaAs/AlGaAs waveguide with a p-i-n junction diode.

The 2D numerical model is developed in COMSOL[TM]'s Multiphysics module. Different from simulation of homojunction diode, the model uses the drift-diffusion approach in combination with Poisson's equation [108]. The steady state current continuity equations for electrons (J_n) and holes (J_p) are [109]:

$$\nabla J_n = qR_{SRH} - qG_n \tag{5.2}$$

$$\nabla J_n = -qR_{SRH} + qG_p \tag{5.3}$$

$$\nabla(\varepsilon \nabla \psi) = -q(p - n + N_D - N_A) \tag{5.4}$$

where q is the electron charge, ε is the dielectric permittivity, p and n are the hole and electron densities, N_D and N_A are the ionized donor and acceptor concentrations. ψ is the electrostatic potential. R_{SRH} represents the Shockley-Read-Hall recombination. Assuming the trap energy level is located at the middle of the band gap, the rate is given by [109]:

$$R_{SRH} = \frac{np - n_i^2}{\tau_n(p + n_i) + \tau_p(n + n_i)}$$

(5.5)

where n_i is the intrinsic carrier density. τ_n and τ_p are electron and hole bulk recombination lifetimes, respectively. The carrier photogeneration rate from TPA is [14]:

$$G_n = G_p = \beta\lambda I^2(z)/2hc$$

(5.6)

where h is the Planck's constant and c is the speed of light in vacuum.

The large dynamic range of the carrier concentrations, especially in the vicinity of the heterojunction interface, makes the numerical solver difficult to converge. Therefore, the current density functions are expressed in terms of the Fermi levels for electrons (ϕ_n) and holes (ϕ_p) [109]:

$$J_n = \mu_n n(d\phi_n/dz)$$

(5.7)

$$J_p = \mu_p p(d\phi_p/dz)$$

(5.8)

where μ_n and μ_p are the electron and hole mobilities, respectively.

τ_n and τ_p in bulk GaAs are on the order of 10^{-8} s, about two orders of magnitude smaller than those in bulk silicon. In GaAs/AlGaAs waveguide, the effective free carrier lifetime τ_{eff} can be even smaller when the surface recombination at the sidewalls dominates over the bulk recombination. τ_{eff} of 250 ps is reported for a 2.4 µm × 0.8 µm GaAs/Al$_{0.8}$Ga$_{0.2}$As ridge waveguide [110]. In this work, τ_{eff} is assumed to be 100 ps as good agreement between numerical simulation and experimental data is achieved under this assumption (Fig. 5-5(b) and Fig. 5-7(b) in Section 5.3). This value is reasonable considering the sidewall roughness induced by the dry

etching process, which might accelerate the surface recombination. Table 6.1 summaries the

other parameters and material properties used in the simulation.

Table 6-1: Material properties used in this study.

Parameters	Unit	GaAs	$Al_{0.15}Ga_{0.85}As$
ε_r (976 nm)	--	12.42	11.88
ε_r (1550 nm)	--	11.41	11.27
n_i	cm^{-3}	2.2×10^6	6.6×10^4
μ_n	$cm^2/(Vs)$	8500	4925
μ_p	$cm^2/(Vs)$	400	241
m_e	m_0	0.067	0.076
m_h	m_0	0.48	0.548
E_g	eV	1.42	1.611
X	eV	4.06	3.905

In Table 6-1, ε_r is the relative permittivity, m_e and m_h are the effective mass of electron

and hole, respectively. $m_0 = 9.1 \times 10^{-31}$ kg is the electron mass. E_g is the energy bandgap, and X

is the electron affinity.

Equations (5.2)-(5.4), (5.7) and (5.8) are first solved assuming no optical input and zero

bias voltage. Then the input power is increased from zero in small steps (1 mW) and the solution

from a previous step is used as the initial condition for the next one. After solving the Fermi

levels at a certain optical intensity, similar method for parameter sweep is applied to scan the

bias voltage V from 0 V to 1.2 V in steps of 0.025 V. The reverse-bias case can be calculated in

the same way but is not considered in this study as the junction diode must be biased in the

fourth quadrant (current $I_c < 0$ and $V > 0$) in order to achieve energy harvesting. From the

current density $J = J_n + J_p$ provided by COMSOL, the total current I_c is then calculated by

integrating J over the waveguide length L.

At last, the ohmic loss of the electrodes and the contacts must be included. A series resistance R_s in the circuit will reduce the harvested electrical power and might possibly lower the short-circuit current if R_s is excessively high. In order to model this effect, the I_c dependence on the bias voltage V is first nonlinearly fitted to an exponential function:

$$I_c(V) = -A + B \exp[qV / (nkT)] \tag{5.9}$$

where k is the Boltzmann constant and T is the room temperature (300 K). A and B are fitting parameters. Then, the final current collected, taking into account the series resistance R_s in the circuit, is numerically solved from the following equation:

$$I_c(V) = -A + B \exp[\frac{q(V + I_c R_s)}{nkT}] \tag{5.10}$$

5.3   Experimental Results on TPPV Effect in GaAs

The junction diode in Fig. 5-3 was fabricated using CREOL's cleanroom facility. The heterostructures in Fig. 5-3 were grown by molecular beam epitaxy. The negative electrode (a 15-nm-thick chromium layer plus a 200-nm-thick gold layer) was first deposited on the bottom of the wafer using a thermal evaporator. The purpose of the chromium layer is to make better adhesion between the gold layer and the bottom of the substrate. Then the waveguides were patterned by ultraviolet photolithography using negative photoresist NR7-1000 PY. A 17-μm-wide taper was added at the output end of the waveguide. This makes it easier to add probe from top and has little influence on the TPPV effect as the optical intensity in the taper is low. After photolithography, another 300-nm-thick gold layer was deposited on top of the sample and then the photoresist was removed by acetone. The top gold layer after lift-off served as both the

positive electrode and the mask for GaAs etching. In the end, the GaAs/AlGaAs multilayer structure was etched using an inductively-coupled-plasma (ICP) reactive ion etcher (RIE) from Plasma-Therm. The 4.2-µm-deep dry etching was divided into three steps and a few seconds of wet etching was performed in the middle in order to remove the residue. The length of the waveguide is 4.5 mm after cleaving.

Figure 5-4 shows the set up for characterization of the TPPV effect in the fabricated junction diodes. Optical power (from a high-power diode laser at 976 nm or from an erbium-doped fiber amplifier (EDFA) at 1550 nm) is coupled into the intrinsic GaAs layer through a lensed-fiber. The linear propagation loss α of the waveguide is measured by cut-back method and is estimated to be 7 dB/cm at 976 nm and around 18 dB/cm at 1550 nm. The high linear loss at 1550 nm can be explained by the mode leakage into the n^+-GaAs substrate as the AlGaAs bottom cladding layer is only 1 µm thick. In order to reduce the mode leakage and increase the power efficiency of the device at this longer wavelength (1550 nm), the bottom cladding layer has to be thicker than 2 µm, according to the mode profile and complex refractive index calculated by COMSOL. The current-voltage (I-V) characteristics of the fabricated waveguide diodes were measured with a curve-tracer at various coupled pump powers and wavelengths.
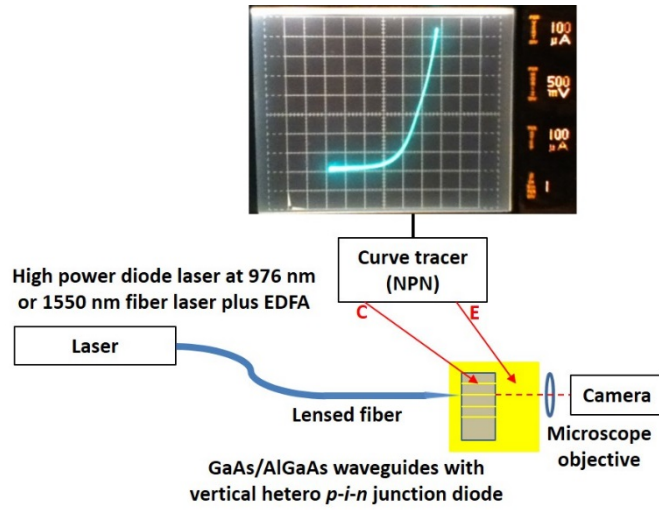
Figure 5-4: Set up for characterization of the TPPV effect in the p-i-n junction diode.

TPPV in GaAs was first investigated at 976 nm wavelength. In this case, (down to the center of the intrinsic AlGaAs top cladding). Figure 5-5(a) shows the measured *I-V* characteristics at three different laser diode powers. The TPPV effect is observed when the device is biased in the fourth quadrant of its *I-V* characteristics, i.e., the carriers generated by TPA are swept out by the built-in field of the *p-i-n* junction. The current measured is a combination of the photocurrent (from TPA), the minority carrier diffusion current and the recombination current including both bulk and surface recombination. The power-voltage (*P-V*) characteristics of the diode at three different pump powers are shown in Fig. 5-5(b). Evidently, over 200 µW of electrical power can be scavenged from this device. The solid lines show the numerical simulation results based on the theoretical model in Section 5.2 for comparison. It is clear that the simulation results show excellent agreement with experimental results when the diode is biased in the fourth quadrant of its *P-V* characteristics. R_s and β are treated as fitting parameters in the simulation and are estimated to be around 700 Ω and 40 cm/GW, respectively.

The β obtained here is comparable to the values reported in references [106,107]. It should be mentioned that the device has also been tested before annealing. At pump power of 55 mW, the generated electrical power is only half of that harvested from an annealed device. This indicates that annealing alleviates the ohmic loss remarkably and is crucial in fabrication of photovoltaic devices. Up to 9% power efficiency, excluding the coupling loss, is theoretically predicted in long (several centimeters), low-loss GaAs waveguides [16]. The rather low wall-plug efficiency observed here is attributed to high linear propagation loss due to fabrication imperfections, as well as the high series resistance at the contacts.
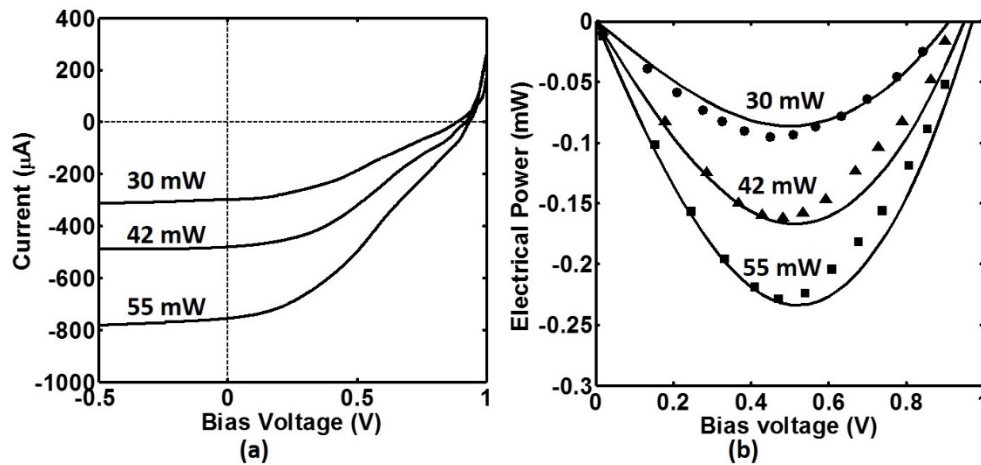
Figure 5-5: (a) *I-V* characteristics of the diodes at wavelength of 976 nm for three different input powers. (b) The corresponding *P-V* characteristics of the diodes from numerical simulation (solid line) and experiment (circles, triangles and squares).

Figure 5-6(a) shows the *I-V* characteristics of a similar device, which has the same multilayer structure as in Fig. 5-3, but an etch depth of 1.0 μm (down to the center of the AlGaAs cladding layer), also characterized at wavelength of 976 nm. The shallow-etched device has two advantages compared with the previous deep-etched one. First, the GaAs core layer is

not etched so the scattering loss of the optical mode is less and the surface recombination is weakened; second, the top contact gold layer is thicker due to less etching time in the process, which decreases R_s by about 200 Ω. However, the generated photocurrent, as well as the harvested electrical power are less than those of the deep-etched device because of the existence of a huge slab mode, which results in low optical intensity in the waveguide core. Moreover, the photons generated in the slab cannot be efficiently collected by the circuit. Figure 5-6(b) presents the electrical power harvested from a load resistance of 1 kΩ (without bias), for both etch depths. This resembles the case of a self-powered electronic-photonic integrated circuit mentioned in Section 5.1.
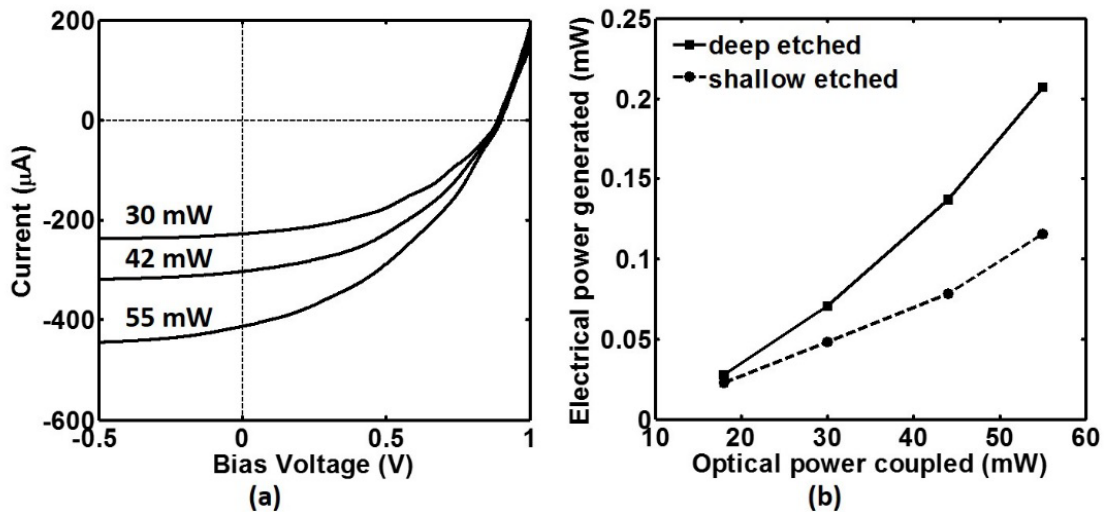
Figure 5-6: (a) *I-V* characteristics of the shallow-etched devices at wavelength of 976 nm for three different input powers. (b) The electrical power generated on a 1 kΩ load resistance for both etch depths.

Next, TPPV in GaAs was studied at the telecommunication wavelength of 1550 nm. The *I-V* and *P-V* characteristics measured at three different input powers are shown in Fig. 5-7(a) and (b), respectively. Once more, good agreement between the numerical modeling and the

experimental results is observed. β is estimated to be 17 cm/GW at this wavelength, in accordance with the value reported in Ref [107], and is still much higher than that in silicon (0.7 cm/GW at 1550 nm). 230 µW of electrical power is generated at input power of 90 mW.
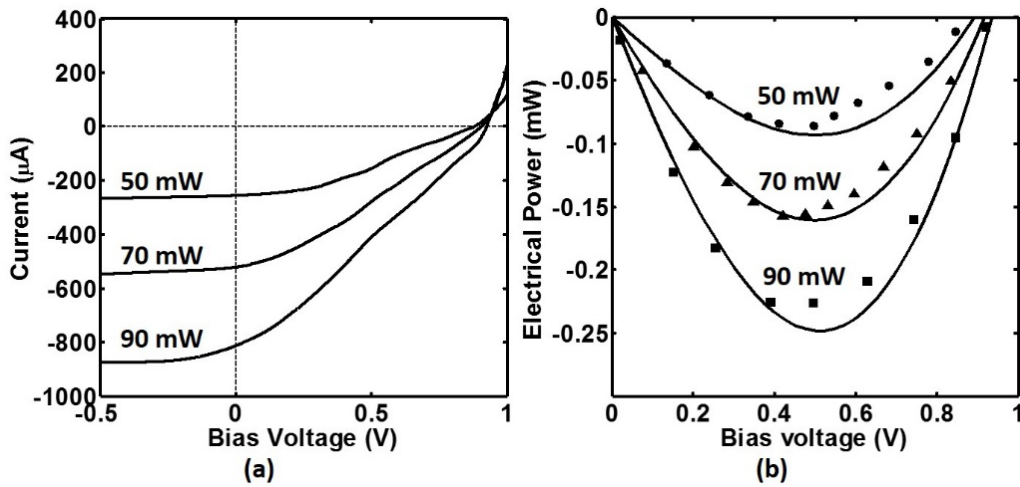

Figure 5-7: (a) *I-V* characteristics of the shallow-etched devices at wavelength of 976 nm for three different input powers. (b) The electrical power generated on a 1 kΩ load resistance for both etch depths.
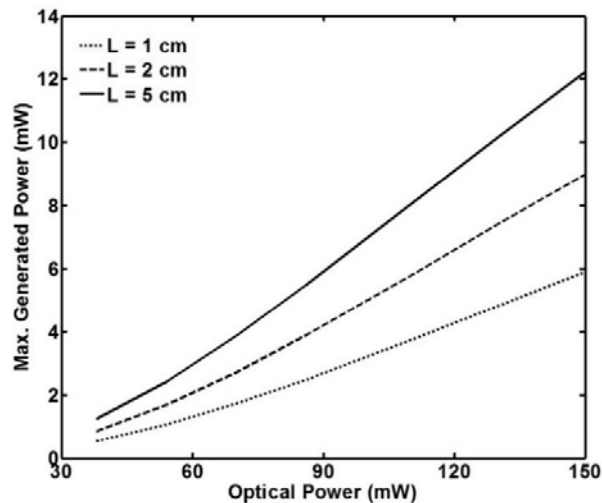
Figure 5-8: Theoretical study of the maximum possible electrical power generation versus coupled optical power for three different device lengths of 1, 2, and 5 cm.

Figure 5-8 presents the simulated maximum possible generated electrical power versus input power for three different waveguide lengths. Negligible ohmic loss of the contacts, as well as low linear propagation loss of 1 dB/cm are assumed in this simulation. Such low α is achievable in micron size waveguides if the bottom cladding layer is designed to be thicker and the fabrication processes, especially the dry etching recipe are optimized. 12 mW of electrical power can be harvested at input power of 150 mW in a 5-cm long device, i.e., a power efficiency of 8% is theoretically predicted in this case. At higher input power, a slight increase in the slope is clearly visible in all three lines, as well as in Fig. 5-6(b). This does not happen in silicon (Fig. 5 of Ref [14]) due to the high FCA loss in silicon waveguides. In GaAs, the carrier recombination lifetime is two orders of magnitude smaller than in silicon. Although the photogenerated carriers recombine faster before they are collected by the circuit, at the same time, the optical loss due to FCA is greatly reduced. Further increasing the length of the waveguide can only slightly improve the power efficiency as the optical intensity is not high enough after the light propagates a certain distance along the waveguide and gets absorbed gradually.

CHAPTER 6: PLASMONIC-ENHANCED SILICON PHOTOVOLTAIC DEVICES

6.1   Background

Photovoltaic (or solar) cells are undoubtedly one of the most promising 'green' technologies for alleviating the energy crisis facing the human civilization in the coming decades. Bulk silicon solar cells with 200-300 μm thicknesses currently dominate the solar cell market. Recently, enhancement of photovoltaic effect using surface plasmon polaritons has been proposed and demonstrated as an alternative method to achieve cost-effective thin-film Si solar cells [111]. In these devices, conventional solar cells are covered with metallic (usually silver or gold) nanoparticles. The nanoparticles are self-assembled by thin film (10-20 nm) metal deposition followed by coalescing metal particles via thermal annealing. Depending on the deposited thickness and annealing conditions, colloidal islands with 50-100 nm heights and diameters are self-formed [112]. These subwavelength nanoparticles are capable of enhancing the photocurrent generation in solar cells via plasmonic effects.

Two mechanisms have been proposed to explain the improved performances [111,113]: (a) the impinged light can resonantly couple into the localized surface plasmons of the conduction electrons in the nanoparticles. The curved surfaces of the particles applies a restoring force on the resonantly driven electrons and near-field amplification occurs in the high-index material (Si); (b) simultaneously, light scattering via the metallic nanoparticles occurs, which

leads to enhanced light trapping. As a result, thin film solar cells enhanced by plasmonics can be demonstrated.

Based on the discussed plasmonic enhancement of photogeneration via metallic nanoparticles, Stuart and Hall demonstrated an up to 18-fold photocurrent enhancement at around 800 nm in 165 nm thick silicon-on-insulator (SOI) photodetectors [114]. Yu and co-workers have more recently shown enhanced performance of photodetectors (up to 80%) at about 500 nm wavelength [112]. The same group has used gold nanoparticles and reported more than 8% increase in power efficiency of plasmonic solar cells as compared with conventional solar cells without nanoparticles [115]. Pillai *et al.* have applied the same technique and demonstrated increase in photocurrent generation in 1.25 μm thick SOI solar cells [111]. Finally, it is noteworthy that plasmonic-enhanced photovoltaic effect has been studied in materials other than Si (e.g., GaAs), a review of which can be found elsewhere [113].

6.2   Plasmonic-Enhanced Solar Cells Using Non-Spherical Nanoparticles

Subwavelength metal nanoparticles are strong scatterers of light at wavelengths near the plasmon resonance. For spherical subwavelength particles, the scattering and absorption cross-sections follow the metal polarizability given by [116]:

$$\alpha_p = 3V \left[\frac{\varepsilon_p - \varepsilon_m}{\varepsilon_p + 2\varepsilon_m} \right], \tag{6.1}$$

where V is the nanosphere volume, ε_p is the dielectric function of the particle and ε_m is the dielectric function of the embedding medium. The polarizability has a resonant enhancement

93

when $|\varepsilon_p + 2\varepsilon_m|$ is a minimum. This is called Fröchlin's condition and the associated mode is called the 'dipole surface plasmon' of the nanoparticle. For metals with low interband absorption, the dielectric function can be described by Drude model. Using $\varepsilon_m = 11.9$ for Si, the dipole surface plasmon resonance of a silver spherical nanoparticle embedded in Si can be analytically calculated.

It has been shown that red-shifting and broadening of the plasmonic resonance occurs as a function of shape and size in non-symmetrical nanoparticles [117]. However, the analytical model is not applicable to analyze these non-spherical structures and numerical simulations are required. Here, the CST Microwave Studio for 3-D electromagnetic (EM) simulations is used. To confirm the validity of our simulation, spherical nanoparticles with 10 nm diameter embedded in Si were first studied. A resonance wavelength of 730 nm was obtained which is in close agreement with the 720 nm analytical value.
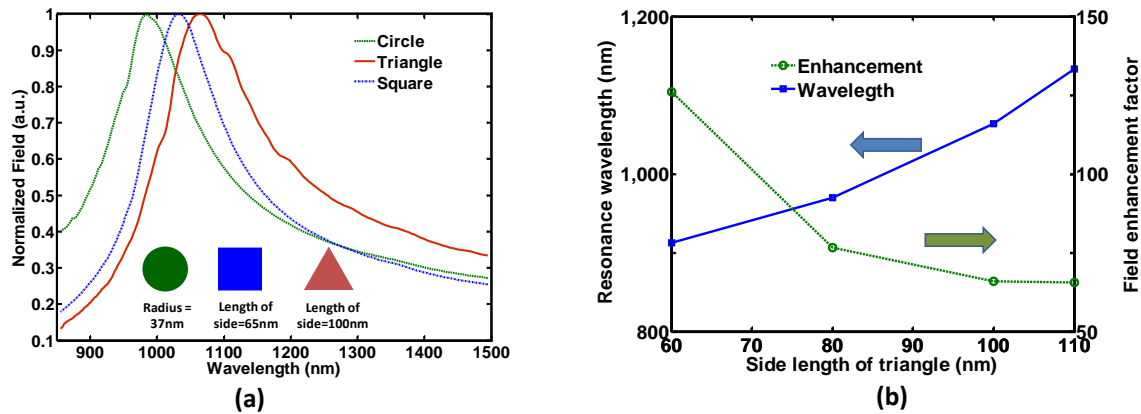
Figure 6-1: (a) Normalized field of surface plasmonic resonance in three different nanoparticle shapes with identical surface areas and 20 nm thicknesses on silicon substrates; (b) Resonance wavelength and maximum field enhancement factor versus side length in the triangular (prism-shaped) nanoparticles with 20 nm thicknesses.

The normalized electric field spectra for circular, square and triangular silver nanoparticles on Si substrates are shown in Fig. 6-1(a). The resonant wavelengths are at 935, 1032 and 1064 nm, respectively. The resonance wavelengths of the circular and square cases are longer than the spherical case, but they remain shorter than Si bandgap. It is clear that triangular (prism-shaped) nanoparticles provide the furthest resonance shift. The resonant wavelength can be increased to above Si bandgap (~1200 nm) by further increasing the side length of the triangle at the expense of decreased plasmonic enhancement factor as presented in Fig. 6-1(b). The simulated electric fields at 1064 nm wavelength normalized to an incident value of 1 V/m are plotted in Fig. 6-2(a) and (b). The enhanced field inside silicon is about two orders of magnitude (~98 times) stronger than the incident field. This is evident from the field versus device depth, along the dashed line of Fig. 6-2(b), plotted in Fig. 6-2(c).
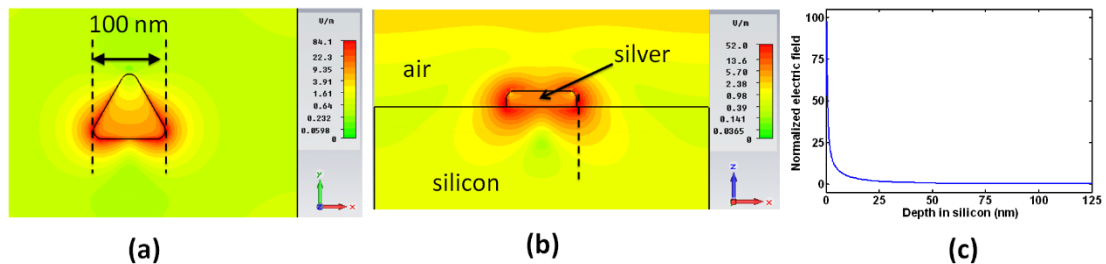
Figure 6-2: Electric field enhancement profile for 1 V/m incident field on a triangular nanoparticle. The incident E-field polarization is horizontal: (a) Top-view at silicon-metal interface; (b) Cross-section view along the horizontal triangle side in (a); (c) 1-D plot along the dashed line in (b).

Using the triangular nanoparticles that give the largest redshift of resonance, a possible scheme of plasmonic-enhanced solar cells is depicted in Fig. 6-3. Lateral *p-i-n* junction is applied here instead of the previously demonstrated vertical *p-n* junction because *p-i-n* solar cells can demonstrate enhanced efficiencies [118] as carrier transport is dominated by drift in the intrinsic

region of the diodes. The photogenerated carriers are accelerated out of the intrinsic region before they recombine and hence close to ideal quantum efficiency is expected [119]. Furthermore, wavy finger doped regions are included in our design such that each nanoparticle is closely surrounded by *p-* and *n*-doped regions. This allows the plasmonic region of each nanoparticle be situated in the middle of the drift region of the *p-i-n* diode path overlapping with it. The proposed scheme (Fig. 6-3) not only enhances the collection efficiency of the devices but also reduces the ohmic loss of the intrinsic regions in carrier transport.
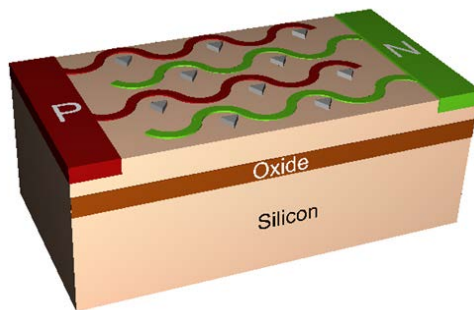
Figure 6-3: Schematic of proposed plasmonic-enhanced solar cells with lateral p-i-n junctions and nanoprism patterned nanoparticles.

6.3   Plasmonic-Enhanced Two-Photon Photovoltaic Power Converters Using Nanoaperture Structures

The TPPV effect discussed in Chapter 5 is the nonlinear equivalent of the photovoltaic effect of solar cells. As previously mentioned in Section 5.1, one possible application is PPCs that transform optical power into electrical power. The difference between a PPC and a solar cell is that the optical source in the case of a PPC is the output of a laser or a high-power light-emitting diode (LED) delivered to the PPC via optical fiber or free space.

PPCs based on conventional photovoltaics and compound semiconductors are available [120]. The disadvantage of using such a conventional scheme is that the devices are bulky and they suffer from self-heating. TPPV effect is a viable solution, especially for nanophotonics applications where local power generation on an integrated chip is demanded. The TPPV devices demonstrated so far [14] rely on optical waveguides for enhancing optical intensity (>10 MW/cm^2). However, the linear loss of submicron waveguides (required to achieve such high intensities with reasonable optical power) remain too high to date for the present CW application. Another problem is that very long waveguides (~10 cm) are required to absorb and convert all the optical energy into electrical power [16]. Plasmonic-enhanced TPPV in Si is proposed here to achieve ultracompact and highly-efficient nanophotovoltaic power converters.

Subwavelength apertures can be applied to photovoltaic power converters whose input is the beam of a narrow linewidth light-emitting diode or a laser source focused into the aperture. C-shaped single apertures have certain advantages over other possible configurations such as slit and circular apertures due to their compact structure, which does not require the presence of arrays or extensive corrugation. My colleagues and I studied the optical properties of C-shaped subwavelength apertures in metallic (silver) films on silicon substrate in the wavelength range of 0.6-6 µm [121].
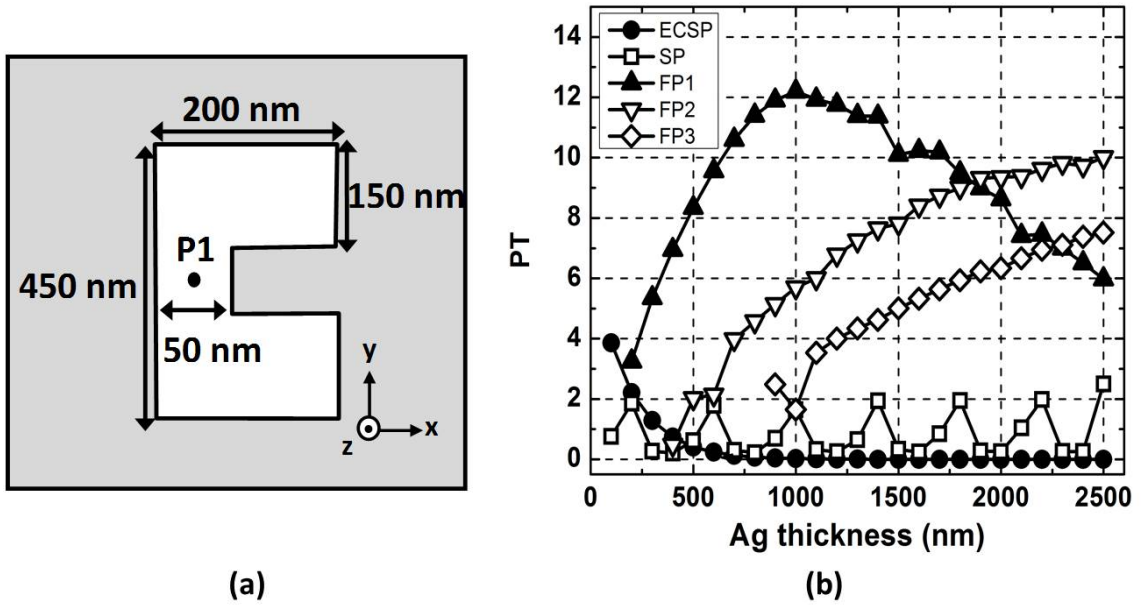
Figure 6-4: (a) Geometry and dimensions of the C-shaped aperture studied; (b) power throughput versus metal layer thickness for the five transmission modes considered in this study [121].

The geometrical dimensions for the designed C-shaped aperture are illustrated in Fig. 6-4(a). In Fig. 6-4(b), the power throughput (PT) of the aperture, which is defined as the ratio of the total power at the exit surface to that impinging upon the physical area of the aperture [122], was calculated and plotted versus metal layer thickness for five different transmission modes at their peak wavelengths. The transmission modes include one evanescently coupled surface plasmon (ESCP) mode, one thickness independent surface plasmon (SP) mode, and FP cavity modes. The number of the FP cavity modes increases with increasing thickness of the metal layer. Detailed physical explanations on these modes can be found in Ref. [121]. A PT of ~7 is predicted for FP1 mode at the telecommunication wavelength of 1.55 µm. The highest PT of 12 is predicted for the same mode at wavelength of 1.92 µm.

It should be mentioned that the above approaches are not power efficient in reality because the PTs in the simulations are normalized to the area of the aperture, not the real illuminated area. Enhancement of extraordinary transmission has been previously reported when periodic arrays of square-shaped nanoapertures are compared with single nanoapertures [123]. Thus, further enhancement is expected in arrays of our C-shaped apertures too. Such a proposed scheme is depicted in Fig. 6-5 and is worth pursuing as a future direction research.
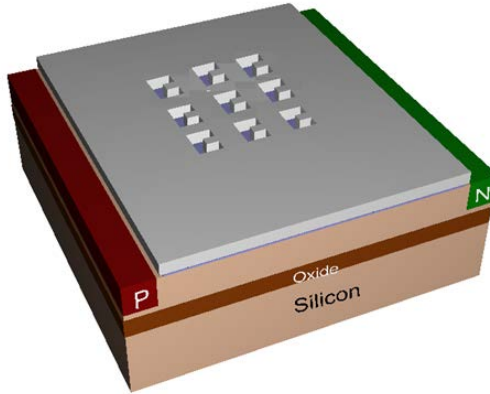
Figure 6-5: Proposed plasmonic-enhanced TPPV power converter using an array of C-shaped apertures.

CHAPTER 7: FUTURE WORK

7.1　　　Active Coherent Beam-Combining via Mid-infrared Silicon Raman Lasing

Quantum cascade lasers (QCLs) are able to deliver optical powers in a wide wavelength range (3.5 to 150 μm) and are considered as good candidates for mid-IR integrated photonics applications. A single QCL, however, cannot provide very high powers. Indeed, room-temperature and CW operation is limited due to the heating of the active region at high current densities. Beam-combining can be applied to simply add up the powers of several lasers, while keeping the beam quality of a single emitter. Coherent beam-combining can be achieved by several schemes including approaches based on a common resonator, evanescent or leaky waves, self-organizing or supermode, active feedback and nonlinearities (phase conjugation) [124].

One scheme for coherent beam combining of laser sources is optical nonlinearities. One approach theoretically suggested in 1986 is using SRS in optically nonlinear media [125]. Mid-IR SRLs have been theoretically modeled and experimentally attempted in Section 2.3. Here, a novel photonic circuit is proposed to practically demonstrate this idea via Mid-IR silicon Raman lasing. The schematic of the proposed technique is illustrated in Fig. 7-1.
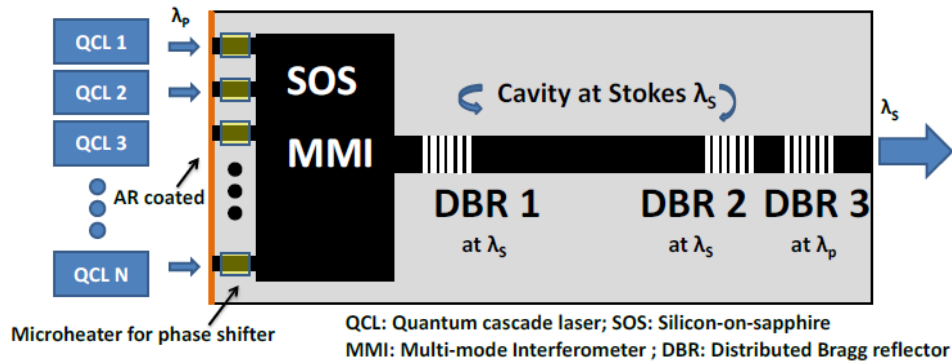
Figure 7-1: Proposed coherent beam-combining technique using a silicon Raman laser pumped by an array of QCLs.

The optical outputs of N independent QCLs at λ_p are combined to pump a Raman laser on SOS using a multimode interferometers (MMI) on SOS. The design of a 10×1 MMI operating at 4.6 µm is presented in Fig. 7-2. In order to obtain coherent combining of the input beams, appropriate phase differences among the 10 inputs ought to be preserved. A typical calculated input phase profile is shown in Fig. 7-2(b). These choices of phase differences lead to the evident beam-combing at the MMI output shown in Fig. 7-2(c). The required phase shifts (Fig. 7-2(b)) can be introduced at the input waveguides by the thermo-optic effect via microheaters. Such Mid-IR MMIs may find applicators beyond the present beam-combiners, e.g., power splitters, arrayed-waveguide gratings and photodetector arrays.
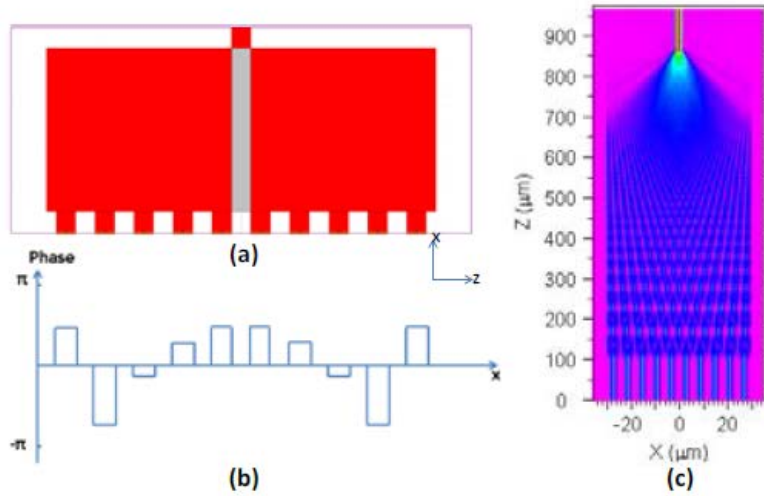
Figure 7-2: (a) Top-view schematic. The MMI length is ~770 μm. Input arms are 1 mm long to accommodate 950 μm heaters (not shown); (b) and (c) Induced input phase difference via appropriate biasing of phase shifters to achieve coherently-combined beams at the output waveguide.

The actual coherent beam-combining is mediated by Raman lasing in the shown cavity in Fig. 7-1, which is resonant at the coherent Stokes wavelength of λ_s. The Bragg wavelength of the schematically shown integrated distributed Bragg reflectors (DBR1 and DBR2) is designed to be at λ_s, while the combined pump power of QCLs at λ_p is not reflected by the input DBR1 and can feed the SRS process. DBR3 only reflects λ_p to boost the pump intensity in the cavity. The DBRs can be achieved in practice by fabricating uniform grating waveguides on SOS. The advantage over that passive technique is that the common cavity is on silicon and hence the QCLs can be off-the-shelf components (no anti- or high-reflection coating needed). Wavelength tunability is a major advantage of the Raman laser approach.

In Section 2.5, the idea of VCSRA is proposed and the design of the top and bottom mirrors has been presented. Here we propose a novel mid-IR imaging system using VCSRA as pre-amplifier (Fig. 4-3). The imaging system consists of a pump laser that allows scanning of the beam, a dichroic beam splitter that can efficiently transmit the pump and reflect the Stokes beam and hence combine the two beams, a lens array for focusing both the pump and the signal into the VCSRA, which pre-amplifies the signal, and a photodiode (PD) array. Each photodiode corresponds to a pixel on the screen.
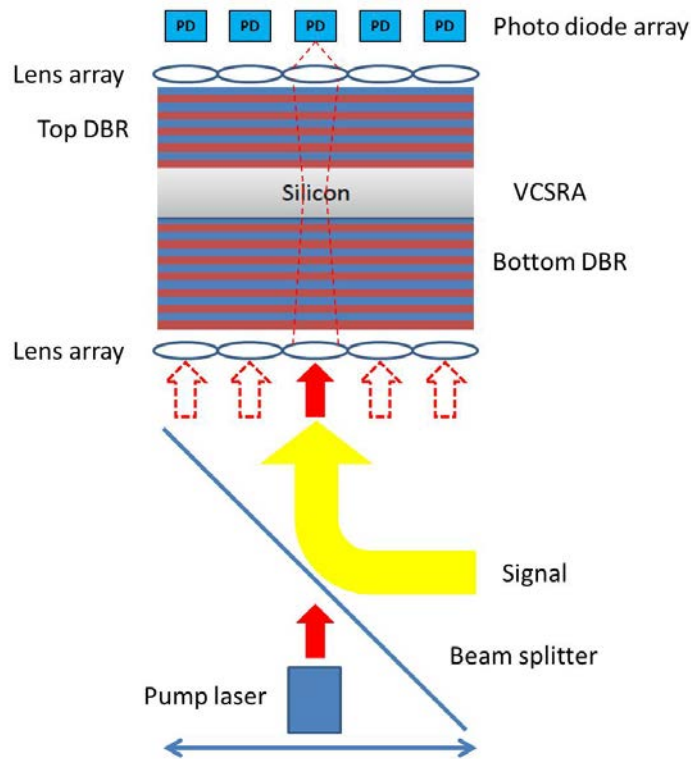
Figure 7-3: The proposed mid-IR imaging system using VCSRA array as pre-amplifiers.

The work that will be conducted in the future include the design of laser beam scanning, lens array and photo diode array, as well as theoretical studies on the NF of the VCSRA considering the cavity effect.

7.3   Radio-Frequency and high-Speed Characterization of the LiNbO$_3$ Electro-optic Modulators

The high-speed modulation properties of the LiNbO$_3$ EO modulators in Section 4.3 have been characterized by measuring the S$_{21}$ parameter of the modulated signal using a network analyzer. The devices are functional up to a few GHz [92]. However, the data obtained was not good enough for full characterization of the modulation properties and extraction of the modulation bandwidth. Below are the suggested ways to improve the performance of the EO modulators at radio frequencies (RF):

1. RF-termination of the electrodes is essential in characterization of high-speed modulators. This can be realized by adding a 50-Ω resistor to the end of the transmission line and connecting it to the chip by a ground-signal-ground (GSG) probe or through wire bonding.

2. Benzocyclobutene (BCB) can be used instead of SiO$_2$ for passivation of the device. The dielectric constant BCB is lower (~2.65) compared with SiO$_2$ (~3.9) and has no frequency dependence for frequencies from 1 kHz to 20 GHz. Moreover, BCB can be easily coated using spinner and the surface flatness of the cladding layer is better than

that of deposited SiO_2. Therefore, better RF performance of the EO modulators is expected using BCB as the material for cladding.

3. Impedance matching is of great importance in achieving high modulation bandwidth in RF systems. So far, we have been focusing on achieving lower V_π values by placing the positive and negative electrodes as close to each other as possible (4 µm distance [92]). This makes it quite difficult to achieve impedance matching with the current design as the electrodes on the transmission line, grown by electroplating, are also too close to each other. The electrode design shown in Fig. 7-4 not only takes the advantage of our highly-confined optical waveguides but also provides flexibility in the transmission line design. The fabrication of such electrodes requires additional photolithography (image reversal is required if positive photoresist is employed) and lift-off steps.
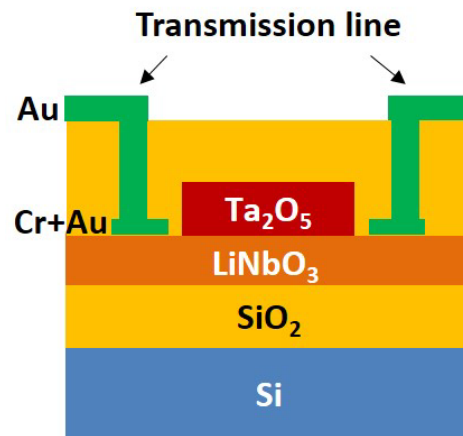
Figure 7-4: Electrode design to achieve impedance match in RF transmission line. The electrodes can be placed further away from each other without increasing the V_π value of the EO modulator.

4. High-speed photo receivers with bandwidth of 10 GHz or higher is needed for RF characterization.

7.4 Experimental Demonstration of Harmonic Generation in LiNbO$_3$ and Ta$_2$O$_5$-on Silicon Waveguides

SHG in LiNbO$_3$-on-silicon and THG in Ta$_2$O$_5$-on-silicon has been theoretically studied in Section 4.4. The phase-matching condition required by SHG and THG can be achieved by conducting dispersion engineering in the geometry design of the ridge waveguide. Also, attainability of small cross-sections using the novel technologies presented in Chapter 4 implies the required intensity for the onset of the desired nonlinearity can be achieved with much lower optical powers. Figure 7-5 shows the experimental set up for demonstration of SHG in LiNbO$_3$-on-silicon and THG in Ta$_2$O$_5$-on-silicon. The output spectrum can be easily measured with an optical spectrum analyzer (OSA). Visible light can be generated on silicon from infrared sources based on this scheme.
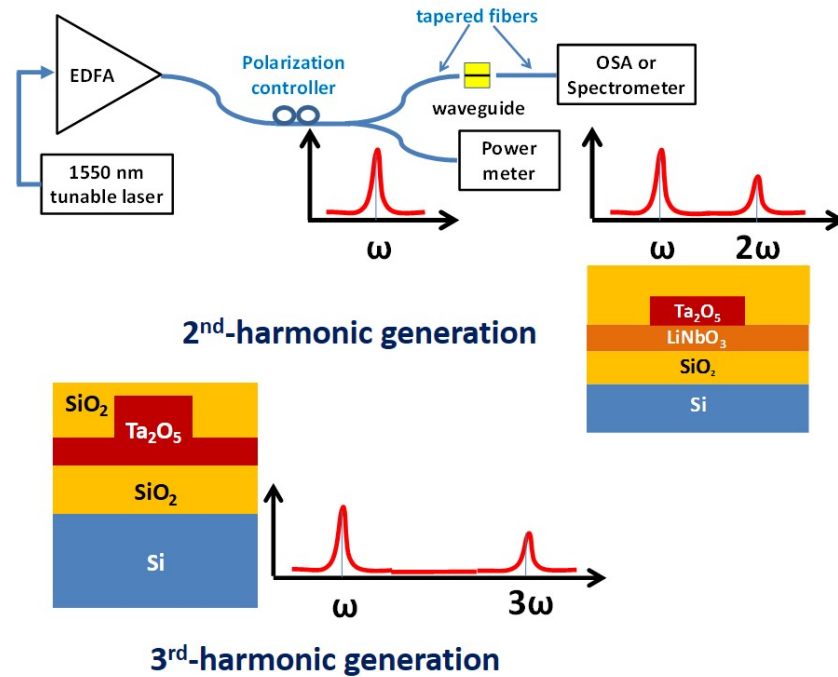
Figure 7-5: The experimental set up for demonstration of SHG in LiNbO$_3$-on-silicon and THG in Ta$_2$O$_5$-on-silicon.

7.5   Power Efficiency of the Two-photon Photovoltaic Effect in Gallium Arsenide

The TPPV effect is considered as a viable solution for achieving energy-efficient integrated photonic devices. It has been theoretically predicted in Section 5.3 that the power efficiency of the TPPV effect in GaAs at wavelength of 1550 nm can reach 8% (Fig. 5-8) or even higher assuming low linear propagation loss, zero ohmic loss at the contacts and long enough devices.

In order to improve the performance of the TPPV devices at wavelength of 1550 nm, first of all, the bottom cladding layer (intrinsic AlGaAs) has to be thick enough to avoid mode

leakage into the GaAs substrate. It has been proved in simulation that a thickness of above 2 µm is required to achieve trivial imaginary part of the effective index ($\sim 10^{-7}$) and negligible mode leakage; second, the linear propagation loss of the GaAs/AlGaAs waveguides can be further reduced by optimizing the dry etching recipe for etching GaAs; third, instead of using the gold layer as a mask for GaAs etching, the electrodes can be added to the fabricated junction diodes after the dry etching process through a secondary photolithography. This will greatly reduce the surface roughness of the electrodes. The negative electrode can be placed on top of the n^+-GaAs slab for the ease of making contacts with probes. Increasing the thickness of the gold layer will further reduce the series resistivity in the circuit. In the end, if the linear propagation loss of the waveguide is low enough (< 1 dB/cm), increasing the length of the device to a few centimeters can greatly improve the power efficiency.

APPENDIX: FABRICATION STEPS AND SIMULATION CODES FOR GAAS/ALGAAS HETEROJUNCTION DIODES

A.1   Fabrication Steps and Recipes for GaAs/AlGaAs Heterojunction Diodes

The processing steps of the GaAs/AlGaAs heterojunction diodes (Fig. 5-3) has been stated in Section 5.3. Here are the recipes for photolithography using negative photoresist NR7-1000PY and dry etching of GaAs.

1. Photolithography using negative photoresist NR7-1000PY

Mask aligner: Karl Suss MJB3 UV 300;

Spin coat: 4000 rpm for 40 s;

Prebake at 150 °C for 1 min;

UV exposure at 12 mW for 14 second;

Postbake at 100 °C for 1 min;

Develop in RD 6 for 6 s.

2. Dry etching of GaAs using ICP-RIE (Plasma Therm)

Pressure = 10 mT;

Gas flow rate: BCl_3 = 11 sccm, Ar = 21 sccm;

ICP power = 200 W;

RIE power = 100 W;

Etch rate ~ 80 nm/min.

The 4.2-µm-deep dry etching was split into three steps and wet etching was performed in the middle for the purpose of removing the residue.

Etchant: citric acid: H_2O_2 = 4:1;

Etch time = 4 s.

A.2   COMSOL Codes for Simulation of the Two-photon Photovoltaic Effect in GaAs/AlGaAs

Heterojunction Diodes

The COMSOL simulation of the TPPV effect in GaAs/AlGaAs heterojunction diodes includes two Transport of Diluted Species Modules for solving the drift-diffusion equations (for electrons and holes respectively) and an Electrostatics Module for solving the Poisson's equation.

Parameters:

width 2[um]
y0 -1.7[um]
y1 -1.5[um]
y2 -0.9[um]
y3 -0.5[um]
y4 0.5[um]
y5 0.9[um]
y6 1.5[um]
y7 1.7[um]
Va 0[V] Bias voltage
q 1.602e-19[C] Elementary Charge
T 300[K] Room temperature
k 1.38e-23[J/K] Boltzmann's constant
h1 6.6261e-34[m^2*kg/s] planck's constant
c1 3e8[m/s] speed of light
c q/(k*T) Reciprocal Thermal voltage
NA1 3e17[1/cm^3] p-type doping
NA2 2e18[1/cm^3] p+ doping concentration
ND1 3e17[1/cm^3] n-type doping
ND2 2e18[1/cm^3] n+ doping concentration
epsilonrGaAs 13.1 relative permittivity for GaAs
niGaAs sqrt(NcGaAs*NvGaAs)*exp(-EgGaAs/(2*k*T)) intrinsic concentration for GaAs
munGaAs 8500[cm^2/(V*s)] electron mobility for GaAs
mupGaAs 400[cm^2/(V*s)] hole mobility for GaAs
m0 9.1e-31[kg] electron mass
meGaAs 0.067*m0 electron effective mass for GaAs

mhGaAs 0.48*m0 hole effective mass for GaAs

NcGaAs 2*(2*pi*meGaAs*k*T/(h1^2))^(3/2) effective density of states in the conduction band for GaAs

NvGaAs 2*(2*pi*mhGaAs*k*T/(h1^2))^(3/2) effective density of states in the valence band for GaAs

EgGaAs 1.42[eV] energy bandgap for GaAs

XGaAs 4.06[eV] electron affinity for GaAs

epsilonrAlGaAs 12.474 relative permittivity for AlGaAs

munAlGaAs 4925[cm^2/(V*s)] electron mobility for AlGaAs

mupAlGaAs 241.15[cm^2/(V*s)] hole mobility for AlGaAs

meAlGaAs 0.0755*m0 electron effective mass for AlGaAs

mhAlGaAs 0.5475*m0 hole effective mass for AlGaAs

NcAlGaAs 2*(2*pi*meAlGaAs*k*T/(h1^2))^(3/2) effective density of states in the conduction band for AlGaAs

NvAlGaAs 2*(2*pi*mhAlGaAs*k*T/(h1^2))^(3/2) effective density of states in the valence band for AlGaAs

EgAlGaAs 1.611[eV] energy bandgap for AlGaAs

XAlGaAs 3.905[eV] electron affinity for AlGaAs

niAlGaAs sqrt(NcAlGaAs*NvAlGaAs)*exp(-EgAlGaAs/(2*k*T)) intrinsic concentration for AlGaAs

taun 1e-8[s] electron life time

taup 1e-8[s] hole life time

deltaN1 k*T*log(NcAlGaAs/ND1)

deltaN2 k*T*log(NcGaAs/ND2)

deltaP1 k*T*log(NvAlGaAs/NA1)

deltaP2 k*T*log(NvGaAs/NA2)

V0 ((XGaAs+EgGaAs-deltaP2)-(XAlGaAs+EgAlGaAs-deltaP1))/q

V1 V0+1/q*(EgAlGaAs-k*T*log(NcAlGaAs/niAlGaAs)-deltaP1)

V2 1/q*(k*T*log(NcAlGaAs/niAlGaAs)+XAlGaAs-k*T*log(NcGaAs/niGaAs)-XGaAs)+V1

V3 V1

V4 1/q*(k*T*log(NcAlGaAs/niAlGaAs)-deltaN1)+V3

V5 V4+1/q*((XAlGaAs+deltaN1)-(XGaAs+deltaN2))

psips 0[V]

psins V5-Va

nns ND2/2+sqrt(ND2^2/4+niGaAs^2)

pps NA2/2+sqrt(NA2^2/4+niGaAs^2)

pns niGaAs^2/nns

nps niGaAs^2/pps

phinns psins+XGaAs/q-k*T/q*log(nns/NcGaAs)

phinps psips+XGaAs/q-k*T/q*log(nps/NcGaAs)

phipns psins+(XGaAs+EgGaAs)/q-k*T/q*log(NvGaAs/pns)

phipps psips+(XGaAs+EgGaAs)/q-k*T/q*log(NvGaAs/pps)

betaTPA 40e-11[m/W] TPA coefficient

lambdap 976[nm] wavelength

Ep h1*c1/lambdap photon energy

Pin 0[mW] total coupled power

Variables:

112

N -NA2*(y>=y6)-NA1*(y>=y5)*(y<y6)+ND1*(y<y2)*(y>=y1)+ND2*(y<y1) doping concentration

ni
niGaAs*(y>=y6)+niAlGaAs*(y>=y4)*(y<y6)+niGaAs*(y>=y3)*(y<y4)+niAlGaAs*(y<y3)*(y>=y1)+ni
GaAs*(y<y1) intrinsic carrier concentration

epsilonr
epsilonrGaAs*(y>=y6)+epsilonrAlGaAs*(y>=y4)*(y<y6)+epsilonrGaAs*(y>=y3)*(y<y4)+epsilonrAlGa
As*(y<y3)*(y>=y1)+epsilonrGaAs*(y<y1) relative permittivity

Eg
EgGaAs*(y>=y6)+EgAlGaAs*(y>=y4)*(y<y6)+EgGaAs*(y>=y3)*(y<y4)+EgAlGaAs*(y<y3)*(y>=y1)
+EgGaAs*(y<y1) bandgap energy

X
XGaAs*(y>=y6)+XAlGaAs*(y>=y4)*(y<y6)+XGaAs*(y>=y3)*(y<y4)+XAlGaAs*(y<y3)*(y>=y1)+X
GaAs*(y<y1) electron affinity

mun
munGaAs*(y>=y6)+munAlGaAs*(y>=y4)*(y<y6)+munGaAs*(y>=y3)*(y<y4)+munAlGaAs*(y<y3)*(y
>=y1)+munGaAs*(y<y1) electron mobility

mup
mupGaAs*(y>=y6)+mupAlGaAs*(y>=y4)*(y<y6)+mupGaAs*(y>=y3)*(y<y4)+mupAlGaAs*(y<y3)*(y
>=y1)+mupGaAs*(y<y1) hole mobility

Nc
NcGaAs*(y>=y6)+NcAlGaAs*(y>=y4)*(y<y6)+NcGaAs*(y>=y3)*(y<y4)+NcAlGaAs*(y<y3)*(y>=y1)
+NcGaAs*(y<y1) effective density of states in the conduction band

Nv
NvGaAs*(y>=y6)+NvAlGaAs*(y>=y4)*(y<y6)+NvGaAs*(y>=y3)*(y<y4)+NvAlGaAs*(y<y3)*(y>=y1
)+NvGaAs*(y<y1) effective density of states in the valence band

RSRH (n*p-ni^2)/(taup*(n+ni)+taun*(p+ni)) recombination term

psi_init
0*(y>=y6)+V0*(y>=y5)*(y<y6)+V1*(y<y5)*(y>=y4)+V2*(y<y4)*(y>=y3)+V3*(y<y3)*(y>=y2)+V4*(
y<y2)*(y>=y1)+V5*(y<y1) Charge neutrality voltage

n_init (abs(N)/2+sqrt(N^2/4+ni^2))*(N>=0)+ni^2/(abs(N)/2+sqrt(N^2/4+ni^2))*(N<0) charge neutrality
electron concentration

p_init (abs(N)/2+sqrt(N^2/4+ni^2))*(N<0)+ni^2/(abs(N)/2+sqrt(N^2/4+ni^2))*(N>=0) charge neutrality
hole concentration

etac c*(psi-phin+X/q)

etav -c*(psi-phip+(X+Eg)/q)

n Nc*exp(etac) electron concentration

p Nv*exp(etav) hole concentration

phin_init psi_init+X/q-1/c*log(n_init/Nc)

phip_init psi_init+(X+Eg)/q+1/c*log(p_init/Nv)

Jn q*mun*n*phiny

Jp q*mup*p*phipy

J Jn+Jp

beta betaTPA*(x>=-width/2)*(x<=width/2)*(y>=y3)*(y<=y4)

G beta*Ip^2/2/Ep

Ip Pin*int1(x,y)/intop2(int1(x,y))

LIST OF REFERENCES

[1]   B. Jalali and S. Fathpour, "Silicon Photonics," J. Lightw. Technol., vol. 24, pp. 4600-4615, 2006.

[2]   T. Barwicz, H. Byun, F. Gan, C. W. Holzwarth, M. A. Popovic, P. T. Rakich, M. R. Watts, E. P. Ippen, F. X. Kärtner, H. I. Smith, J. S. Orcutt, R. J. Ram, V. Stojanovic, O. O. Olubuyide, J. L. Hoyt, S. Spector, M. Geis, M. Grein, T. Lyszczarz, and J. U. Yoon, "Silicon photonics for compact, energy-efficient interconnects," Journal of Optical Networking, vol. 6, pp. 63–73, 2006.

[3]   Y. Vlasov, W. M. J. Green and F. Xia, "High-throughput silicon nanophotonic wavelength-insensitive switch for on-chip optical networks," Nature Photon., vol. 2, pp. 242–246, 2008.

[4]   W. A. Zortman, A. L. Lentine, M. R. Watts, and D. C. Trotter, "Power penalty measurement and frequency chirp extraction in silicon microdisk resonator modulators," *Proc. Optical Fiber Communication Conference*, paper OMI7, 2010.

[5]   W. A. Zortman, A. L. Lentine, M. R. Watts, and D. C. Trotter, "Power penalty measurement and frequency chirp extraction in silicon microdisk resonator modulators," *Proc. Optical Fiber Communication Conference*, paper OMI7, 2010.

[6]   G. C. Holst, and S. W. McHugh, "Review of thermal imaging system performance," Proceedings of SPIE, pp. 78-84, 1992.

[7]   H. B. Gray, *Chemical Bonds*: *An Introduction to Atomic and Molecular Structure*, University Science Books, 1994.

[8]   P. Werle, F. Slemr, K. Maurer, R. Kormann, R. Mucke, and B. Janker, "Near- and mid-infrared laser optical sensors for gas analysis," Opt. Lasers Eng., vol. 37, pp. 101-114, 2002.

[9]   T. K. Liang and H. K. Tsang, "Role of free carriers from two-photon absorption in Raman amplification in silicon-on-insulator waveguides," Appl. Phys. Lett., vol. 84, pp. 2745-2747, 2004.

[10]   V. Raghunathan, R. Shori, O. M. Stafsudd, and B. Jalali, "Nonlinear absorption in silicon and the prospects of mid-IR Raman lasers," IEEE J. Sel. Top. Quantum Electron., vol. 12, pp. 1618-1627, 2006.

[11] AdTech Optics, Inc., http://www.atoptics.com/pdf/specs_CSmount_0380um.pdf.

[12] E. M. Dianov, "Single Mode As-S Glass Fibers," Inorg. Mater. 39, 627-630, 2003.

[13] Kazuto Noguchi, Osamu Mitomi, and Hiroshi Miyazawa, "Millimeter-wave Ti:LiNbO$_3$ optical modulators," IEEE J. Lightwave Technol., vol. 16, pp. 615–619, 1998.

[14] S. Fathpour, K. Tsia, and B. Jalali, "Two-photon photovoltaic effect in silicon," IEEE Journal of Quantum Electronics, vol. 43, pp. 1211-1217, 2007.

[15] B. Jalali, S. Fathpour, and K. Tisa, "Green silicon photonics," Optics & Photonics News, pp. 18-23, June 2009.

[16] S. Fathpour, K. Tisa, and B. Jalali, "Nonlinear photovoltaics and energy harvesting," in *Silicon Photonics for Telecommunications and Biomedicine*, S. Fathpour and B. Jalali, eds. (CRC Press, 2012), pp. 363–381.

[17] V. Raghunathan, D. Borlaug, R. R. Rice, and B. Jalali, "Demonstration of a mid-infrared silicon Raman amplifier," Opt. Express, vol. 15, pp. 14355–14362, 2007.

[18] D. Borlaug, S. Fathpour, and B. Jalali, "Extreme value statistics in silicon photonics," IEEE Photon. J., vol. 1, pp. 33–39, 2009.

[19] X. Liu, R. M. Osgood, Y. A. Vlasov, and W. M. J. Green, "Mid-infrared optical parametric amplifier using silicon nanophotonic waveguides," Nature Photon., vol. 4, pp. 557–560, 2010.

[20] S. Zlatanovic, J. S. Park, S. Moro, J. M. C. Boggio, I. B. Divliansky, N. Alic, S. Mookherjea, and S. Radic, "Mid-infrared wavelength conversion in silicon waveguides using ultracompact telecom-band-derived pump source," Nature Photon., vol. 4, pp. 561–564, 2010.

[21] T. Baehr-Jones, A. Spott, R. Ilic, B. Penkov, W. Asher, and M. Hochberg, "Silicon-on sapphire integrated waveguides for the mid-infrared," Opt. Express, vol. 18, pp. 12127–12135, 2010.

[22] G. Z. Mashanovich, M. M. Milošević, M. Nedeljkovic, N. Owens, B. Xiong, E. J. Teo, and Y. Hu, "Low loss silicon waveguides for the mid-infrared," Opt. Express, vol. 19, pp. 7112–7119, 2011.

[23] Z. Cheng, X. Chen, C. Y. Wong, K. Xu, C. K. Y. Fung, Y. M. Chen, and H. K. Tsang, "Mid-infrared grating couplers for silicon-on-sapphire waveguides," IEEE Photon. J., vol. 4, pp. 104–113, 2012.

[24] B. Jalali, "Nonlinear optics in the mid-infrared," Nature Photon., vol. 4, pp. 506-508, 2010.

[25] S. Pearl, N. Rotenberg, and H. M. Driel, "Three photon absorption in silicon for 2300-3300 nm," Appl. Phys. Lett. 93, 131102, 2008.

[26] S. Khan, J. Chiles, J. Ma, and S. Fathpour, "Silicon-on-nitride waveguides for mid- and near-infrared integrated photonics," Appl. Phys. Lett., vol. 102, p. 121104, 2013.

[27] J. Chiles, S. Khan, J. Ma, and S. Fathpour, "High-contrast, all-silicon waveguiding platform for ultra-broadband mid-Infrared photonics," Appl. Phys. Lett., vol. 103, p. 151106, 2013.

[28] R. A. Soref, S. J. Emelett, and W. R. Buchwald, "Silicon waveguided components for the long-wave infrared region," J. Optics A, vol. 8, pp. 840–848, 2006.

[29] S. P. Campbell, *The Science and Engineering of Microelectronic Fabrication*, Oxford University Press, New York, NY, 1996

[30] R. Claps, D. Dimitropoulos, Y. Han, and B. Jalali, "Observation of Raman emission in silicon waveguides at 1.54 µm," Opt. Express, vol. 10, pp. 1305-1313, 2002.

[31] O. Boyraz, and B. Jalali, "Demonstration of a silicon Raman laser," Opt. Express, vol. 12, pp. 5269-5273, 2004.

[32] H. Rong, R. Jones, A. Liu, O. Cohen, D. Hak, A. Fang and M. Paniccia, "A continuous-wave Raman silicon laser," Nature, vol. 433, pp. 725-728, 2005.

[33] Y. –H. Kuo, H. Rong, and M. Paniccia, "High bandwidth silicon ring resonator Raman amplifier," *Group IV Photonics Conference (GFP 2006)*, paper FB2, 2006.

[34] M. Krause, H. Renner, S. Fathpour, B. Jalali, and E. Brinkmeyer, "Gain enhancement in cladding-pumped silicon Raman amplifiers," IEEE J. Quantum Electron., vol. 44, pp. 692-704, 2008.

[35] R. Claps, D. Dimitropoulos, V. Raghunathan, Y. Han, and B. Jalali, "Observation of stimulated Raman scattering in Silicon waveguides," Opt. Express, vol. 11, pp. 1731-1739, 2003.

[36]   H. M. Pask, "The design and operation of solid-state Raman lasers," Prog. Quantum Electron., vol. 27, 3-56, 2003.

[37]   A. Liu, L. Liao, and H. Rong, "Recent development in silicon photonics: 2.5 Gb/s silicon optical modulator and silicon Raman laser," Proc. of SPIE, vol. 5730, pp. 80–93, 2005.

[38]   X. Chen, N. C. Panoiu, and R. M. Osgood, "Theory of Raman-mediated pulsed amplification in silicon-wire waveguides," IEEE J. Quantum Electron., vol. 42, pp. 160–170, 2006.

[39]   M. Krause, R. Draheim, H. Renner, and E. Brinkmeyer, "Cascaded silicon Raman lasers as mid-infrared sources," Electron. Lett., vol. 42, pp. 1224-1225, 2006.

[40]   M. Krause, H. Renner, and E. Brinkmeyer, "Theory of silicon Raman amplifiers and lasers," in *Silicon Photonics for Telecommunications and Biomedicine*, S. Fathpour and B. Jalali, eds. (CRC Press, 2012), pp.131–200.

[41]   I. D. Rukhlenko, M. Premaratne, and G. P. Agrawal, "Nonlinear silicon photonics: analytical tools," IEEE J. Sel. Top. Quantum Electron., vol. 16, pp. 200–215, 2010.

[42]   H. Rong, S. Xu, O. Cohen, O. Raday, M. Lee, V. Sih, and M. Paniccia, "A cascaded silicon Raman laser," Nature Photon., vol. 2, pp. 170–174, 2008.

[43]   J. Ma and S. Fathpour, "Pump-to-Stokes relative intensity noise transfer and analytical modeling of mid-infrared silicon Raman lasers," Optics Express, vol. 20, pp. 17962-17972, July 2012.

[44]   F. Leplingard, C. Martinelli, S. Borne, L. Lorcy, D. Bayart, F. Castella, P. Chartier, and E. Faou, "Modeling of multiwavelength Raman fiber lasers using a new and fast algorithm," IEEE Photon. Technol. Lett., vol. 16, pp. 2601–2603, 2004.

[45]   J. Zhou, J. Chen, X. Li, G. Wu, and Y. Wang, "Exact analytical solution for Raman fiber lasers," IEEE Photon. Technol. Lett., vol. 18, pp. 1097–1099, 2006.

[46]   Z. Qin, X. Zhou, Q. Li, H. Wu, and Z. Zhou, "An improved theoretical model of nth-order cascaded Raman fiber lasers," J. Lightw. Technol., vol. 25, pp. 1555–1560, 2007.

[47]   S. A. Babin, D. V. Churkin, and E. V. Podivilov, "Intensity interactions in cascades of a two-stage Raman fiber laser," Opt. Commun., vol. 226, pp. 329–335, 2003.

[48] C. Huang, Z. Cai, C. Ye, H. Xu, and Z. Luo, "Optimization of dual-wavelength cascaded Raman fiber lasers using an analytic approach," Opt. Commun., vol. 272, pp. 414–419, 2007.

[49] K. Huang, X. Zhou, Z. Qin, H. Wu, and Z. Zhou, "A novel fast numerical algorithm for cascaded Raman fiber laser using the analytic approximate solution," Opt. Commun., vol. 271, pp. 257–262, 2007.

[50] H. Rong, Y.-H. Kuo, S. Xu, A. Liu, R. Jones, and M. Paniccia, "Monolithic integrated Raman silicon laser," Opt. Express, vol. 14, pp. 6705–6712, 2006.

[51] M. Krause, S. Cierullies, H. Renner, and E. Brinkmeyer, "Pump-to-Stokes RIN transfer in Raman fiber lasers and its impact on the performance of co-pumped Raman amplifiers," Opt. Commun., vol. 260, pp. 656–661, 2006.

[52] X. Sang, D. Dimitropoulos, and B. Jalali, "Influence of pump-to-signal RIN transfer on noise figure in silicon Raman amplifiers," IEEE Photon. Technol. Lett., vol. 20, pp. 2021–2023, 2008.

[53] I. D. Rukhlenko, I. Udagedara, M. Premaratne, and G. P. Agrawal, "Effect of free carriers on pump-to-signal noise transfer in silicon Raman amplifiers," Opt. Lett., vol. 35, pp. 2343–2345, 2010.

[54] X. Liu, X. Sang, B. Yan, K. Wang, C. Yu, and W. Dou, "Influences of pump-to-Stokes RIN transfer on the single order silicon Raman lasers," Optoelectron. Adv. Mater. Rapid Comm., vol. 4, pp. 1284–1288, 2010.

[55] Q. Lin, J. Zhang, P. M. Fauchet, and, G. P. Agrawal, "Ultrabroadband parametric generation and wavelength conversion in silicon waveguides," Opt. Express, vol. 14, pp. 4786-4799, 2006.

[56] J. Leuthold, C. Koos and W. Freude, "Nonlinear silicon photonics," Nature Photonics, vol. 4, pp. 535–544, 2010.

[57] G. P. Agrawal, *Nonlinear Fiber Optics*, 4th Edition, Academic Press, Burlington, MA, 2007.

[58] Q. Lin, J. Zhang, G. Piredda, R. W. Boyd, P. M. Fauchet, and G. P. Agrawal, "Dispersion of silicon nonlinearities in the near infrared region," Appl. Phys. Lett., vol. 91, 021111, 2007.

[59] A. D. Bristow, N. Rotenberg, and H. M. van Driel, "Two-photon absorption and Kerr coefficients of silicon for 850–2200 nm," Appl. Phys. Lett., vol. 90, 191104, 2007.

[60] N. K. Hon, R. Soref, and B. Jalali, "The third-order nonlinear optical coefficients of Si, Ge, and Si1-xGex in the midwave and longwave infrared," J. Appl. Phys., vol. 110, p. 011301, 2011.

[61] P. L. Baldeck, and R. R. Alfano, "Intensity effects on the stimulated four photon spectra generated by picosecond pulses in optical fibers," J. Lightwave Technol., vol. 5, pp. 1712-1715, 1987.

[62] J. M. Dudley, G. Genty, and S. Coen, "Supercontinuum generation in photonic crystal fiber," Rev. Mod. Phys., vol. 78, pp. 1135-1184, 2006.

[63] I- W. Hsieh, X. Chen, X. Liu, J. I. Dadap, N. C. Panoiu, C-Y. Chou, F. Xia, W. M. Green, Y. A. Vlasov, and R. M. Osgood, "Supercontinuum generation in silicon photonic wires," Opt. Express, vol. 15, pp. 15242–15248, 2007.

[64] Q. Lin, O. J. Painter, and G. P. Agrawal, "Nonlinear optical phenomena in silicon waveguides: modeling and applications," Opt. Express, vol. 15, pp. 16604-16644, 2007.

[65] Ö. Boyraz, P. Koonath, V. Raghunathan, and B. Jalali, "All optical switching and continuum generation in silicon waveguides," Opt. Express, vol. 12, pp. 4094–4102, 2004.

[66] B. M. Cowan, "Optical damage threshold of silicon for ultrafast infrared pulses," *Boulder Damage Symposium XXXIX*, SLAC-PUB-12960, AARD-493, Boulder, CO, September 2007.

[67] A. Karim, S. Bjorlin, J. Piprek, and J. E. Bowers, "Long-wavelength vertical-cavity lasers and amplifiers," IEEE Journal of Selected Topics in Quantum Electronics, vol. 6, pp. 1244-1253, 2000.

[68] E. S. Bjorlin and J. E. Bowers, "Noise figure of vertical-cavity semiconductor optical amplifiers," IEEE Journal of Quantum Electronics, vol. 38, pp. 61-66, 2002.

[69] K. K. Tsia, S. Fathpour, and B. Jalali, "Energy harvesting in silicon wavelength converters," Opt. Express, vol. 14, pp. 12327-12333, 2006.

[70] Y. Okawachi, A. L. Gaeta, and M. Lipson, "Breakthroughs in nonlinear silicon photonics 2011," IEEE. Photon. J., vol. 4, pp. 601-605, 2012.

[71]   C. Grillet, L. Carletti, C. Monat, P. Grosse, B. B. Baker, S. Menezo, J. M. Fedeli, and D. J. Moss, "Amorphous silicon nanowires combining high nonlinearity, FOM and optical stability," Opt. Express, vol. 20, pp. 22609-22615, 2012.

[72]   K. Narayanan and S. F. Preble, "Optical nonlinearities in hydrogenated-amorphous silicon waveguides," Opt. Express, vol. 18, pp. 8998-9005, 2010.

[73]   B. Kuyken, S. Clemmen, S. K. Selvaraja, W. Bogaerts, D. V. Thourhout, P. Emplit, S. Massar, G. Roelkens, and R. Baets, "On-chip parametric amplification with 26.5 dB gain at telecommunication wavelengths using CMOS-compatible hydrogenated amorphous silicon waveguides," Opt. Lett., vol. 36, pp. 552-554, 2011.

[74]   B. Kuyken, H. Ji, S. Clemmen, S. K. Selvaraja, H. Hu, M. Pu, M. Galili, P. Jeppesen, G. Morthier, S. Massar, L. K. Oxenlowe, G. Roelkens, and R. Baets, "Nonlinear properties of and nonlinear processing in hydrogenated amorphous silicon waveguides," Opt. Express, vol. 19, pp. B146-B153, 2011.

[75]   D. Dimitropoulos, D. R. Solli, R. Claps, O. Boyraz, and B. Jalali, "Noise figure of silicon Raman Amplifiers," J. Lightwave Technol., vol. 26, pp. 847-852 (2008).

[76]   X. Sang, D. Dimitropoulos, and B. Jalali, "Influence of pump-to-signal RIN transfer on noise figure in silicon Raman amplifiers," IEEE Photon. Technol. Lett., vol. 20, pp. 2021-2023, 2008.

[77]   J. Ma and S. Fathpour, "Pump-to-Stokes relative intensity noise transfer and analytical modeling of mid-infrared silicon Raman lasers" Opt. Express, vol. 20, pp.17962-17972, 2012.

[78]   X. Liu, X. Sang, B. Yan, K. Wang, C. Yu, and W. Dou, "Influences of pump-to-Stokes RIN transfer on the single-order silicon Raman lasers," Optoelectron. Adv. Mater. Rapid Comm., vol. 4, pp. 1284-1288, 2010.

[79]   X. Sang and O. Boyraz, "Gain and noise characteristics of high-bit-rate silicon parametric amplifiers," Opt. Express, vol. 16, pp. 13122-13132, 2008.

[80]   Y. Huang, E. K. Tien, S. Gao, S. K. kalyoncu, Q. Song, F. Qian, E. Adas, D. Yildirim, and O. Boyraz, "Electrical signal-to-noise ratio improvement in indirect detection of mid-IR signals by wavelength conversion in silicon-on-sapphire waveguides," Appl. Phys. Lett., vol. 99, p. 181122, 2011.

[81]   T. Deschaines, J. Hodkiewicz, and P. Henson, "Characterization of amorphous and microcrystalline silicon using Raman spectroscopy," available at : http://www.thermoscientific.fr/eThermo/CMA/PDFs/Product/productPDF_56886.PDF

[82]   P. L. Voss and P. Kumar, "Raman-effect induced noise limits on $\chi^{(3)}$ parametric amplifiers and wavelength converters," J. Opt. B: Quantum Semiclass. Opt., vol. 6, pp. S762-S770, 2004.

[83]   F. Bassani and S. Scandolo, "Dispersion relations and sum rules in nonlinear optics," Phys. Rev. B, vol. 44, pp. 8446-3453, 1991.

[84]   E. Golovchenko, P. V. Mamyshev, A. N. Pilipetskii, and E. M. Dianov, "Mutual influence of the parametric effects and stimulated Raman scattering in optical fibers," IEEE J. Quantum Electron., vol. 26, pp. 1815-1820 (1990).

[85]   J. Ma and S. Fathpour, "Noise figure in near-infrared amorphous and mid-infrared crystalline silicon optical parametric amplifiers," IEEE Journal of Lightwave Technology, vol. 31, pp. 3181–3187, October 2013.

[86]   C. Headley and G. P. Agrawal, *Raman Amplification in Fiber Optical Communication Systems*, Elsevier Academic Press, Burlington, MA, 2005.

[87]   P. Kylemark, P. O. Hedekvist, H. Sunnerud, M. Karlsson and P. A. Andrekson, "Noise characteristics of fiber optical parametric amplifiers," J. Lightwave Technol., vol. 22, pp. 409-416, 2004.

[88]   Y. Shoji, T. Ogasawara, T. Kamei, Y. Sakakibara, S. Suda, K. Kintaka, H. Kawashima, M. Okano, T. Hasama, H. Ishikawa, and M. Mori, "Ultrafast nonlinear effects in hydrogenated amorphous silicon wire waveguides," Opt. Express, vol. 18, pp. 5668-5673, 2010.

[89]   S. Zhu, G. Q. Lo, and D. L. Kwong, "Low-loss amorphous silicon wire waveguide for integrated photonics: effect fabrication process and the thermal stability," Opt. Express, vol. 18, pp. 25283-25291, 2010.

[90]   S. Suda, K. Tanizawa, Y. Sakakibara, T. Kamei, K. Nakanishi, E. Itoga, T. Ogasawara, R. Takei, H. Kawashima, S. Namiki, M. Mori, T. Hasama, and H. Ishikawa, "Pattern-effect-free all-optical wavelength conversion using a hydrogenated amorphous silicon waveguide with ultra-fast carrier decay," Opt. Lett., vol. 37, pp. 1382-1384, 2012.

[91]   Z. Wang, H. Liu, N. Huang, Q. Sun, J. Wei, and X. Li, "Influence of three-photon absorption on mid-infrared cross-phase modulation in silicon-on-sapphire wavegudies," Opt. Express, vol. 21, pp. 1840-1848, 2013.

[92]   P. Rabiei, J. Ma, S. Khan, J. Chiles, and S. Fathpour, "Heterogeneous lithium niobate photonics on silicon substrates," Opt. Express, vol. 23, pp. 25573-25581, 2013.

[93]   K. Wong, *Properties of Lithium Niobate*, INSPEC, London, 2002.

[94]   M. Jazbinsek, and M. Zgonik, "Material tensor parameters of $LiNbO_3$ relevant for electro- and elastooptics," Appl. Phys. B, vol. 74, pp. 407–414, 2002.

[95]   E. L. Wooten, K. M. Kissa, A. Yi-Yan, E. J. Murphy, D. A. Lafaw, P. F. Hallemeier, D. Maack, D. V. Attanasio, D. J. Fritz, G. J. McBrien, and D. E. Bossi, "A Review of lithium niobate modulators for fiber-optic communications systems," IEEE J. Select. Topics Quant. Electron., vol. 6, pp. 69–72, 2000.

[96]   M. M. Howerton, R. P. Moeller, A. S. Greenblatt, and R. Krähenbühl, "Fully packaged, broad-band LiNbO3 modulator with low drive voltage," IEEE Photon. Technol. Lett., vol. 12, pp. 792–794, 2000.

[97]   P. Rabiei, J. Ma, S. Khan, J. Chiles, and S. Fathpour, "Submicron optical waveguides and microring resonators fabricated by selective oxidation of tantalum," Opt. Express, vol. 21, pp. 6967-6972, 2013.

[98]   Y. C. Cheng and W. D. Festwood, "Losses in tantalum pentoxide waveguides," J. Electron. Mater., vol. 3, pp. 37-50, 1974.

[99]   H. Takahashi, S. Suzuki, and I. Nishi, "Wavelength multiplexer based on SiO2-Ta2O5 arrayed-waveguide grating," J. Lightw. Technol., vol. 12, pp. 989-995 1994.

[100]   A. Guarino, G. Poberaj, D. Rezzonico, R. Degl'Innocenti, and P. Günter, "Electro–optically tunable microring resonators in lithium niobate," Nat. Photonics, vol. 1, pp. 407–410, 2007.

[101]   J. Kondo, A. Kondo, K. Aoki, M. Imaeda, T. Mori, Y. Mizuno, S. Takastsuji, Y. Kozuka, O. Mitomi, and M. Minakata, "40-Gb/s X-Cut $LiNbO_3$ optical modulator with two-step back-slot structure," J. Lightwave Tech., vol. 20, pp. 2110–2114, 2002.

[102]   R. Y. Chen, M. D. B. Charlton, and P. G. Lagoudakis, "Reference free Chi 3 dispersion measurements in planar tantalum pentoxide waveguides," *Proc. SPIE 7420, Photonic*

Fiber and Crystal Devices: Advances in Materials and Innovations in Device Applications III, paper 74200D, 2009.

[103]   S. Fathpour, K. Tsia, and B. Jalali, "Energy harvesting in Silicon Raman amplifiers," Applied Physics Letters, vol. 89, p. 061109, 2006.

[104]   K. Tsia, S. Fathpour, and B. Jalali, "Energy harvesting in silicon wavelength converters," Optics Express, vol. 14, pp. 12327-12333, 2006.

[105]   J. Ma, J. Chiles, Y. D. Sharma, S. Krishna and S. Fathpour, "Two-photon photovoltaic effect in gallium arsenide," accepted by *Conference of Laser and Electro-Optics*, 2014.

[106]   H. F. Tiedje, H. K. Haugen, and J. S. Preston, "Measurement of nonlinear absorption coefficients in GaAs, InP and Si by an optical pump THz probe technique," Optics Communications, vol. 274, pp. 187-197, 2007.

[107]   S. Krishnamurthy, Z. G. Yu, L.P. Gonzalez, and S. Guha, "Temperature- and wavelength-dependent two-photon and free-carrier absorption in GaAs, InP, GaInAs, and InAsP," Journal of Applied Physics, vol. 109, pp. 033102, 2011.

[108]   M. S. Lundstrom and R. J. Schuelke, "Numerical analysis of heterostructure semiconductor devices," IEEE Transactions on Electron Devices, vol. ed-30, pp. 1151-1159, 1983.

[109]   K. Horio and H. Yanai, "Numerical modeling of heterojunctions including the thermionic emission mechanism at the heterojunction interface," IEEE Transactions on Electron Devices, vol. 37, pp. 1093-1098, 1990.

[110]   P. Apiratikul, "Semiconductor waveguides for nonlinear optical signal processing," Ph.D. thesis, University of Maryland, 2009.

[111]   S. Pillai, K. R. Catchpole, T. Trupke, and M. A. Green, "Surface plasmon enhanced silicon solar cells", J. Appl. Phys., vol. 101, p. 093105, 2007.

[112]   D. M. Schaadt, B. Feng and E. T. Yu, "Enhanced semiconductor optical absorption via surface plasmon excitation in metal nanoparticles," Appl. Phys. Lett., vol. 86, p. 063106, 2005.

[113]   K. R. Catchpole and A. Polman, "Plasmonic solar cells," Optics Express, vol. 16, pp. 21793–21800, 2008.

[114] H. R. Stuart and D. G. Hall, "Island size effects in nanoparticle-enhanced photodetectors," Appl. Phys. Lett., vol. 73, No 26, pp. 3815–3817, 1998.

[115] D. Derkacs, S. H. Lim, P. Matheu, W. Mar, and E. T. Yu, "Improved performance of amorphous silicon solar cells via scattering from surface plasmon polaritons in nearby metallic nanoparticles," Appl. Phys. Lett., vol. 89, p. 093103, 2006.

[116] S. A. Maier, *Plasmonics: Fundamentals and Applications*, Springer, New York, NY, 2007.

[117] J. J. Mock, M. Barbic, D. R. Smith, D. A. Schultz, and S. Schultz, "Shape effects in plasmon resonance of individual colloidal silver nanoparticles," J. Chem. Phys., vol. 116, pp. 6755– 6759, 2002.

[118] S. J. Fonash, *Solar Cell Device Physics*, Academic Press, New York, NY, 1981.

[119] S. M. Sze, K. K. Ng, *Physics of Semiconductor Devices*, 3rd Edition, John Wiley & Sons, Hoboken, NJ, 2007.

[120] J. Liu, T. Wu, M. Cohen, and J. G. Werthen, "High efficient photovoltaic power converter suitable for 920nm to 970nm InGaAs laser diodes," *Proc. of SPIE*, paper 58710D-1, 2005.

[121] O. Lopatiuk-Tirpak, J. Ma, and S. Fathpour, "Optical transmission properties of C-shaped subwavelength waveguides on Silicon," Appl. Phys. Lett., vol. 96, p. 241109, 2010.

[122] J. A. Matter and L. Hesselink, "Fractal extensions of near-field aperture shapes for enhanced transmission and resolution," Opt. Express, vol. 13, pp. 636-647, 2005.

[123] T. W. Ebbesen, H. J. Lezec, H. F. Ghaemi, T. Thio, and P. A. Wolff, "Extraordinary optical transmission through sub-wavelength hole arrays," Nature, vol. 391, pp. 667–669, 1998.

[124] T. Y. Fan, "Laser beam combining for high-power, high-radiance sources," IEEE J. Select. Topics Quant. Electron., vol. 11, pp. 567–577, 2005.

[125] J. M. Eggleston, "Steady-state coherent Raman beam combining with multiaxial mode lasers," IEEE J. Quant. Electron., vol. 22, pp. 1942–1952, 1986.